INVESTIGATION OF LIGHT POLE BASE INTEGRITY

by

J.B. Mander
S.S. Chen
K.M. Shah
A. Madan

Department of Civil Engineering
State University of New York at Buffalo

Submitted to Erie County Department of Public Works
July 13, 1992

Investigation of
Light Pole Base Integrity

by

J. B. Mander
S. S. Chen
K. M. Shah
A. Madan

Submitted to Erie County Department of Public Works
13 July 1992

Department of Civil Engineering
State University of New York at Buffalo

ACKNOWLEDGEMENTS

The maintenance of instrumentation and data collection effort through the onerous winter months was faithfully carried out by Dr. Wei-Kuo K. Chen, formerly a Post-Doctoral Research Associate at SUNY at Buffalo. He also graciously donated the use of his computer for acoustic emission data logging. His involvement is gratefully acknowledged.

Assistance with field equipment setup and installation was provided by SUNY at Buffalo Laboratory Department of Civil Engineering Technicians Messrs. M. Pitman, D. Walch, G. Majewski, and X. Gao. Some of the equipment was provided by the Department. Their contributions are gratefully acknowledged.

The portions of this report dealing with acoustic emission data analysis, results and discussion are based in part on information provided by Dr. Z. Kevin Gong, Director of Engineering, MONAC International Corporation. The involvement of MONAC in this effort- equipment setup, data analysis and consultation- is gratefully acknowledged.

Prof. Zhou Jian, former Visiting Scholar at SUNY at Buffalo from Beijing University, conducted ANSI code predictions of pole loadings, base shears and moments in the early stages of this project. His participation is gratefully acknowledged.

Financial support of this investigation was provided by the Erie County Department of Public Works and the National Science Foundation.

EXECUTIVE SUMMARY

This report describes the results of an investigation of wind-induced fatigue and structural integrity of the anchorage of the middle west light pole at Rich Stadium in Orchard Park, New York.

An adequate approach to the problem of assessing the light pole base integrity requires an understanding of: the dynamic wind pressure effects; the dynamics of flexible structures and their response to along-wind and across-wind effects; and the mechanics of fatigue and fracture phenomena in steel. Current codes do not sufficiently address these issues either in isolation or in relation to each other.

In the investigation reported herein, a dual experimental-analytical approach was adopted. Theoretical response analyses based on measured wind speeds were conducted in tandem with a 6 month period of experimental measurements to quantify these effects on the Rich Stadium light poles and propose remedial actions. The use of a modern portable 16-channel PC-based computerized data acquisition system permitted an automated collection of data needed for behavior monitoring and condition assessment of the structure. In order to account for the less frequent higher wind speeds which were not encounted during the 6 month measurement period, analytical time-history pole dynamics predictions based on scaled-up actual wind records were developed to estimate the cyclic moment and stress range amplitudes needed to complete the fatigue evaluation.

Based on the wind environment at the site, the pole's dynamic response to it, and the resulting stress cycling in the bolts, several key conclusions are drawn:

1. A relationship is established among fatigue damage, bolt stress range, and mean wind velocity. This enables prediction of fatigue damage not just for the instrumented pole but also for other similar structures, in terms of historical wind velocity records, which are readily available.

2. A clear case can be made for the fatigue life of the bolts being consumed in less than the 20 year life of the pole to date. Thus, cracking observed by both ultrasonic and acoustic emission nondestructive testing techniques could reasonably have been expected.
3. Cracks are actively growing at higher wind speeds. Thus, proof tests of cracked bolts are not recommended as a means of assessing their safety. Remaining fatigue lives of instrumented cracked bolts could be less than one year.
4. Vortex shedding (cross wind effects) do not appear to be a major contributor to fatigue effects.

In order to increase the fatigue life of the light poles at Rich Stadium a three-phase retrofitting scheme is proposed. The first of these involves reseating the pole base with non-shrink grout. This eliminates the average stress range by 50% and increases the fatigue life 8-fold. The second phase requires additional high-strength thread-bars to be installed and post-tensioned after grouting to relieve the load on the existing anchor bolts. This second step should eliminate stress cycling on the existing bolts in all but the most extreme winds.

The third phase of reducing the stress ranges in the pole base would be to reduce the pole's dynamic response. This would have the effect of reducing the moment ranges and hence the stress ranges that must be sustained by the anchorage/base system. Viscous dampers are proposed as a means to accomplish this effect. Two dampers would be attached to each pole, anchored to the concrete parapet via a steel strap and to the pole via a collar. This measure should mitigate potential fatigue problems associated with the welded pole shell to base plate connection.

During the anchorage retrofit construction process, it is further suggested that the available portion of a cracked bolt be extracted for laboratory forensic analysis. Under controlled laboratory conditions, many of the rough assumptions that were necessary in conducting the post-cracking fatigue analyses could be directly investigated. Such investigations would provide more accurate insights into expected fatigue and crack

propagation behavior in the remaining anchor bolts. The types of investigations envisioned include: fatigue crack propagation and correlation of ΔK with acoustic emission counts; fractographic studies of crack surface to infer stress cycling history; and fracture toughness testing.

Continued monitoring of field stress range conditions in the anchor bolts is also recommended. The results may be used to assess the remaining need to install the proposed damper retrofit.

TABLE OF CONTENTS

SECTION 1

INTRODUCTION

1.1 BACKGROUND TO THE PROBLEM

Rich Stadium, the home playing field of the Buffalo Bills National Football League franchise, is located in the town of Orchard Park, Erie County. Opened in 1972, the 80,000 seat main stadium is flood lit by six tall light standards. The three west poles have 96 1500 W lights, and the three east poles have 60 1500W lights. During a routine maintenance check in 1990 it was discovered that the anchor bolt holding down nuts loosened under the repeated wind loads on the pole. Subsequent ultrasonic testing revealed fatigue crack "indications" located approximately at the leveling nut location. Such testing is unable to ascertain the cause, extent or growth rate of "indicated" cracking.

The purpose of the study reported herein was to investigate the integrity of the existing light pole base anchorages and to make remediation recommendations.

1.2 GENERAL NATURE OF THE PROBLEM

The effect of transient wind loads on slender structures is not simple to analyze. The determination of maximum and cyclic stresses is governed by the stochastic nature of the wind loading and the interaction of wind effects with structure response (aeroelasticity). For a cantilever light pole structure, Fig. 1.1 presents the interrelationships between: wind loads; dynamic response; and the fatigue resistance of the base foundation bolted connection. Fig. 1.1(a) illustrates how the incoming wind momentarily oriented at an angle θ with respect to the weak and strong bending axes induces base shear forces and moments (S_x, S_y, and M_x, M_y, respectively). The resulting dynamic response is depicted schematically in Fig. 1.1(b). Pictured here are the first two mode shapes, which serves to show the potential complexity of the dynamic response for such a multi-degree of freedom system. The resistance to the dynamic loads is provided by the anchor bolt system, with each anchor bolt sharing the base shear, and with resisting moments in the form of either direct tension or compression as shown in Fig. 1.1(c).

Fig. 1.1(d) and 1.1(e) respectively present the random nature of the wind speed V and direction θ. These plots are from actual data obtained during the course of this study and result in a power spectral density function shown in Fig. 1.1(f). This input motion leads to a random, but harmonic-like, dynamic response shown in the time domain in Fig. 1.1(g), which results in narrow-banded frequency response. Due to the variability of wind speed and direction, the stress ranges in the anchor bolts are of course not constant and presumably lead to a probability density function of stress ranges shown in Fig. 1.1(h).

The problem, therefore, can be considered as one of random input Fig. 1.1(i), resulting in output Fig. 1.1(j), which can thus be synthesized in either the frequency or time domain, Fig. 1.1(k), and related to a fatigue S-N damage function Fig. 1.1(l).

Consideration of fatigue resistance, depicted in Fig. 1.1(l), raises the question of the

appropriate category S-N curve to use, and whether a fatigue (stress) limit should be considered to apply. A number of studies reported in the literature indicate that a fatigue limit does not exist in many variable-amplitude fatigue loading situations.

The fluctuation of wind speed and direction, although a stochastic process, also poses further problems relating to response analysis. For example, changes in wind speed and/or wind direction lead to changes in along-wind drag coefficients, projected areas, and hence dynamic pressures. The possibility of aeroelastic lock-in and across-wind effects due to vortex shedding also pose additional complexity.

It is evident from the foregoing discussion that due to the immense uncertainty associated with the structural loading, reliable prediction of the response leads to a virtually intractable problem.

1.3 THE SOLUTION TECHNIQUE TO THE PROBLEM AND THE SCOPE OF THIS REPORT

Herein we adopt a dual experimental and analytical approach to the problem solution. It is considered that both approaches are necessary, as one without the other would only give a partial insight as to the cause of the fatigue in the anchor bolts.

The central west light pole was selected for this study. This pole was chosen for three principal reasons: it was close to the press box and thus conveniently located for housing the required instrumentation and computerized data acquisition system; the pole had a selection of ultrasonic indications indicating possible high, medium and low degrees of damage; and this pole had virtually unobstructed view in the direction of the incoming prevailing wind. The latter reason was considered important for minimizing any uncertainty associated with the wind loading. Fig. 1.2 shows elevation views of the light pole.

Section 2 firstly describes the framework of the problem and sets forth the theoretical basis for a comprehensive solution. Interrelationships are presented between: applied probabilistic wind load; the along-wind and across-wind dynamic response of the pole structure; and the fatigue induced damage resulting from the applied loadings.

Section 3 outlines the experimental program and presents the principal details required to determine: applied wind loading; dynamic repsonse; and strain induced damage in the anchor bolts.

In Section 4, the results of the experimental study are presented. The results are corroborated by analytical predictions based on measured wind speeds and direction time histories. Differences between the two approaches explain the significance of across-wind response and site-specific (stadium) load (gusting) dependence. The dual experimental-analytical approach makes it possible to derive structure dependent damage density functions for each of the instrumented bolts and hence derive first fatigue crack life

predictions. Inferences of post fatigue crack life are also made, employing experimental and analytical fracture mechanics techniques.

Section 5 describes a three step fatigue mitigation proposal. The first two of these steps are relatively simple and should be employed as early as practicable. The third measure is to provide for improved longevity of the pole and to ensure that the fatigue problem will not transfer itself to another location such as the pole to base plate welds.

Finally, conclusions pertaining to this study are drawn and recommendations made regarding necessary follow-up work.

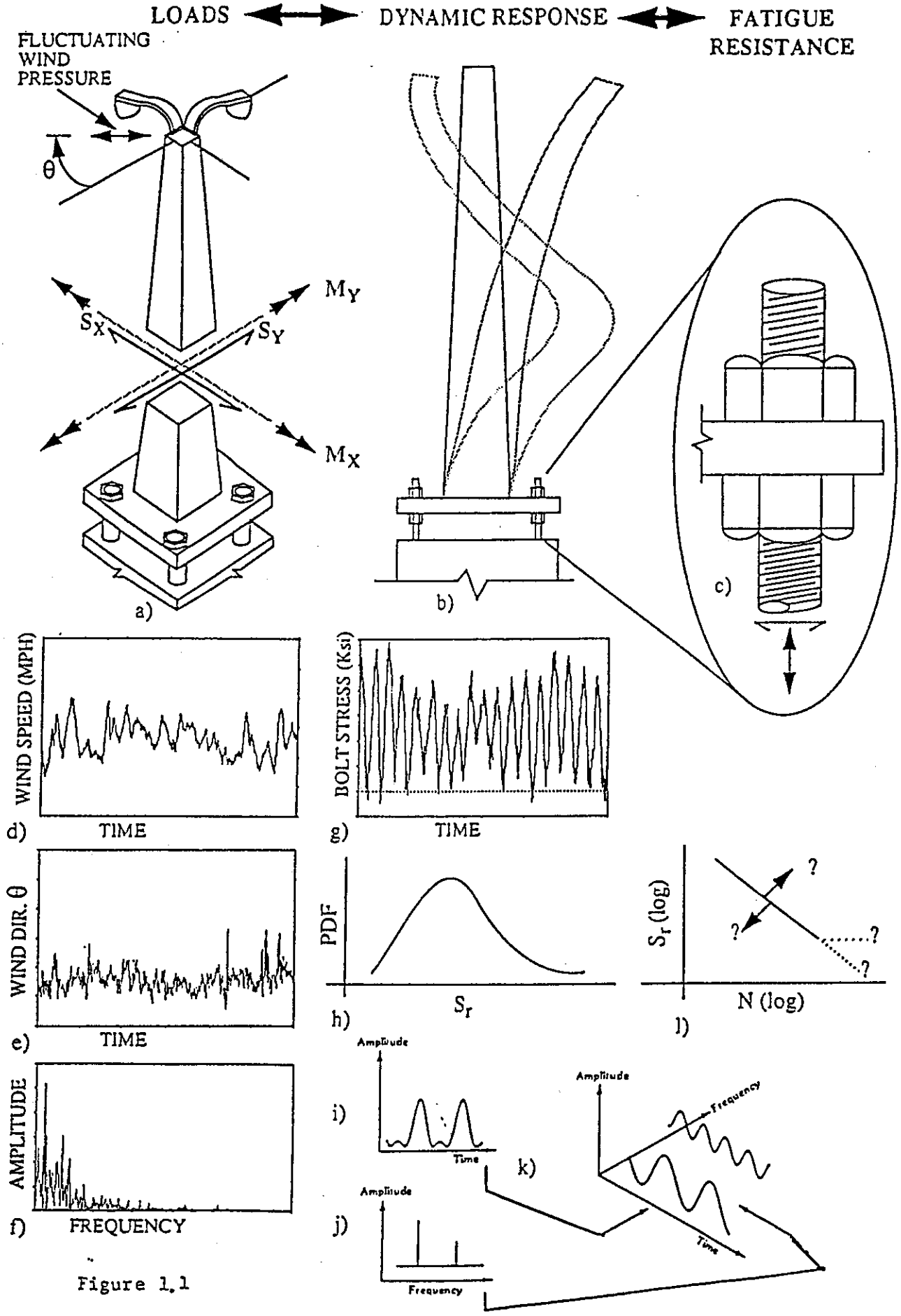
LOADS
DYNAMIC RESPONSE
FATIGUE RESISTANCE
FLUCTUATING WIND PRESSURE
θ
S_X
S_Y
M_Y
M_X
a)
b)
c)
WIND SPEED (MPH)
TIME
d)
BOLT STRESS (Ksi)
TIME
g)
WIND DIR. θ
TIME
e)
PDF
S_r
h)
S_r (log)
N (log)
?
?
?
?
l)
AMPLITUDE
FREQUENCY
f)
Amplitude
Time
i)
Amplitude
Frequency
Time
k)
Amplitude
Frequency
j)

Figure 1.1

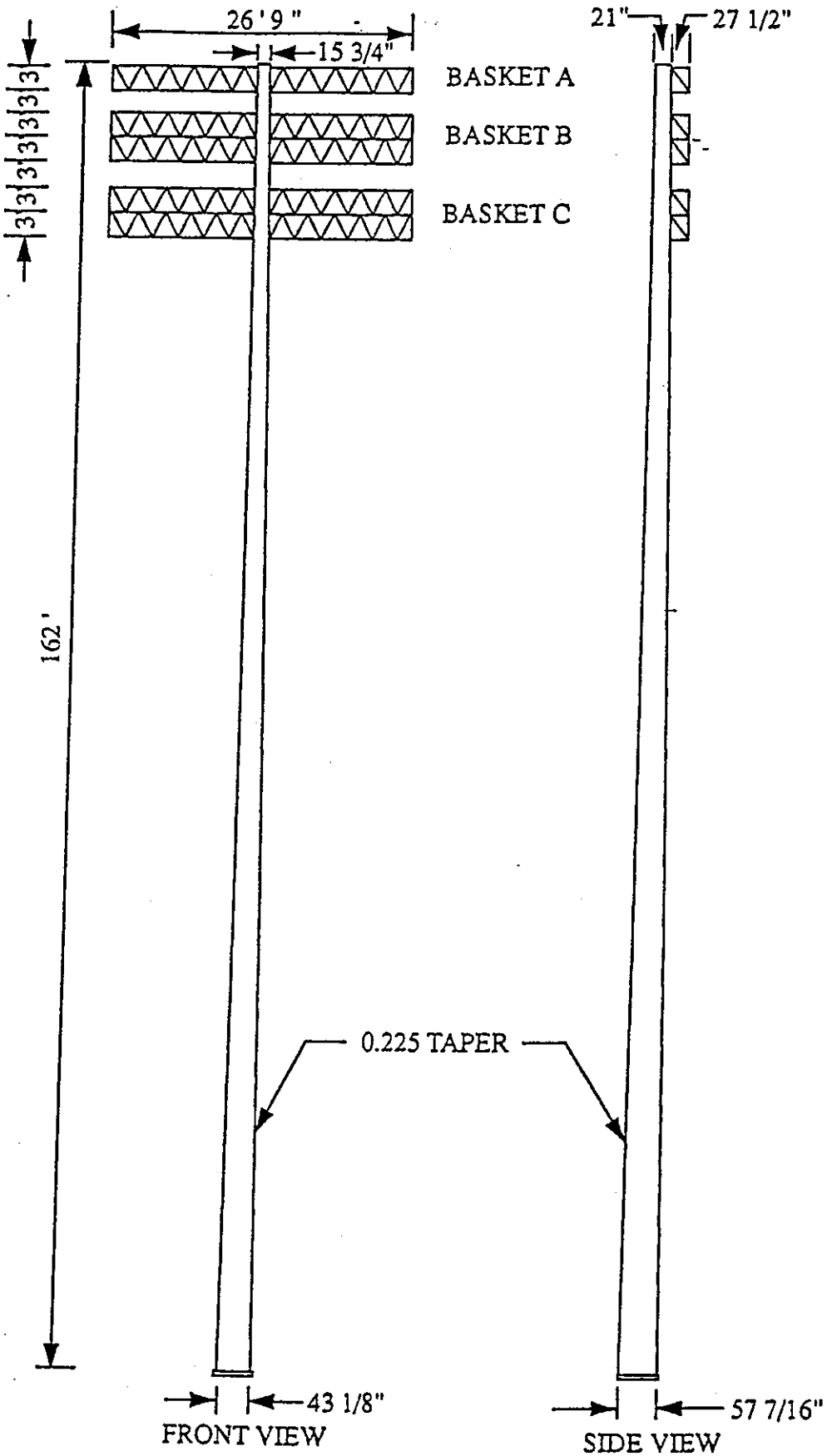

Fig. 1.2 : Elevation of the Light Pole

SECTION 2

WIND LOADS AND THEIR EFFECT ON POLE STRUCTURES: THEORETICAL CONSIDERATIONS

2.1 INTRODUCTION

This section sets forth the basis for the dynamic response and hence the vibration induced fatigue and fracture mechanics of pole type structures. Firstly the forces induced on a pole by steady and unsteady winds is discussed. This is followed by a theoretical development which leads to the solutions of the equations of motion in both the frequency and time domain. A discussion is then presented on implications pertaining to wind gusting and the basis of *AASHTO* and *ANSI* code based gust factors. A relationship between gusting and stress cycling is then derived. High cycle fatigue which leads to initial cracking due to stress cycling is then discussed. This is followed by a discussion of fracture mechanics which pertains to the post-cracking life till failure. Finally the wind environment in the Buffalo area is analyzed in terms of its transient nature and extreme wind climatology and is related to fatigue and fracture damage.

These theoretical results are employed in section 4 for interpreting and utilizing the experimental results obtained from the site.

2.2 WIND LOADS

2.2.1 Steady State Wind Loads

The pressure from a steady wind against a structure can be found from Bernoulli's equation

$$\frac{1}{2}\rho v^2 + p = const. \tag{1}$$

in which p = local pressure, v = velocity in ft/s and ρ is the standard air density which may be taken as 0.0761 pcf at 15° C and 760 mm of mercury. By bringing air to rest against an obstruction in the flow the mean dynamic pressure may be found from

$$P = 0.00256V^2 \tag{2}$$

where P = static pressure in psf and V = approach wind velocity in mph.

A steady wind will induce forces in the along-wind and across-wind directions (F_D, F_L) which are respectively affected by the drag and lift coefficients:

$$F_D = 0.00256C_DV^2B \tag{3}$$

$$F_L = 0.00256C_LV^2B \tag{4}$$

in which B = reference width in ft, C_D = drag coefficient, C_L = lift coefficient and F_D and F_L are respectively drag and lift forces in lb/ft. The drag and lift coefficients are dependent on both shape and Reynolds number R_e, which is given by

$$R_e = \frac{vD}{\nu} \tag{5}$$

where v = velocity in ft/s, D = diameter (or section width B) in ft and ν = kinematic viscosity of air which is 1.46×10^{-5} m^2/s at 15° C at standard air pressure or

$$R_e = 9350Vd \tag{6}$$

where V = velocity in mph and d = diameter in ft.

2.2.2 Along-Wind Forces in a Steady Wind

The relationship of the drag coefficient with Reynolds number is determined experimentally. The mean drag coefficient for a cylinder plotted against Reynolds number is shown in Fig. 2.1 [Simiu 86]. The dependence of a circular section's drag coefficient is due to the change in the wake developed behind the body. At a low Reynolds number the wake is in subcritical flow and C_D = 1.2. As R_e increases, supercritical flow takes place, the wake decreases and the separation point moves from the front to the rear of the body with C_D reducing to about 0.45. The drag coefficient C_D will gradually rise to a plateau of about 0.75 for very high Reynolds numbers.

For other bluff body shapes the drag coefficient is relatively independent of Reynolds number. Square shapes and angle sections, for example, have $C_D \sim 2$. The light pole in this study is idealized as a duo-decagonal ellipse. By interpolation it is therefore possible to derive the appropriate wind direction dependent drag factors.

It may be noted that [*AASHTO 85*] provides drag coefficients that are dependent on the wind speed V. Such a provision is more realistic than other codes which do not vary C_D with wind speed as it takes into account the varying nature of air flow around the pole (i.e.

laminar or turbulent). The pole cross-section was idealized to be elliptical in shape for the purpose of calculating the wind drag coefficients. For such a cross-section, the *AASHTO* code (Table 1.2.5 C, *AASHTO 1985*) specifies different drag coefficients in the two principal directions. In the case of wind blowing at an inclination to the principal axes (Fig. 2.2), the drag factor was derived by interpolating between the two cases using the following function:

$$C_{d\theta} = \sqrt{(C_{db}\sin\theta)^2+(C_{dn}\cos\theta)^2} \tag{7}$$

where, $C_{d\theta}$ = drag coefficient for an arbitrary angle of approach, C_{db} = drag Coefficient for broad-side facing the wind, C_{dn} = drag coefficient for narrow side facing the wind, θ = approach angle of the wind with respect to minor Y-Y axis. The assumed variation of the drag factor with the Reynolds number for different approach angles is shown in Fig. 2.3. The wind pressure was assumed to act on an effective projected area which also depends on the wind direction. The effective projected diameter, d, for an inclined wind was calculated by interpolating between the major and minor diameters of the ellipse using a function similar to the one used for the drag coefficients.

2.2.3 Across-Wind Forces in a Steady Wind

In the wake of along-wind response vortex shedding may take place. For a bluff body vortex shedding approximately conforms to a sinusoidal motion which will produce a harmonic lift force normal to the direction of the wind. This may be expressed as

$$F_L = \frac{1}{2}\rho\ V^2\ B\ C_L\ \sin 2\pi ft \tag{8}$$

in which f = the shedding frequency in Hz that satisfies the Strouhal relationship given by

$$S_n = \frac{f\ D}{v} \tag{9}$$

where D = characteristic dimension which may be taken as the breath of the body projected on a plane normal to the mean flow velocity in ft and v = approach velocity in ft/s.

Thus the harmonic loading function, such that when the structure and Strouhal frequency are equal under a steady state wind the peak transverse wind force will be

$$F_i = \frac{F_L}{2\xi} \tag{10}$$

where ξ = damping coefficient.

The Strouhal number is also shape dependent and may vary from about 0.12 for a square section to 0.2 for a cylindrical section.

2.3 DYNAMIC RESPONSE TO AN UNSTEADY WIND

2.3.1 General Dynamic Behavior

The natural air is unsteady, and the wind load on a structure and its elements fluctuates with time. This is distinct from the aforementioned steady-state across-wind effects that can induce harmonic response transverse to the direction of the wind as a result of vortex shedding. Of particular concern with along-wind response is the effect of wind gusts on the structure and the dynamic structural amplification and possible resonance that may arise leading to high stresses and possible yielding under extreme wind loads. Also of concern is the general transient nature of the wind at lower wind velocities which causes strain cycling and consequently may induce high cycle fatigue.

Consider a structure that can be idealized as an equivalent single degree of freedom (SDOF) system. From Newton's second law of motion the governing equation of motion is given by

$$m\ddot{x} + c\dot{x} + kx = F(t) \tag{11}$$

where F(t) = time dependent load acting on the structural mass m of stiffness k and structural damping c, and x, $\dot{x}$, and $\ddot{x}$ are the displacement, velocity and acceleration respectively. For convenience Eq. 11 may be rewritten as

$$\ddot{x} + 2\xi\omega_n\dot{x} + \omega_n^2 x = \frac{F(t)}{m} \tag{12}$$

where the natural circular frequency (in rad/s) can be found from

$$\omega_n^2 = k/m \tag{13}$$

and the natural frequency f_n in Hz

$$f_n = \frac{\omega}{2\pi} \tag{14}$$

and the damping ratio

$$\xi = c / c_c \tag{15}$$

where c_c = critical damping ratio defined as

$$c_c = 2\sqrt{km} \tag{16}$$

There are two distinct approaches to the solution of the equation of motion (Eq. 12). Such solutions are either in the *frequency* or *time* domains and are explained in the following two subsections.

2.3.2 Frequency Domain Solution

Consider a steady state response to forced harmonic loading such that

$$F(t) = F_o \cos\omega t \tag{17}$$

where F_o = peak force and ω is the cyclic forcing frequency in rad/s. Then the steady state solution is given by

$$x(t)=F_o H(\omega)\cos(\omega-\phi) \tag{18}$$

where the phase angle ϕ is given by

$$\tan\phi = \frac{2\xi(\omega/\omega_n)}{1 - (\omega/\omega_n)^2} \tag{19}$$

and

$$|H(\omega)|^2 = \frac{1}{\omega_n^4 m^2} \frac{1}{[1 - (\omega/\omega_n)^2]^2 + 4\xi^2(\omega/\omega_n)^2} \tag{20}$$

where $|H(\omega)|^2$ is referred to as the transfer function which is the square of the dynamic magnification factor for harmonic loading. For a system responding to a random loading complying with wide band white noise such that

$$S(\omega) = S_o \tag{21}$$

where $S(\omega)$ = response spectrum and S_o = Amplitude at frequency ω. Then the mean square of the resonant response is given by

$$\sigma_x^2 = \frac{S_o}{8\ \omega^3\ m^2\ \xi} \tag{22}$$

Real winds, however, do not necessarily follow wide-band white noise. Rather, a decaying spectrum is appropriate as shown in Fig.2.4.

Therefore, it can be shown [Simiu & Scanlan 86] that

$$\sigma_x^2 = \int_0^\infty S(\omega)|H(\omega)|^2 d\omega \approx \frac{1}{\omega^4 m^2} \int_0^\infty S(\omega) d\omega + \frac{S(\omega_n)}{8\xi\omega_n^3 m^2} \tag{23}$$

The first and second parts of the right hand side of the above equation are generally referred to as the background and resonant part of the response, respectively. It should be noted that the integral in the first part is merely the area beneath the power spectral density curve. Of particular concern is the moment at the base of the pole structure, as this is what primarily induces the stresses in the anchor bolts. After converting from generalized displacements into base moments Eq. 23 becomes

$$\sigma_m^2 = \int_0^\infty S_m(\omega)d\omega = \int_0^\infty |H(\omega)|^2 S_m(\omega)d\omega + \frac{\omega_n S_m(\omega_n)}{8\xi}$$

thus

$$\sigma_m^2 \sim \frac{\omega_n S_m(\omega_n)}{8\xi} \qquad (25)$$

It will be shown later how this response quantity is associated with measures of high cycle fatigue.

2.3.3 Time Domain Solution.

If a displacement time-history can be derived either from direct physical measurement or analytically based on a known applied loading, then reaction forces and stresses can be computed. From the stress history inferences can be made regarding the rate of fatigue damage accumulation as a function of the applied transient loads or wind speed. Using measured wind speeds it is possible to compute applied along-wind forces F(t) using Eqs 3 and 7. Changes in applied forces over small time steps can be employed directly into an incremental form of Eq. 12, thus

$$\Delta\ddot{x} + 2\xi\omega_n \Delta\dot{x} + \omega_n^2 \Delta x = \frac{\Delta F(t)}{m} \qquad (26)$$

where Δ denotes a change over a small time-step.

There are a number of numerical schemes that can be used to solve this initial-value differential equation of motion. Herein we use the well known Newmark-beta scheme [Clough & Penzien 76] due firstly to its simplicity in programming, and secondly for its unconditional stability when extended to non-linear problems. Although material (stress-strain) or geometric (P-delta) non-linearities were finally not encountered in this study it was initially believed that such non-linear behavior could have contributed to fatigue damage. Moreover, possible fatigue mitigation schemes could employ added non-linear visco-elastic type damping and the present program is easily extended to accommodate such behavior.

2.4 THE GUSTING EFFECTS OF AN UNSTEADY WIND

2.4.1 Gust Relationships

The response moment M(t) at the base of the pole is assumed to be normally (Gaussian) distributed which can be described by its standard deviation $\sigma_m = M_{std}$ and mean value M_{avg}. Since damping is low and the response narrowly banded, the response can be assumed to comply with random vibration theory with randomly varying amplitude and phase angle. The cycling peaks are of interest and it has been shown previously [Simiu & Scanlan 85] that these peaks conform to a Rayleigh probability density function. The largest peak value can be derived from

$$M_{max} = M_{avg} + \beta_p M_{std} \tag{27}$$

where β_p = peak factor. Assuming a Rayleigh distribution the peak factor β_p is calculated from

$$\beta_p = \sqrt{2 \ln(f_n \tau)} + \frac{0.5772}{\sqrt{2 \ln(f_n \tau)}} \tag{28}$$

in which f_n = natural frequency ($\omega_n/2\pi$), τ = duration of loading or the averaging period. For example averaging the present poles over 5 and 60 minutes would respectively result in the peak factors of 3.2 and 3.9.

It is evident that Eq. 28 can be related to gust factors used in code based design. The response of a system to a turbulent wind can be expressed in the general form

$$M_{max} = G_m M_{avg} \tag{29}$$

where M_{max} = maximum wind induced base moment from gusting, M_{avg} = mean base moment equivalent to a steady wind load and G_m is gust response factor defined as

$$G_m = 1 + \frac{\beta_m M_{std}}{M_{avg}} \tag{30}$$

where $M_{std} = \sigma_m$ = root mean square (standard deviation) of the fluctuating base moment.

For an elastic pole structure, base moments and anchor bolt stresses are directly proportional, thus

$$\sigma_{max} = G_m \sigma_{avg} \tag{31}$$

where σ_{max} and σ_{avg} are the maximum and mean anchor bolt stresses, respectively. The gust factor may be determined either by (a) empirical means from code formulations, (b) experimentally from wind tunnel tests, or (c) from field tests. For the latter case strain/stress measurements can be taken and response quantities computed to experimentally find β as follows:

$$\beta = \frac{\epsilon_{max} - \epsilon_{avg}}{\epsilon_{std}} \tag{32}$$

from which an experimental gust factor can be determined as:

$$G_\sigma = 1 + \beta \frac{\epsilon_{std}}{\epsilon_{avg}} = \frac{\epsilon_{max}}{\epsilon_{avg}} \tag{33}$$

2.4.2 Code Gust Factors

As part of this project two code type formulations were considered. These are described as follows:

(1) AASHTO Standard Specification for Structural Supports for Highway Signs, Luminaries and Traffic Signals, 1985

The wind pressure in this code is computed by the following formula

$$P = 0.00256(1.3V)^2 C_d C_h \tag{34}$$

where P = wind pressure in psf, C_h = height coefficient which converts the wind pressure from a standard height of 30 ft to the height under consideration, C_d = drag factor and V = wind velocity in mph. The coefficient in the above equation is said to be the gust speed, which implies a constant gust factor of 1.69 to be used for all structures covered by this code.

(2) ANSI A58.1 - 1982

In this code the velocity pressure q_z in psf, at height z, is calculated from the formula:

$$q_z = 0.00256 K_z (IV)^2 \tag{35}$$

where V = basic wind speed in mph, I = an importance factor normally assumed to be 1.0 except for important structures and those in hurricane prone areas and K_z = a velocity exposure coefficient (similar to C_h above).

Gust response factors are then explicitly employed to account for the fluctuating nature of wind and its interaction with main wind - force resisting system of the structure through the factor G_h. This factor is exposure (roughness) dependent. For example, in Exposure category C for open terrain with scattered obstructions up to 30 ft in height, including open country and grasslands, the gust factor G_h varies from 1.13 at 160 ft to 1.32 at ground level.

For main wind force resisting systems of flexible structures, the gust factor $\overline{G}$ is calculated through a rational analysis as described by clause A6.6.1 of the *ANSI* code. For the Rich Stadium Light Poles $\overline{G}$ varies from 4.306 to 1.709 for low to high wind speeds in the strong axis direction and 3.933 to 1.618 in the weak axis direction. Determination of the *ANSI* Code gust factor $\overline{G}$ is performed in Appendix 1. The *ANSI* code has recently been re-issued as the *ASCE 7-88* code [ASCE 90] with no changes in the gust factor provisions applicable to the Rich Stadium Light Poles.

2.5 FATIGUE CONSIDERATIONS

2.5.1 Present Design Requirements

The unsteady nature of the wind loading in the along-wind direction as well as forced harmonic across-wind loading due to vortex shedding lead to dynamic pole response that causes stress cycling in the structural elements. Such stress cycling over a sustained period of time may lead to fatigue damage in welded and/or bolted connections.

Such a problem is alluded to in the *AASHTO* code, but only for across-wind response where resonance under a steady critical wind velocity may occur. This velocity is computed by

$$v_c = \frac{f_n \, d}{S_n} \tag{36}$$

in which f_n = natural frequency in Hz, S_n = Strouhal number taken as 0.18 for circular sections and 0.15 for multi-sided sections, v_c = critical velocity in ft/s and d is approach width normal to the wind.

The transverse pressure is calculated from

$$P_L = \frac{P}{2\xi} \tag{37}$$

where ξ = damping ratio and P = wind pressure calculated for v_c (without the 1.3 gust speed amplifier). The *AASHTO* code gives guidance for how to cope with tapered members. Designers are then required to check the *AASHTO* "Standard Specifications for Highway Bridges". The code implies that stresses under across-wind effects should be sufficiently low to be below the fatigue limit stress which can sustain at least 2 million cycles.

No guidance is given by the code to designers as to how to cope with fatigue damage if the critical wind velocity producing across-wind response induces stresses greater than the fatigue limit. Presumably the designer would need to strengthen and/or stiffen the design to make the problem disappear!

The inadequacies of current code based fatigue criteria are part of the reason for the experimental investigation and new analytical models developed in the course of the present study.

2.5.2 Fatigue Damage Models

The fatigue life of a material be conveniently expressed in terms of the well known Manson - Coffin equation [Manson 1953 and Coffin 1954] which states

$$\epsilon_a = \frac{\sigma'_f}{E} (2N_f)^b + \epsilon'_f (2N_f)^c \qquad (38)$$

in which ϵ_a = strain amplitude, N_f = number of cycles to failure (first crack), $2N_f$ = number of reversals, E = Young's Modulus and σ'_f, ϵ'_f, b and c are material constants determined by tests for a given material.

The first and second parts of the right hand side of the Manson - Coffin equation respectively model high cycle (low stress range) fatigue and low cycle (high strain range) fatigue. The former and latter primarily represent elastic and inelastic material behavior.

For elastic design where inelasticity is unlikely to occur, the equation can be simplified to give

$$\frac{S_r}{2} = \sigma_a = \sigma'_f (2N_f)^b \qquad (39)$$

where S_r = total stress range and σ_a = stress amplitude.

The primary effect of fatigue life in this equation is governed through the exponent b. This may vary from -0.08 to -0.12 for mild steel reinforcing bars and lead to a relatively long life. For steel with welded connections and possible flaws, as well as threaded bolts this exponent may increase to -1/3 which implies a more restricted high cycle fatigue life. According to studies by Frank (1980) b = -1/3, thus inverting Eq. 34 gives a modified form of the Manson-Coffin equation in the *AASHTO bridge* code format as:

$$N_f = AS_r^{-3} \tag{40}$$

where A = *AASHTO* fatigue category coefficient. Frank recommended that category C fatigue be applicable for double nutted bolts, thus A = 4.443×10^9 [Keating and Fisher 86].

The accumulation of fatigue can be described by a number of damage models. The simplest of these and probably still the best for either constant amplitude or completely random loading is Miner's Rule. Damage D_i, for the i^{th} cycle of loading can be expressed as

$$D_i = 1 / N_f \tag{41}$$

where N_f is given by Eq. 40.

Over a period of time t the total damage is summed as follows

$$D_t = \Sigma D_i = \Sigma 1/N_f \tag{42}$$

Normally for a given cycle if S_r is less than the fatigue stress limit the damage fraction for

that cycle is ignored. However test data suggests that such a limit may not exist under variable amplitude loading. In the present study no fatigue limit has been assumed.

It is generally not possible to determine all damage fractions over the entire structural life. Instead samples may be taken that are representative of the response under different wind loading conditions and the damage fraction for that response computed. An experimental relationship can then be established between wind velocity (with preferably directional dependence) and the rate of damage accumulation. Thus by knowing the effective constant amplitude stress range for an entire (average) year, it is possible to calculate the number of years of life to the occurrence of first fatigue crack. For one year

$$D_1 = \frac{n}{N_f} = \frac{24*60*60*365.25\, f_n}{A\, S_r^{-3}} \tag{43}$$

here f_n = the nominal damaging frequency that is used in the rainflow counting method (described below) to determine the effective stress range S_r. The number of years to fracture is therefore $T_f = 1/D_1$ which leads to

$$T_f = \frac{A}{31.6x10^6\, S_r^3\, f_n} \tag{44}$$

Thus for Category C fatigue

$$T_f = \frac{140}{S_r^3\, f_n} \tag{45}$$

What follows is a description of how the effective annual stress range is determined for a given bolt based on either experimental observations or analytical predictions.

2.5.3 Stress Amplitude and Cycle Counting Analysis

Under random wind loading the main concern then becomes how to count the strain (stress) cycles that contribute to damage. A number of cycle counting methods have been proposed in the literature which include; the peak - to - peak method; the zero crossing method, energy based equivalent harmonic process [Kliman 85] and the rainflow method. The latter method was used in this study to count cycles and to determine stress amplitudes. Although computationally cumbersome it is considered to give good results.

The rain flow method has become popular and has been frequently applied to variable load problems [Fisher at. el. 89, Whittaker at. el. 69]. The method assumes plasticity at the crack tip and counts hysteresis loops on the stress strain diagram for material in plastic zone. The relationship between a nominal stress-time plot and a stress-strain hysteresis plot at the crack tip where plasticity has developed is seen by comparing Fig. 2.5 with Fig. 2.6. [Fisher at. el. 89].
The stress-time curve can be seen to have 3 half cycles, a-d, d-e and e-f, and one full cycle, b-c-b'. The same results are obtained by using the analogy of rain running down a series of pagoda roofs.

The general rules for rainflow counting are as follows:

1) Rain flow begins at the beginning of the stress response and successively at the inside every peak.

2) Flow initiated at a maximum drips down until it comes opposite a maximum more positive than the one from which it started. Flow initiating at a minimum drips down until it come opposite a minimum more negative than the minimum from which it started.

3) Rain flow stops when it meets rain flow from the roof above.

4) The beginning of the sequence is a maximum if the initial straining is in tension.

5) The horizontal length of each rain flow is counted as a half cycle at that stress range.

In Fig. 2.7, strain initials at a, flows to b, drips to b', flows to d and finally stops opposite e, because e is more negative than a. Rain flow initiating at c, stops at b' where it meets rain flow dripping from b. Rain flow initiating at d flows to e and stops at the end of the record, and flow initiating at e flows to f and stops at the end of the record.

Once cycles have been computed and the strain amplitude determined, it is then necessary to determine a damage-equivalent constant stress amplitude σ_a. This is found for a sample by considering Eqs. 39 and 41, where

$$\frac{D_{random}}{D_{constant}} = \frac{\sum_{1}^{n} \sigma_{ai}^{-1/b}}{n\ \sigma_{ae}^{-1/b}} = 1 \tag{46}$$

Thus,

$$\sigma_{ae} = \left(\frac{1}{n} \sum_{1}^{n} \sigma_{ai}^{-1/b} \right)^{-b} \tag{47}$$

For the present study b = -1/3, hence in terms of stress range.

$$S_{re} = \left(\frac{1}{n} \sum_{1}^{n} S_r^3 \right)^{1/3} \tag{48}$$

Herein this is referred to as the *root mean cube* or RMC stress range

It should be noted that if b = -0.5 as in the case for low cycle fatigue then Eq. 47 by

definition is the standard deviation of the peaks of the stress response. If all points in a time history, rather than just the peaks are used, then it can be shown that

$$\frac{S_{re}}{2} = \sigma_{ae} = \sqrt{2}\sigma_{std} \tag{49}$$

where σ_{std} = standard deviation or RMS of the response. This is a simple and convenient alternative to the rainflow method of analysis. Data analysis programs such as DADiSP and spreadsheets have intrinsic functions that can automatically generate the standard deviation of a time-history response.

Furthermore the standard deviation of the response can be computed from the frequency domain autospectrum using Eq. 23. These two methods serve as an independent check on the rainflow analysis for the deformation of S_r.

2.6 POST-CRACKING FATIGUE CRACK PROPAGATION

2.6.1 Overview of Fracture Mechanics Principles

The foregoing fatigue considerations address only the pre-cracking stage of fatigue behavior of the pole and anchor bolts. This subsection presents approaches appropriate to the post-cracking assessment of the anchor bolts.

Even when fatigue life is used up, resulting in the presence of these cracks, there can often be a significant period of stable crack growth before fracture (unstable crack growth) of the cracked component occurs. In order to quantitatively assess this post-cracking fatigue, principles from fracture mechanics [Barsom and Rolfe 87] must be utilized, in conjunction with nondestructive testing techniques. An overview of relevant fracture mechanics principles and parameters is provided in this subsection. It is essential to note in the following that although a recognized methodology exists for quantifying post-cracking fracture susceptibility, uncertainties in the numerical values of several key parameters mean that results must not be regarded as precise values, rather treated in a qualitative sense.

Fracture Mechanics of Plates:

The basis of fracture mechanics theory has been developed and calibrated for cracked steel plates. This standardized theory provides a quantitative way to relate the primary factors influencing the fracture susceptibility to crack size. The classic case consists of a through-thickness crack of length $2a$ in a wide plate, for which the design requirement is

$$K_1 = \sigma\sqrt{\pi a} \qquad \leq K_c \tag{50}$$

in which σ = peak stress, a = crack size, K_1 = stress intensity factor, and K_c = material fracture toughness. Further explanation of these parameters is given below.

Crack size (a).

A brittle fracture, were it to occur, would initiate from a notch or other discontinuity, in this case the suspected fatigue crack. The larger the crack size is, the smaller is the stress level that can be tolerated before fracture would occur.

Stress level(σ).

In order for brittle fracture to occur, tensile stresses must be present. Such stresses arise in the light pole anchor bolts in order to resist overturning moments. For this analysis, σ designates the nominal tensile stress on the cross section of the bolt in question. Under observed wind conditions at the site, σ can be inferred directly from the strain gauge on the bolt.

Material Toughness (K_c).

The material toughness in the presence of a crack is known as the fracture toughness, K_c. It can be thought of as the ability of the material to carry load in the presence of a crack and is a function of material composition, specimen thickness and geometry, stress state and stress gradient, and loading rate.

Eq. 50 is the basic form of the requirement for preventing fracture in members with flaws, analogous to the requirement that $\sigma \leq \sigma_y$ to prevent yielding in members without flaws, where σ_y is the yield stress. The stress intensity factor, K_1, varies with both the applied load level and the crack length.

Fracture Mechanics of Bolts:

For a crack in a bolt, the expression for K_1 must be adjusted to account for crack and specimen geometry and loading conditions that differ from those of the standard through-thickness crack in a plate. Thus, the general expression for K_1 becomes

$$K_1 = Y\sigma\sqrt{\pi a}, \tag{51}$$

which is in units of ksi$\sqrt{in}$, (or MNm$^{-3/2}$ in SI units where 1.0 ksi$\sqrt{in}$ = 1.099 MNm$^{-3/2}$). Y is a correction factor, determined experimentally/analytically. Empirical polynomial curve fits to observed experimental and/or analytical FEM/BEM solutions may be found in the literature. In this study of cracked bolts, several different crack geometries are considered, these are described below.

1) Straight crack front: Fig. 2.8 shows an actual bolt that developed a straight crack front. The correction factor for this crack geometry may be given as

$$Y = 0.926 - 1.771\left(\frac{a}{D}\right) + 26.421\left(\frac{a}{D}\right)^2 - 78.481\left(\frac{a}{D}\right)^3 + 87.911\left(\frac{a}{D}\right)^4 \tag{52}$$

where D = bolt diameter, taken as 2 inches at the thread root.

2) Semi-circular crack front: Fig. 2.9 shows an actual bolt that developed a crack of this sort. Experimental studies have shown that in many cases, the crack front transitions from semi-circular to a straight front. This is illustrated in Fig. 2.10, where a semicircular crack of size a_1 grows to one of size a_2. As a_2 approaches a value of 0.5, the crack front is assumed to become straight. The correction factor for this crack geometry and assumed propagation is given as [James and Mills 88]:

$$Y = 2.043\, e^{-31.332\frac{a}{D}} + 0.6507 + 0.5367\frac{a}{D} + 3.0469\left(\frac{a}{D}\right)^2 - 19.504\left(\frac{a}{D}\right)^3 + 45.647\left(\frac{a}{D}\right)^4 \tag{53}$$

3) Sickle-shaped crack front: Fig. 2.11 shows an actual bolt that developed a crack of this sort. The correction factor for this crack geometry is given as [Mattheck et. al. 85]:

$$Y = 1.1215 + 0.1664\frac{a}{R} + 5.1396(\frac{a}{R})^2 - 15.932(\frac{a}{R})^3 + 24.746(\frac{a}{R})^4 - 10.986(\frac{a}{R})^5 \quad (54)$$

which is valid for $0 \le a/R \le 1$, where R = bolt radius, taken herein as 1 inch.

4) Annular crack front: The correction factor for this class of crack front can be expressed as [Hertzberg 89]:

$$Y = \frac{1}{\sqrt{a/D}}\left(\frac{0.762155}{1-2a/D} - 0.56275\right) \quad (55)$$

Since neither ultrasonic nor acoustic emission nondestructive testing techniques directly quantify the flaw size or shape, these four different potential crack geometries should be investigated in an assessment of a cracked bolt. Each has different Y and a values corresponding to it.

Another important parameter with uncertain numerical value in this study is the fracture toughness. The fracture toughness, K_c, is not a constant for a given material. It is adversely affected by high strain rate, low temperature, and specimen size. Static loading is normally considered to have a strain rate of approximately $\dot{\varepsilon} = 10^{-5}$ sec^{-1}, while for fracture toughness testing purposes dynamic loading corresponds to a strain rate of approximately 10 sec^{-1}. For the pole's first mode-dominated load cycling at 0.3 Hz, the strain rate is approximately 10^{-4} sec^{-1}. Thus, it is reasonable to consider the loading to be essentially static, so that static values of K_c may be used directly. The plane strain static value of fracture toughness, K_{Ic}, would be a reasonable lower bound.

Firm values of K_{Ic} for the anchor bolt steel, unfortunately, are not available. This steel, Grade 75 ASTM A615, is no longer manufactured. The most recent ASTM specification for this steel (1968) predates the routine specification of chemical composition and fracture toughness requirements which are more common in current practice. By

comparing to K_{Ic} values for other carbon steels and assuming -20° F as a worst-case temperature, a value of 60 ksi$\sqrt{in}$ appears to be a reasonable lower-bound value and is employed in subsequent analyses.

2.6.2 Crack Propagation

The problem with proof tests of a suspected damaged bolt is that a successful proof test would prove only that a flaw of critical dimensions did not exist at the time of the test. No guarantee can be made that the flaw would not propagate (grow) during further cyclic loading (caused by swaying of the pole due to wind loading) to the critical size at which fracture would occur [Hertzberg 89].

Cyclic loading (as reflected in the stress range, S_r, or $\Delta\sigma$), produces crack propagation if the magnitude of the stress range is beyond a certain threshold. Fig. 2.12 shows the typical form of fatigue crack propagation data for a specimen with an initial crack size of a_0. This figure illustrates that crack growth rate (measured by the slope of either curve) increases with increasing crack length, and that most of the useful fatigue life is expended when the crack is small. For values of ΔK above the threshold ΔK_{Th} shown in Fig. 2.13, it has been found that fatigue crack propagation can be predicted from the power law equation

$$\frac{da}{dN} = C(\Delta K)^m \tag{56}$$

where for carbon steels like that used in the anchor bolts and ksi$\sqrt{in}$ units, C = 3.6 x 10^{-10}, and m = 3.0. In this equation ΔK = the stress intensity factor range, defined by $\Delta K = Y\Delta\sigma\sqrt{\pi a}$. For large threaded fasteners such as the anchor bolts in question, the fatigue crack growth threshold, ΔK_{Th}, has not yet been established [Fisher 91].

The analysis of crack propagation can be performed by integrating the power law equation, using the starting and final flaw size, respectively, as limits of integration:

$$N_f = \int_0^{N_f} dN = \int_{a_0}^{a_f} \frac{da}{C(\Delta K)^m} \tag{57}$$

If the correction factor, Y, does not change within the limits of integration, the resulting expression for remaining fatigue life is

$$N_f = \frac{2}{C Y^3 \Delta\sigma^3}\left[\frac{1}{\sqrt{a_0}} + \frac{1}{\sqrt{a_f}}\right] \tag{58}$$

where a_0 = the initial flaw size, and a_f = the final flaw size corresponding to the fracture condition defined by setting $K = K_{Ic}$ for the expected peak stress. It is evident from this equation that the remaining fatigue life is highly dependent on the initial flaw size.

Where the correction factor, Y, does change with changes in flaw size, the integration of the power law equation can be performed numerically. The increment of remaining fatigue life, ΔN, corresponding to a further increment of crack growth, Δa, is

$$\Delta N = \frac{\Delta a}{3.6*10^{-10}\left(Y \Delta\sigma \sqrt{\pi a_{avg}}\right)^3} \tag{59}$$

where a_{avg} is the average crack size during this particular growth increment. The quantity in parentheses is ΔK. Here, too, it is evident that the remaining increments of fatigue life are highly dependent on the initial flaw size.

Non-destructive testing techniques are generally unable to be used to directly estimate the initial (current) flaw size. In conjunction with stress ranges calculated from the bolt strain range measurements, however, the current flaw size (a_0) can be inferred from the

equation

$$\Delta K = Y \Delta \sigma \sqrt{\pi a_0} \tag{60}$$

where ΔK is estimated from a non-destructive testing technique such as the acoustic emission method described in section 3 and 4. In order to account for the variable amplitude fatigue stress ranges, a root-mean-cube value is used, similar to that employed in the pre-cracking fatigue analysis. Thus, acoustic emission testing results are employed to estimate ΔK, which is used to infer the initial crack size a_0 from Eq. 60, needed to estimate the remaining fatigue life by numerical integration using Eq. 59. This value, together with a knowledge of probable future stress distribution can be used to obtain an inference of the remaining life until fracture.

2.7 FATIGUE AND FRACTURE IN A WIND ENVIRONMENT

2.7.1 The Buffalo Wind Environment

In order to assess the fatigue life of the bolts, wind records were obtained from the National Weather Service for the twenty year period (1972-1991). A histogram of average hourly wind speeds at 1 knot intervals was generated. This has been normalized and is plotted in Fig. 2.14. This observed distribution conforms well to a log-normal distribution and can be expressed analytically as

$$PDF[V] = \frac{1}{y \ln V_o \sqrt{2\pi}} \exp\left[-0.5\left(\frac{\ln V/V_\mu}{\ln V_o}\right)^2\right] \qquad (61)$$

in which V_μ and V_o are the mean velocity and standard deviation chosen to fit a lognormal distribution. The resulting distribution fitted for the 1972-91 hourly average observations from Buffalo Airport is plotted in Fig. 2.15 and can be expressed as:

$$PDF[V] = \frac{1}{18.2 \ln 1.689 \sqrt{2\pi}} \exp\left[-0.5\left(\frac{\ln V / 7.90}{\ln 1.689}\right)^2\right] \qquad (62)$$

where V = average hourly wind speed in mph.

2.7.2 Wind Induced Fatigue Damage

It has been shown previously herein that for along-wind response the stress range is proportional to the RMS of the dynamic response which is proportional to the wind pressure. Thus, in terms of damage

$$\dot{D} \alpha \ S_r^3 \ \alpha \ V^6 \tag{63}$$

Herein we define the concept of a *Damage Density Function* (DDF) which can be found by multiplying PDF(V) by V^6 and then normalizing, thus

$$DDF[V] \ \alpha \ V^6.PDF[V] \tag{64}$$

This is plotted on Fig. 2.16. From the resulting distribution, it is apparent that a Gaussian distribution will describe well a theoretical *Damage Density Function.* Fitting such a distribution to the data gives

$$DDF[V] = \frac{1}{17.323}\exp\left[-0.5\left(\frac{V-28.27}{8.043}\right)^2\right] \tag{65}$$

Here it will be noted that the DDF has a mean and standard deviation of 28.27 and 8.043 mph respectively.

Another important quantity to define is the effective damaging wind. This is found using Eq. 47 (with b=-1/6) to give $V_{eff} = 18.01\,mph$. It should be noted that this wind, if blowing constantly, would give the same degree of damage as the probabilistic distribution. The significance of the mean damaging wind of 28.27 mph implies that 50% of the fatigue damage is done at speeds greater than this wind, and 50% of damage at speeds less than this wind. Hereinafter this wind will be referred to as $V_{50\%}$.

2.7.3 Extreme Wind Climatology

It is considered important to evaluate the maximum likely stresses that may have occurred over the past 20 years of the pole life, or potentially could occur in say a 50 year

design life. Using the annual maxima data from 1972-1991, it is possible to determine the theoretical probability density function that can describe the extreme winds.

The distribution of annual peak gust velocities is plotted in Fig. 2.17. It should be noted that the horizontal axis is an Extreme Type I (Gumbel) distribution scale. For a Gumbel distribution the return period of the average annual peak gust velocity is 2.33 years. Using a least squares fit to the historic data this distribution can be expressed mathematically as

$$V_T^{gust} = 67.45\ (0.086735 - 0.95459 \ln(\ln(1-1/T_n))) \qquad (66)$$

Note the first coefficient of 67.45 equals the average annual peak gust velocity. Thus for a 50 year return period the peak gust velocity is projected to be 80 mph. This is contrasted with the maximum of 68 mph observed in the period 1972 - 1991. Similarly the annual maximum hourly average wind speed curve can be plotted as an Extreme Type I distribution. This results also conform to a Gumbel distribution and can be expressed as

$$V_T^{avg} = 44.39\ (0.081718 - 0.9572 \ln(\ln(1 - 1/T_n))) \qquad (67)$$

For a 50 year return period the average hourly wind speed therefore is equal to 56 mph. The maximum observed over the life of the pole to date (1972 - 91) is 48 mph.

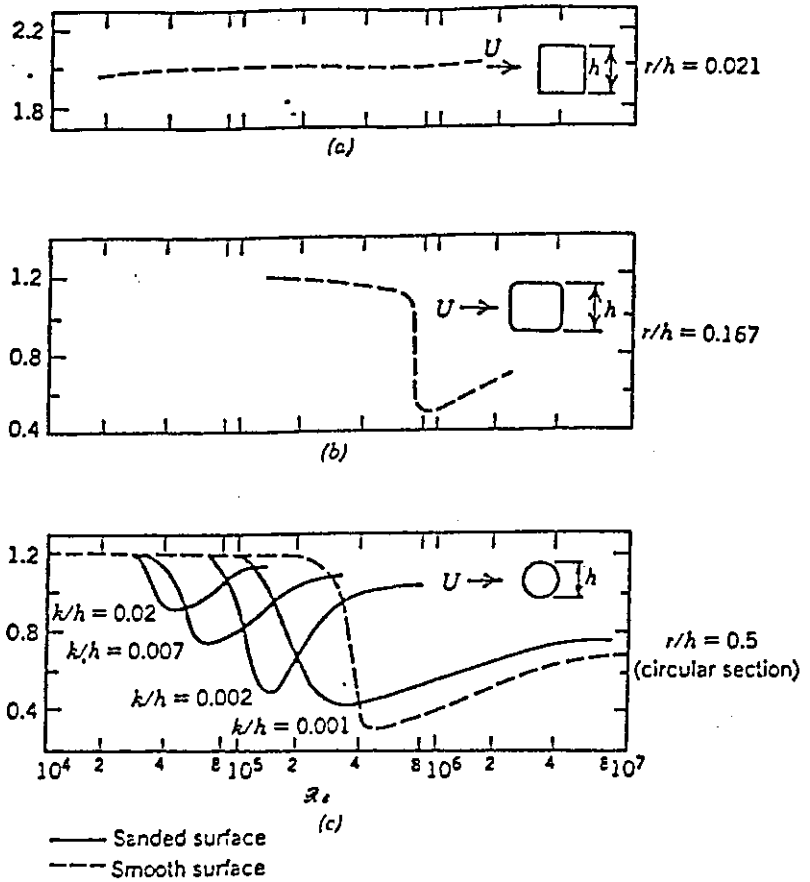

Fig. 2.1 : Influence of Reynolds number, Corner Radius & Surface Roughness on Drag Coefficient [Scruton & Rogers 71]

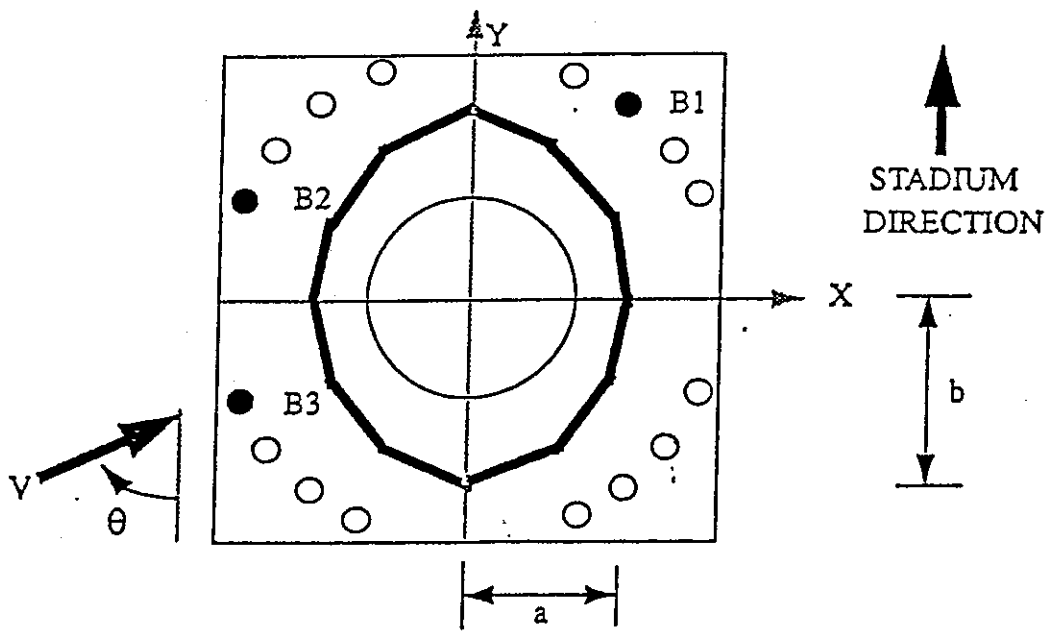

Fig. 2.2 : Reference for Computation of $C_{D\theta}$

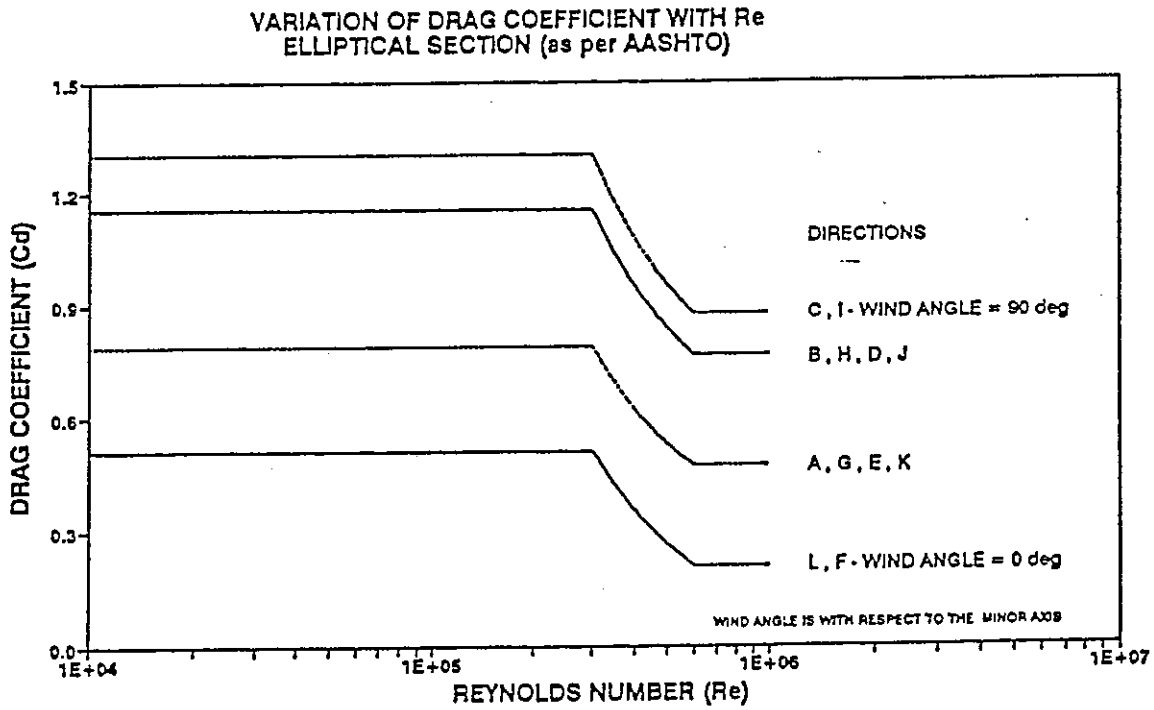

Fig. 2.3 : Influence of Reynolds number on Drag Coefficient for Light Pole

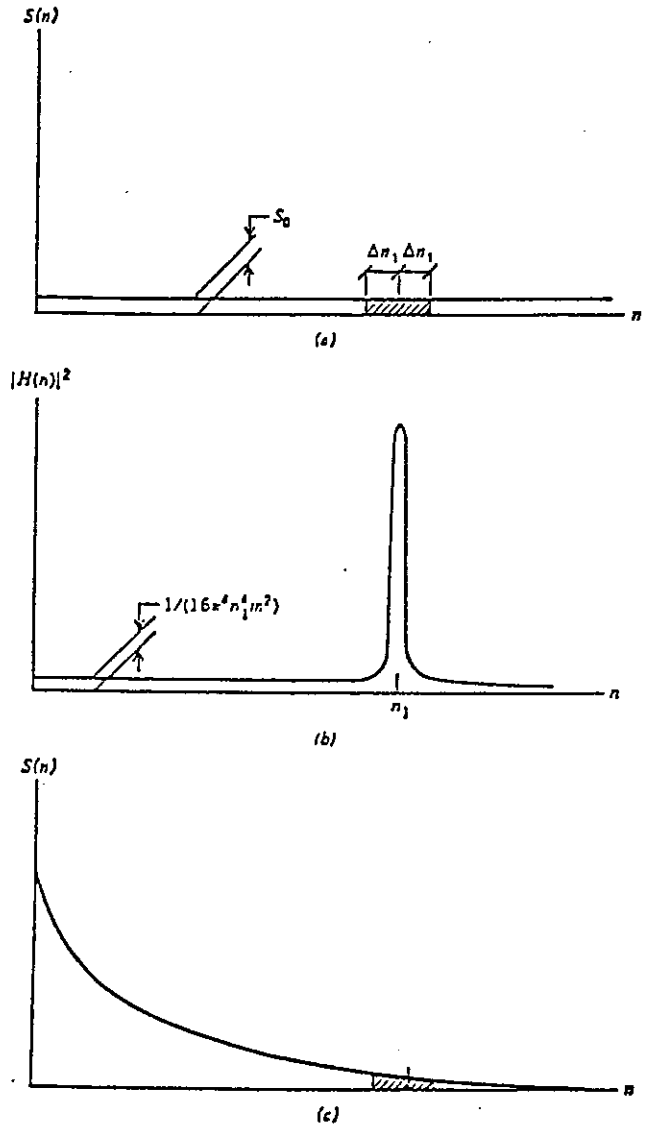

Fig. 2.4 : Decaying Spectrum for Real Winds [Simiu & Scanlan 86]

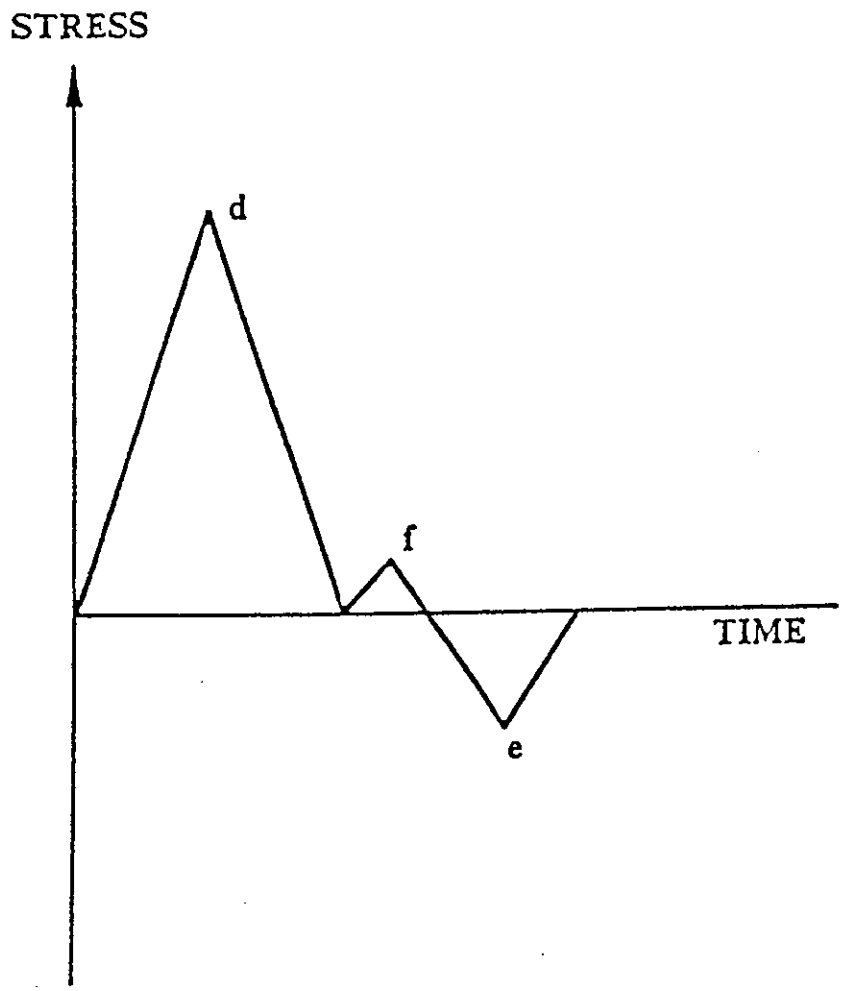

Fig. 2.5 : Normal Stress - Time Plot [Fisher at. el. 89]

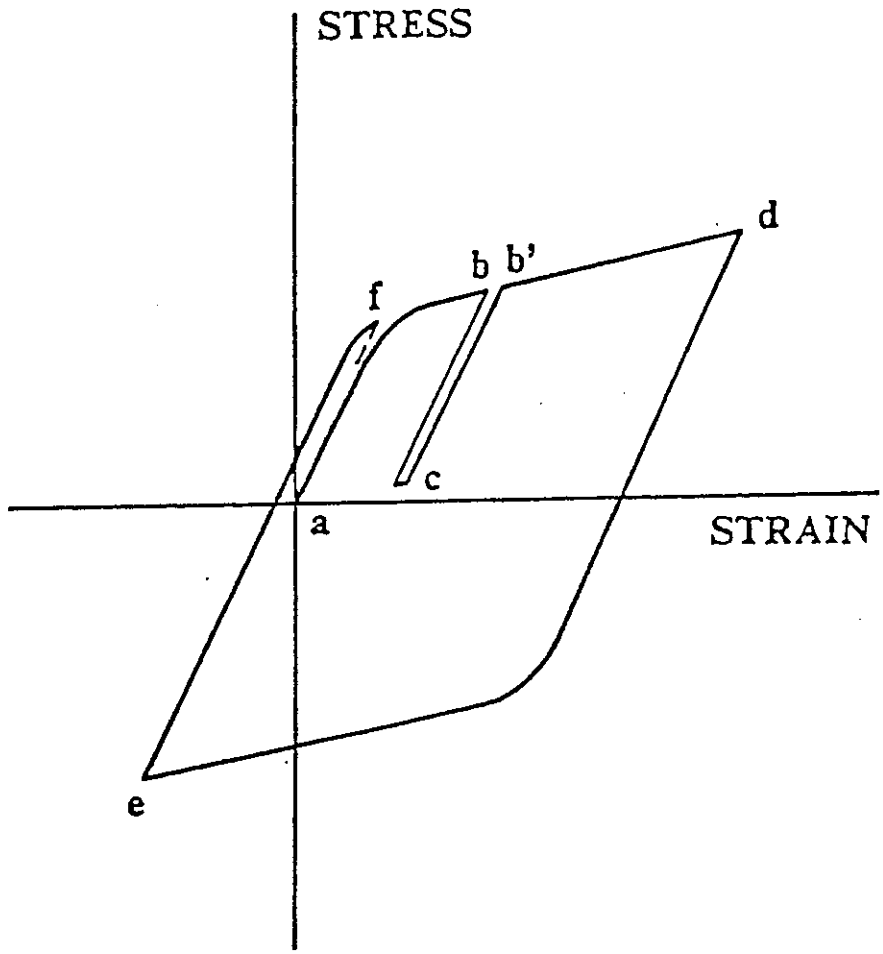

Fig. 2.6 : Stress - Strain Hysteresis at Crack Tip [Fisher at. el. 89]

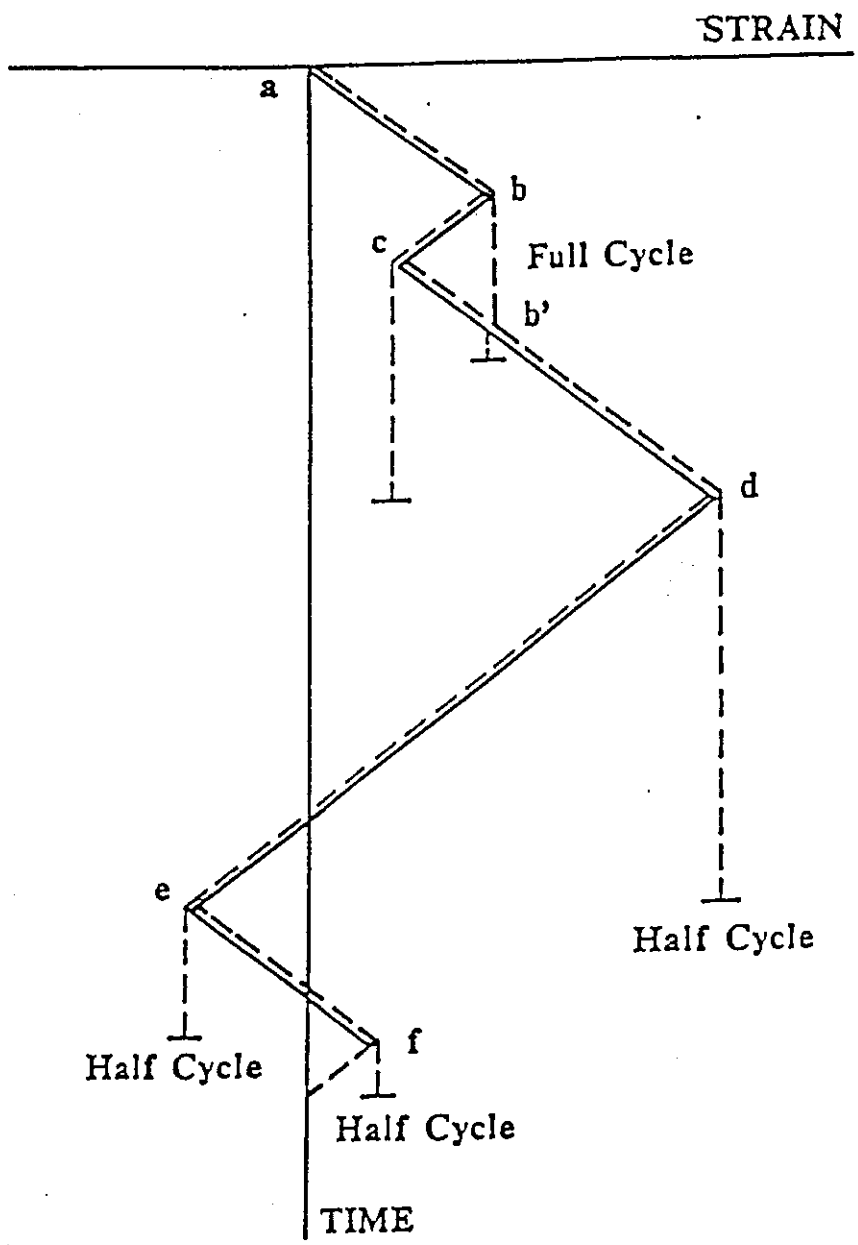

Fig. 2.7 : Rainflow Stress Range Cycle Counting Method

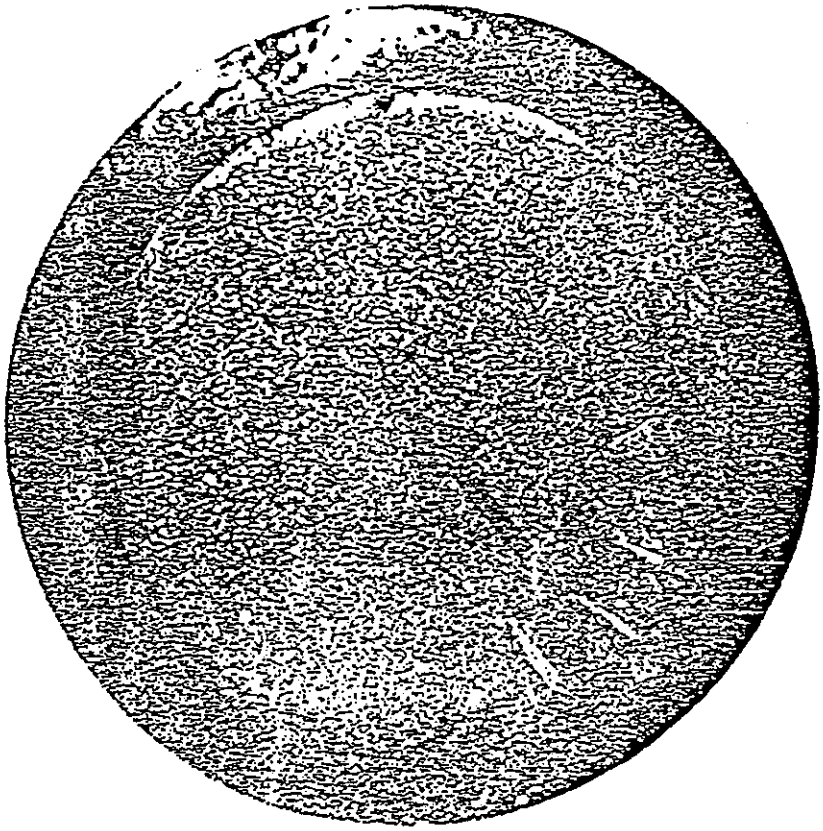

Fig. 2.8 : Straight Crack Front in Failed Bolt [James & Mills 88]

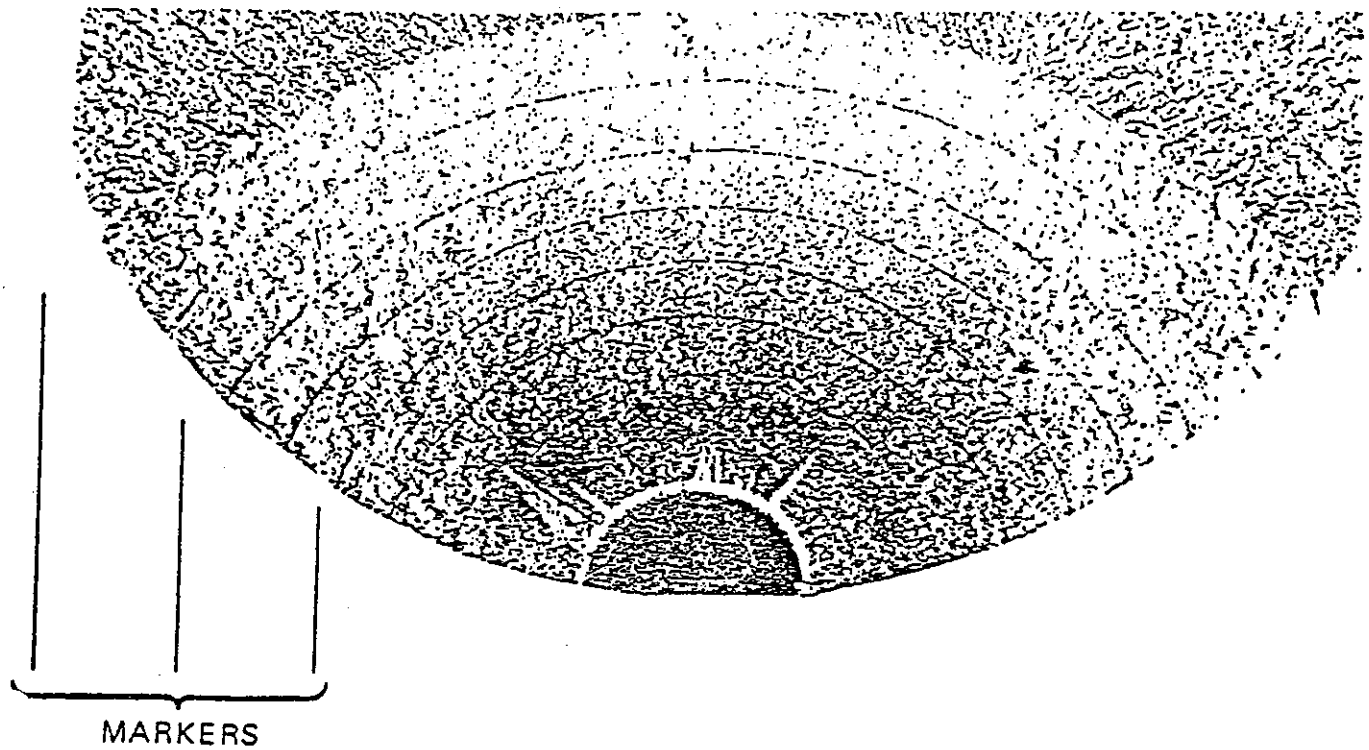

Fig. 2.9 : Semicircular Crack Front in Failed Bolt

[Mackay & Alperin 85]

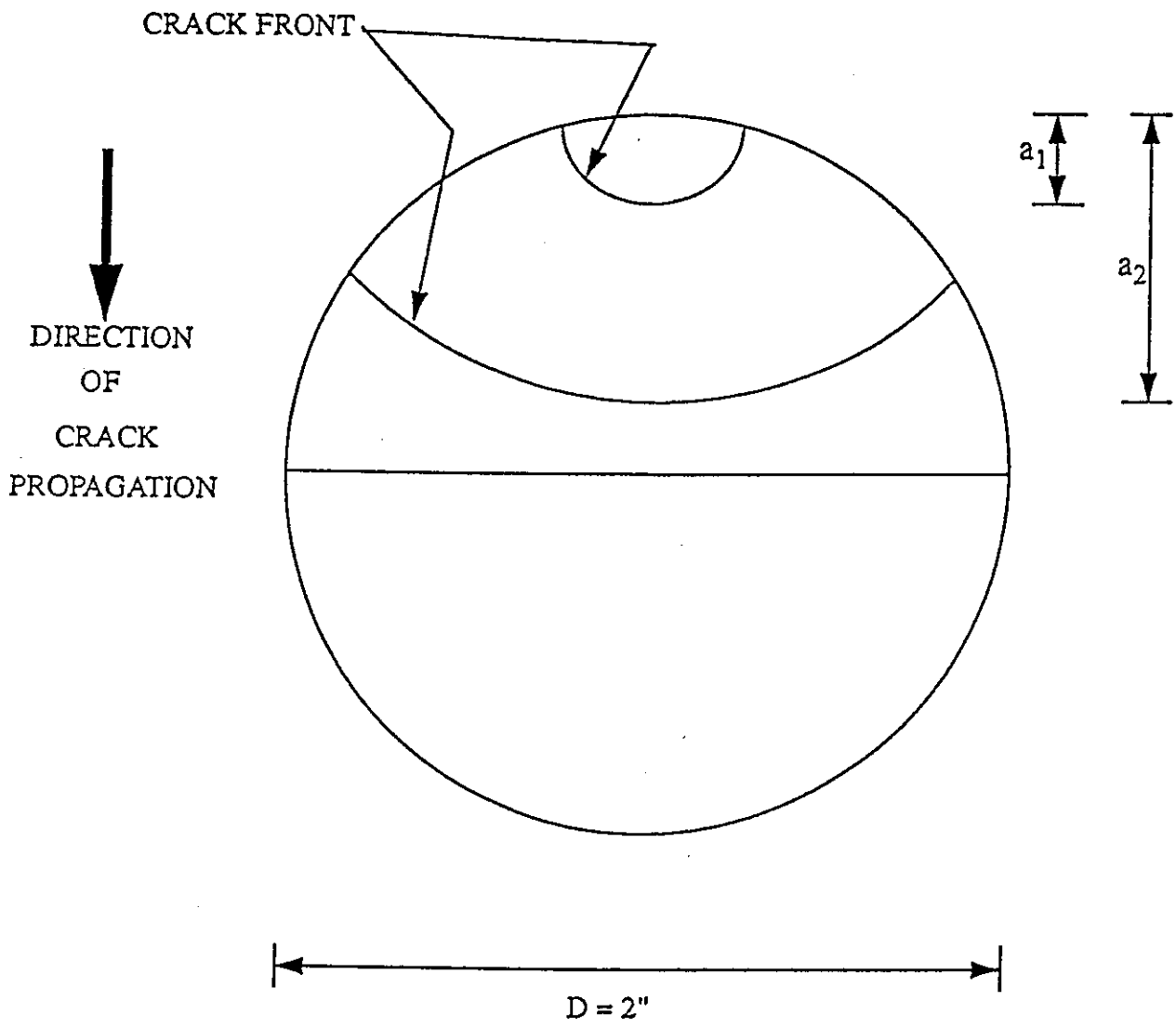

Fig. 2.10 : Assumed Propagation of Semicircular Crack Front

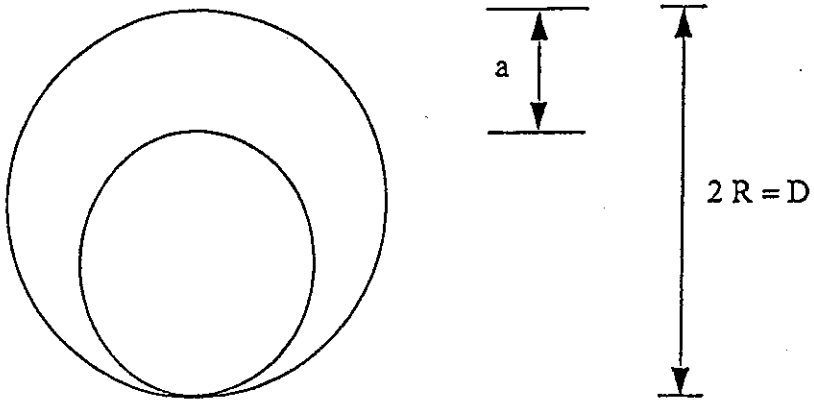

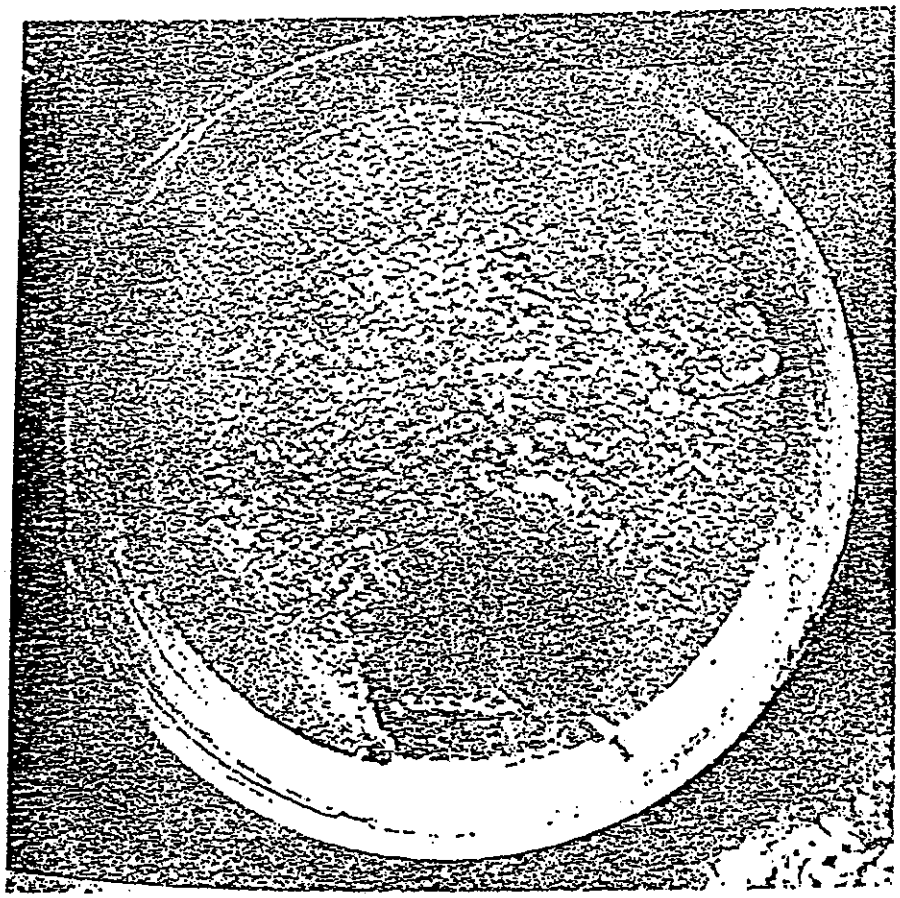

Fig. 2.11 : Sickle - Shaped Crack Front in Failed Bolt

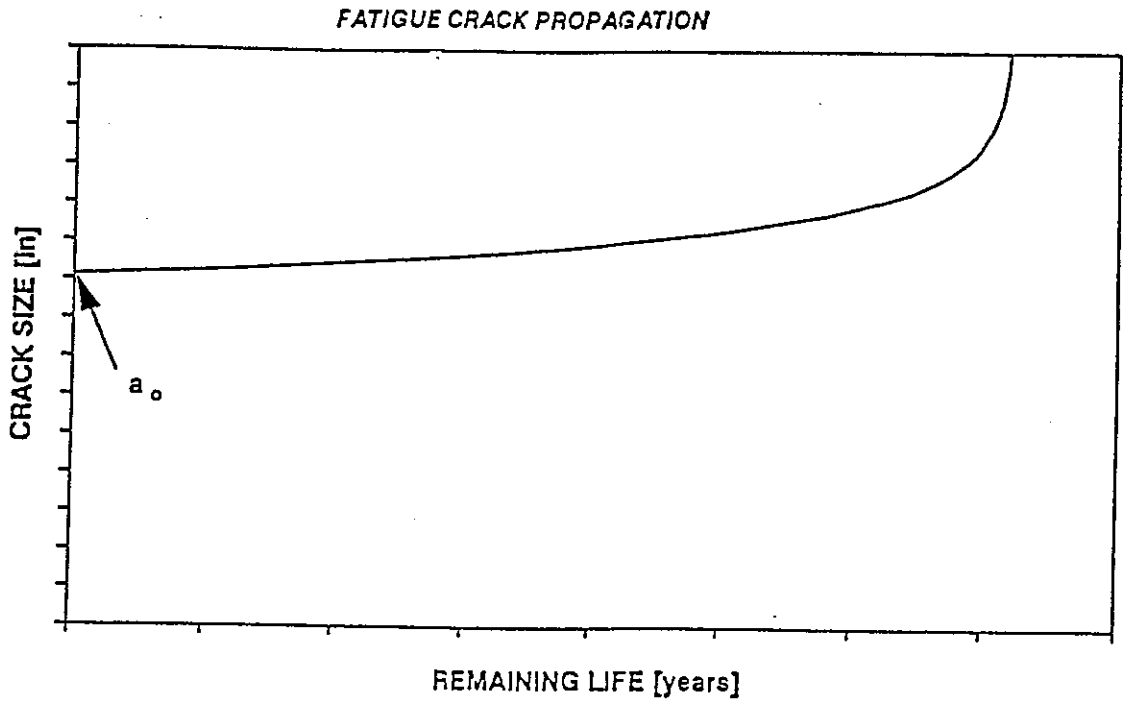

Fig. 2.12 : Fatigue Crack Propagation

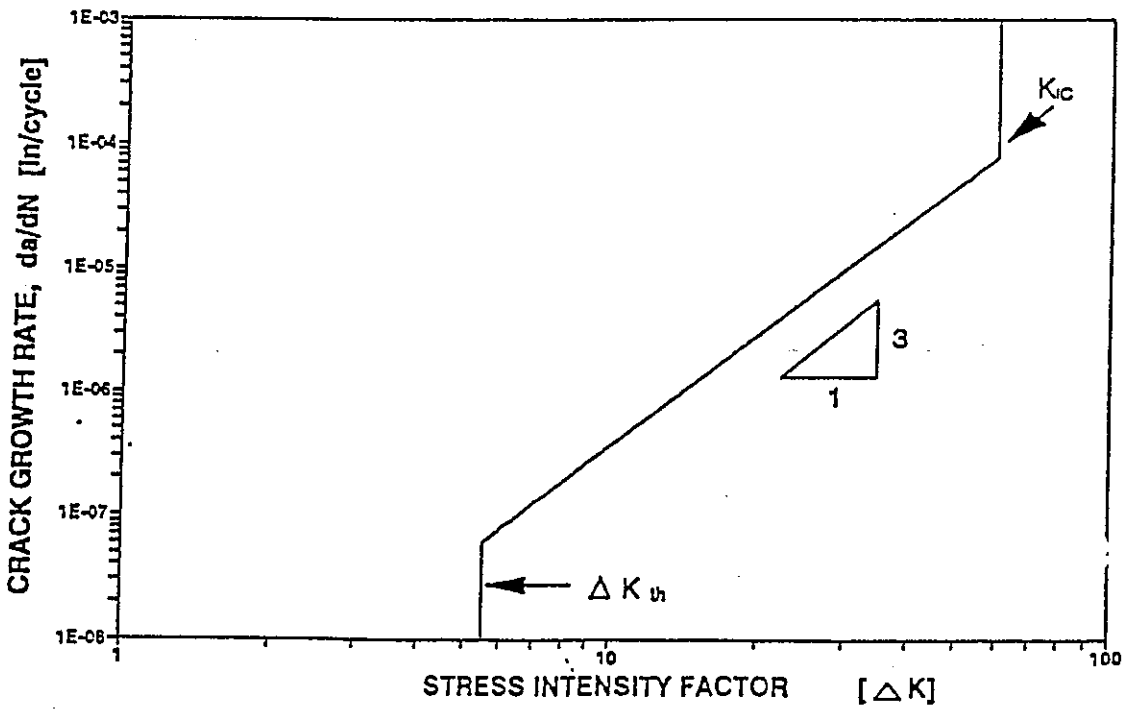

Fig. 2.13 : Fatigue Crack Growth Prediction

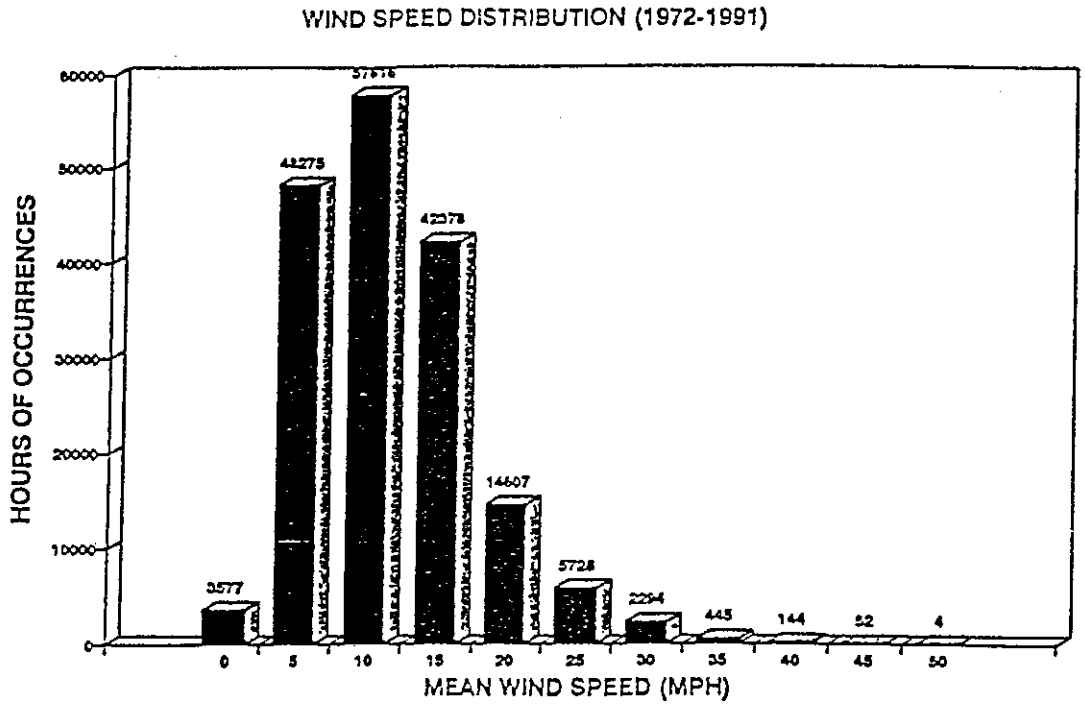

Fig. 2.14 : Histogram of Hourly Average Wind Speed Over 20 Years

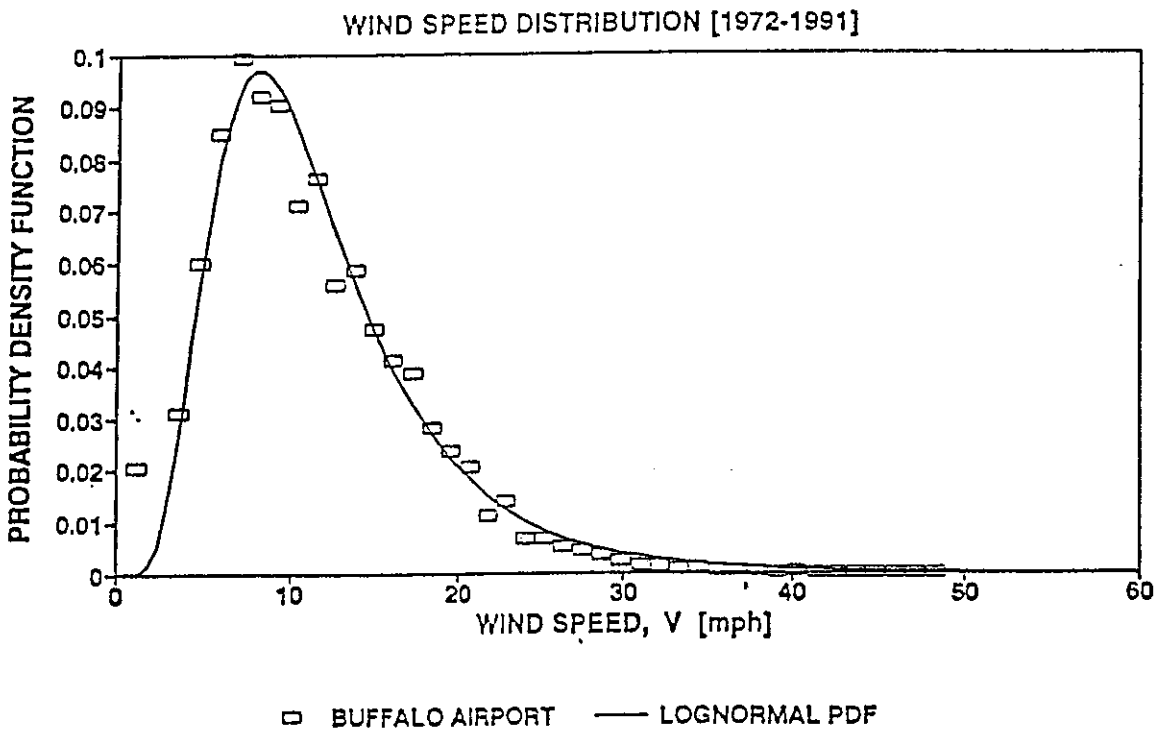

Fig. 2.15 : Probability Density Function of Hourly Average Wind Speed

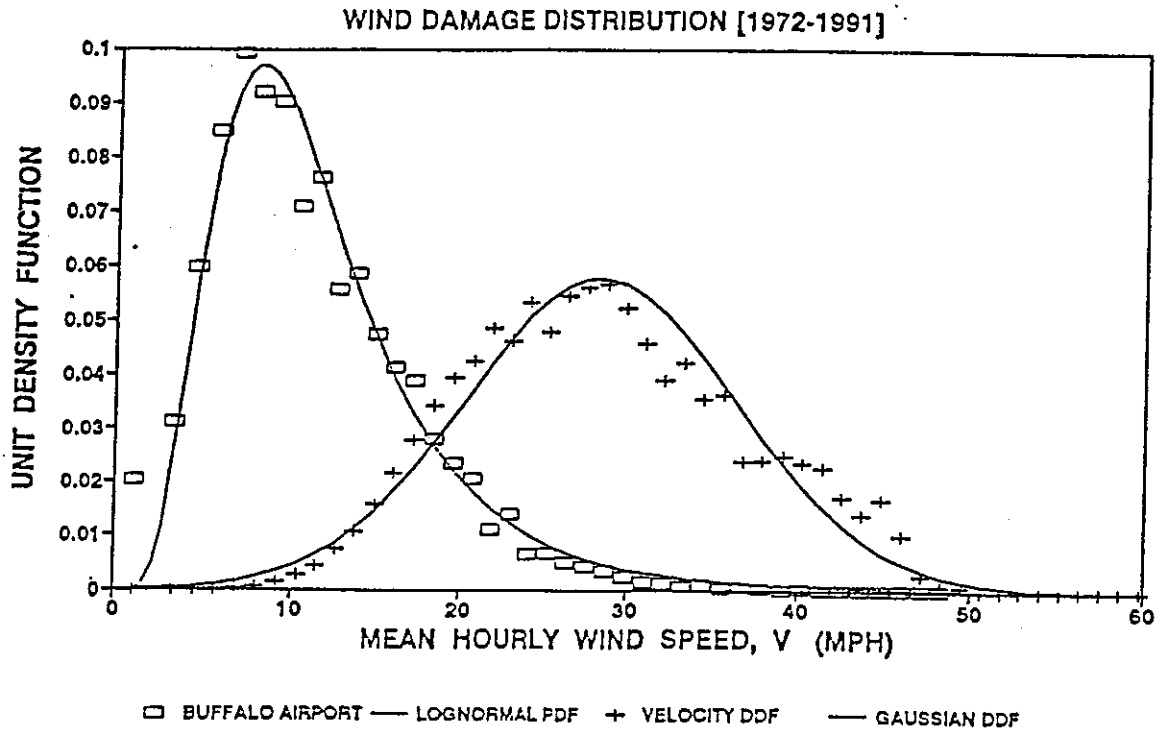

Fig. 2.16 : Damage Distribution Function of Hourly Average Wind Speed

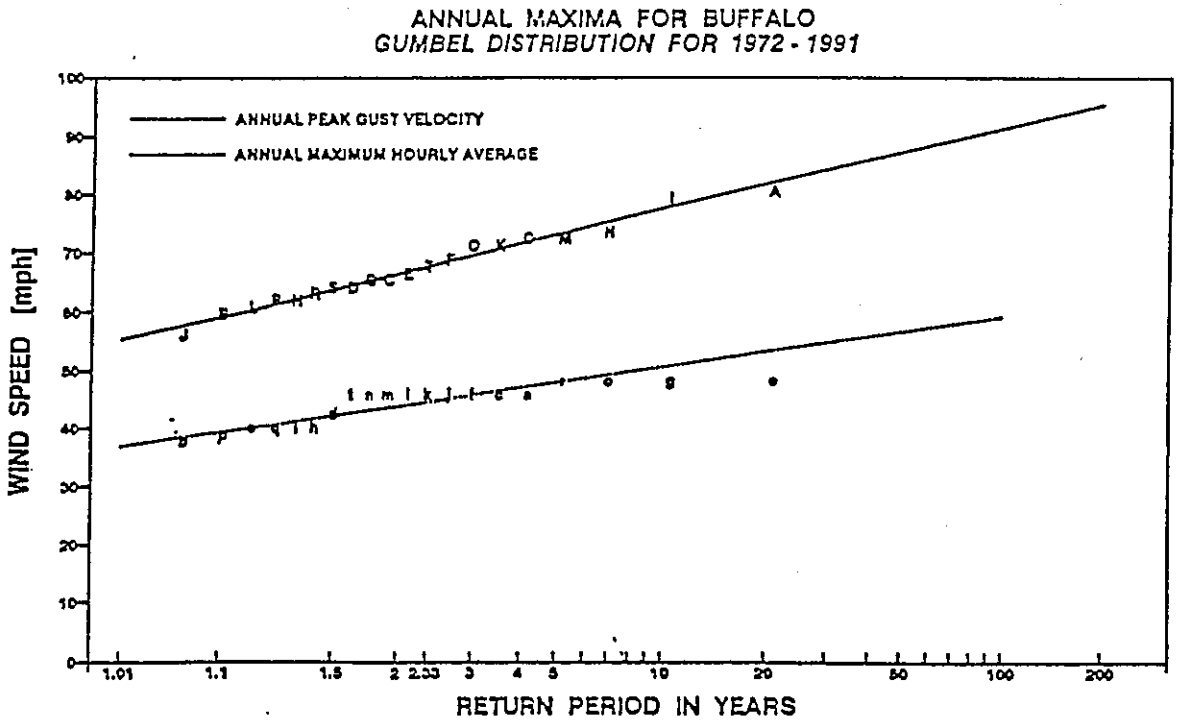

Fig. 2.17 Annual Peak Gust Speed Distribution Over 20 Years

SECTION 3
EXPERIMENTAL PROGRAM

3.1 INTRODUCTION

In order to ascertain the magnitude and nature of any fatigue damage to the anchor bolts, it was considered essential to directly measure the dynamic response of the pole with respect to the local wind environment and to relate this response to the cyclic strain induced fatigue and/or fracture damage. This section thus describes the instrumentation employed for the field study which was carried out over a six month period from November 1991 to May 1992.

The middle west light pole at the stadium was selected for the pole base integrity instrumentation. This instrumented light pole is located next to the press box of the stadium and is illustrated in Fig. 3.1. The elevations of this light pole in the strong and weak axis direction are shown in Fig. 1.2.

3.2 INSTRUMENTATION

3.2.1 General

The instrumentation was installed in three main phases. Firstly, five accelerometers were mounted on the pole in July 1991 and were connected to a computerized data acquisition system in order to determine the dynamic characteristics of the light pole under the naturally occurring wind conditions. Secondly, in early November 1991 strain gauges were mounted on the light pole near the pole base to measure reaction forces to the wind loading. Strain gauges were also mounted on three of the 16 holding-down bolts for determination of the stresses in the holding-down bolts. Thirdly, acoustic emission equipment was installed on the three bolts in an attempt to monitor fatigue crack propagation and to quantify the progression of the crack front, if any.

The cables from the four types of instrumentation were assembled and fed through an underground conduit to reach the data acquisition system. A 486 IBM PC based 16 channel computerized data acquisition system was used for condition monitoring of the light pole. This was located inside the telephone room adjacent the press box as shown in Fig. 3.2. Fig. 3.3 shows a schematic diagram of the data acquisition setup.

Further details of the instrumentation systems are described in the following subsections.

3.2.2 Wind Speed

A model 05103 Young anemometer is used to measure wind speed and direction. The instrument is mounted on a redundant antenna mast adjacent to the pole, as shown in Fig. 3.4 and 3.5. Wind speed and direction signals are transmitted on channels 1 and 2, respectively.

3.2.3 Pole Dynamic Response

Five accelerometers, type 302A from PCB Piezotronics were installed on the pole at two levels as shown in Fig. 3.4. At the upper level (at 151 ft. above the ground level), two

accelerometers (channels 3 and 5) were placed at the extremities of the middle level of light baskets oriented along the Y-Y meridian to capture both strong axis bending (translational) motion by averaging the signal. Differences in this pair of signals indicate any possible torsional nodes. The third accelerometer at the upper level (channel 4) was oriented along the X-X meridian to capture weak axis bending motion.

Two accelerometers were placed at 95.5 ft. above ground level to indicate whether higher mode response was significant. Channels 6 and 7 were used for the Y-Y and X-X bending, respectively. Analog voltage signals from the accelerometers are firstly processed through signal conditioners, secondly routing through an A/D converter, and then stored in the 486 computer.

3.2.4 Pole Base Moments and Shears

The strain gauges were wired to form a full bridge temperature compensated circuit for the determination of pole reaction forces to wind loads. By determining the pole base bending moments and shear forces, it is possible to determine theoretical anchor bolt stresses. For this purpose, strain gauges and rosettes are used near the base of the pole.

Bending moments are measured at two levels, 4 and 12 ft. above the base plate. Assuming a linear bending moment diagram near the base of the pole, the moment at the base can be found from extrapolation, thus

$$M_{base} = 1.5\,M_4 - 0.5\,M_{12} \tag{68}$$

where M_4 = moment measured at 4 ft. above the base, and M_{12} = moment measured at 12 ft. above the base.

By differentiating the moment gradient, the shear force can be determined. Thus bending moments in the x and y directions are calculated from curvatures determined from strain differentials as follows:

$$\frac{M_i}{EI_i} = \phi_i = \frac{\Delta e_i}{d_i} \tag{69}$$

where EI_i = flexural bending stiffness, d_i = over distance between strain gauge pairs, and Δe_i is the differential strain measured in a full bridge circuit for the i^{th} channel.

The four strain gauge channels shown in Fig. 3.4 for pole moments are thus related by the following matrix

$$\begin{Bmatrix} M_4^x \\ M_4^y \\ M_{12}^x \\ M_{12}^y \end{Bmatrix} = \begin{bmatrix} EI_x/D & & & \\ & EI_y/B & & \\ & & EI_x/D & \\ & & & EI_y/B \end{bmatrix} \begin{Bmatrix} \Delta e_8 \\ \Delta e_{10} \\ \Delta e_9 \\ \Delta e_{11} \end{Bmatrix} \tag{70}$$

where I_x and I_y are the second moment of area for the respective strong and weak bending axes, with the corresponding depth and breadth of the section, D and B. In a similar manner, channels 15 and 16 are used to determine pole torsion.

3.2.5 Anchor Bolt Strains

Channels 12, 13 and 14 record axial strains in Bolts 1, 2 and 3 shown in Fig. 3.6. Bolt stress is determined by multiplying a dynamic value of Young's modulus taken herein as E = 30,000 *ksi*, thus

$$\sigma_i = E\epsilon_i \tag{71}$$

These particular bolts were chosen since Bolt 1 had previously been identified as having a large ultrasonic indication, Bolt 2 a small indication and Bolt 3 had none, as shown in Fig. 3.7.

The strain gauges were wired in a quarter bridge. Mounting dummy gauges for full bridge (temperature compensated) wiring was not possible due to the space limitations on the anchor bolts. Therefore, some drift of the signal is to be expected. However, for the purpose of measuring stress range histories over five minute periods, such drift was considered not to be a significant problem.

3.3 AN OVERVIEW OF ACOUSTIC EMISSION NON-DESTRUCTIVE TESTING

3.3.1 Acoustic Emission Monitoring

Acoustic emission monitoring devices are used on the same three strain gauged bolts to provide an independent check of the previous ultrasonic testing results and to correlate with measured bolt stress ranges to estimate the remaining fatigue life of the bolts. These devices, supplied by the MONAC International Inc., use transducers mounted on the top of the three bolts to detect sound bursts emitted by propagating cracks. Fig. 3.8 illustrates the transducer mounting. The acoustic emission system employed in this study is described in more detail in the following subsection.

3.3.2 The General Approach

The MONAC acoustic monitoring system is designed to determine fatigue crack initiation and growth in structural members and components by monitoring acoustic emissions during cyclic loading. The purpose of the acoustic emission monitoring was to determine if suspected fatigue cracks in the anchor assembly were active and how rapidly they were propagating. The results can be used to help quantify the effects of bolt cracking by providing estimates of parameters in fracture mechanics models used to calculate crack growth rates and remaining life in terms of changes to the stress intensity factor as described in Section 4 of this report.

In general, an acoustic emission nondestructive monitoring system consists of the following components as shown in Fig. 3.9: transducer(s), pre-amplifier and filter, signal processor, and digital computer, all connected by appropriate cables. The transducer itself is a pressure sensor, typically of the piezoelectric type. It responds to strain by producing a voltage output. Growing cracks release strain energy in the form of pressure pulses which are detected by these transducers. A signal that results from any of the above mechanisms is defined as an "event" if the amplitude rises above a certain voltage threshold and if the signal meets other criteria. Typical amplified acoustic emission signals are shown in Fig. 3.10. The other criteria are typically frequency, event duration (in milliseconds), rise-time,

number of counts, and energy, refer to Fig. 3.11. The number of counts is equal to the number of pressure fluctuations above the pre-selected threshold value during the event. The pre-amp gain boosts the transducer's output electric signal, which is typically very small initially (e.g., fractions of millivolts). The resulting amplified signal may contain frequencies outside the range of interest and thus, is then filtered such that only the frequencies of interest are passed on. The signal processor extracts time domain data relating to the number of signals received, how fast they are received, how strong they are, and how long they last. Results are stored on the hard disk of the microcomputer dedicated to this purpose. A schematic view of the MONAC system setup is shown in Fig. 3.12.

At the Rich Stadium site, the narrow band (100 kHz - 500 kHz) transducers are mounted in housings which are magnetically attached to the tops of the bolts, as shown in Fig. 3.8. A spring inside the housing keeps a light pressure on the transducer to keep it down against the bolt itself. Proper acoustic coupling is ensured by a thin silicon grease film between the transducers and the top of the bolt. The pre-amps are located underneath the pole base plate. This allows for minimum cable length between the transducer and the pre-amp, and it allows the pre-amps to be out of the way of curious lookers. (A longer cable would also introduce a higher impedance and noise.) The three cables are routed underground along the conduit (Fig. 3.2) into the telephone network room, where they are connected through three signal conditioners to a separate 386 PC computer used for the acoustic emission data logging.

3.3.3 Acoustic Emission Correlation to Stress Intensity Factor Range

The purpose of the acoustic emission monitoring of the 3 bolts is to determine if suspected fatigue cracks in the anchor assembly were active and how rapidly they are propagating. In utilizing this technique, the structural component is passively monitored for elastic pressure wave pulses that arrive at surface locations where acoustic transducers are placed. These pulses contain information on damage or fracture events that occur on the surface, or from cracks embedded within the bulk of the material. Through comparison of

a time signal with a past history of time responses, insight can be gained regarding the compounding damage in the structure.

Like other nondestructive testing techniques, acoustic emission requires skilled personnel and knowledgeable interpretation of results. A number of practical difficulties make it, like other nondestructive testing techniques, less than an exact science. For example, detection of acoustic emission signals is hindered by background noise. This noise may be of mechanical or electrical origin, and it may be very broad-band in nature. Through careful amplifier gain, filtering and appropriate threshold settings, the desired signals may still be generated. Fig. 3.12 shows a schematic diagram of the AE system supplied for this study by MONAC International, Inc.

Another potential complication is that events from a number of sources may occur simultaneously. These may constructively or destructively interfere with each other at the system sensor. Trained personnel are required to distinguish between normal and anomalous signals.

Finally, the form of the elastic wave reaching the sensor may be completely different in nature (shape) than that generated at the source of the emission. This is due to signal modification when the wave encounters a boundary discontinuity or free surface. Different materials have different wave propagation speeds associated with them as well. This tends to separate frequency components as the wave travels over long distances. Surface (Rayleigh) waves also travel at different velocities than waves within the bulk of the material. Regardless of these vagaries, it is normally assumed that the signals emitted from a flaw are all modified in a proportionate (i.e., like) manner. Thus, even though the signal is not an exact replica of the crack event, comparisons can legitimately be made between arriving signals, as long as the transducer positioning is not altered.

For the purposes of the present study, the following is of particular interest: since both crack growth rate and emission count rate increase with a worsening severity of flaw,

a direct proportionality exists between the actual number of counts and the crack area created in a specific time interval. The MONAC data analysis is based on the theoretical relationship that exists between fatigue crack growth rate and acoustic emission activity as measured by a count or event rate. In experimental fracture mechanics, this relationship is usually represented by expressing the acoustic emission count rate as a function of the stress intensity factor range ΔK, as shown in Fig. 3.13. The relationship employed has the form of a power law,

$$AE_{count\ rate} = C'(\Delta K)^6 \tag{72}$$

where the constant C' = a function of standard specimen thickness and material properties and crack geometry, as well as experimental gain and threshold levels.

3.3.4 Acoustic Emission Crack Monitoring

As mentioned, Fig. 3.13 illustrates the relationship among acoustic emission count rate, crack growth rate, and the stress intensity factor for two steels. Experimental fracture-acoustic emission data for the particular steel used in these anchor bolts are not available, so experimental data for 1% carbon steel was used to estimate the stress intensity factor range. Since the acoustic characteristics for most carbon steels are similar, the possible error resulting from the use of this data is considered to be minimal. It should be further noted, however, that the data for Fig. 3.13 are from tests performed for an edge crack on a 0.75 in. thick plate specimen, while the anchor bolts are 2 in. in diameter at the root of the threads. When the specimen thickness changes, acoustic count rate changes accordingly. The correction factor needed to account for this difference depends on the geometry of the crack front, which is not known. Thus, as previously described, three different crack front geometries were assumed and investigated based on actual fatigue cracking scenarios which have been reported for bolts: an edge crack with a semi-circular to straight crack front [James and Mills 88], a sickle-shaped crack [Mattheck 85], and an annular crack [Hertzberg 89]. More accurate estimates would be achieved if laboratory fatigue test results could be

obtained on the actual anchor bolt material and if actual crack shape were known.

The procedure employed to estimate ΔK and a_0 is as follows:

1. Assume a flaw size a.

2. Calculate K for the standard plate specimen from

$$K = f(\alpha)\,\sigma\sqrt{\pi a}$$

where

$$f(\alpha) = 1.12 - 0.231\,\alpha + 10.55\,\alpha^2 - 21.72\,\alpha^3 + 30.39\,\alpha^4 \qquad (74)$$

which is valid for $0.1 \le \alpha \le 0.7$, where $\alpha = a/W$, where W is the width, taken to be 2".

3. Assume shape for the crack in the bolt.

4. For this crack with size as assumed in step 1, determine: length of crack front, b, and stress intensity correction factor Y.

5. Calculate the ratio of the crack front length to the width of the standard specimen used to generate the correlation used in Fig. 3.13.

$$r = b \,/\, 0.75 \qquad (75)$$

6. Calculate the adjusted AE count rate:

$$(C.\,R.)_{adj} = (C.\,R.)_{actual} \,/\, r \qquad (76)$$

7. From Fig. 3.13, determine the equivalent stress intensity factor range that would exist in the standard specimen, $(\Delta K)_{eq}$.

8. Adjust for the stress intensity correction factor Y:

$$(\Delta K)_{expt} = Y\frac{(\Delta K)_{eq}}{f(\alpha)} \tag{77}$$

9. For measured stress ranges, use the analytical expression for ΔK to solve for the initial (current) flaw size:

$$\Delta K = Y(\Delta \sigma)_{avg}\sqrt{\pi a_o} = (\Delta K)_{expt} \tag{78}$$

10. Compare to crack size assumed in step 1. Reiterate the procedure, if necessary.

Once a_0 is available, determination of remaining fatigue life can be performed. Results of such estimates of remaining fatigue life are presented in Section 4.

3.4 DATA ACQUISITION AND PROCESSING

Wind speed was monitored continuously at a sampling rate of 1 Hz. For each hour all channels are monitored. The collected data was stored on the hard disk of the 486 computer. Approximately twice weekly, the data was archived onto diskettes for further analysis. Three additional channels of acoustic emission signals were collected on a separate 386 computer.

Acoustic Emission

The three acoustic emission data channels collect data continuously, activated whenever detectable acoustic emission activity occurred in any of the three instrumented bolts.

Other Channels

The other 16 channels start collecting data in the beginning of a one-hour period of time at a sampling rate of 20 Hz for five minutes. In order not to overwhelm hard disk storage capacity, for the remaining 55 minutes of each hour, only the wind speed and wind direction are collected continuously at a sampling rate of 1 Hz. This data acquisition system was operated continuously 24 hours a day, except whenever interruptions occurred for data downloading, system maintenance, and power failures.

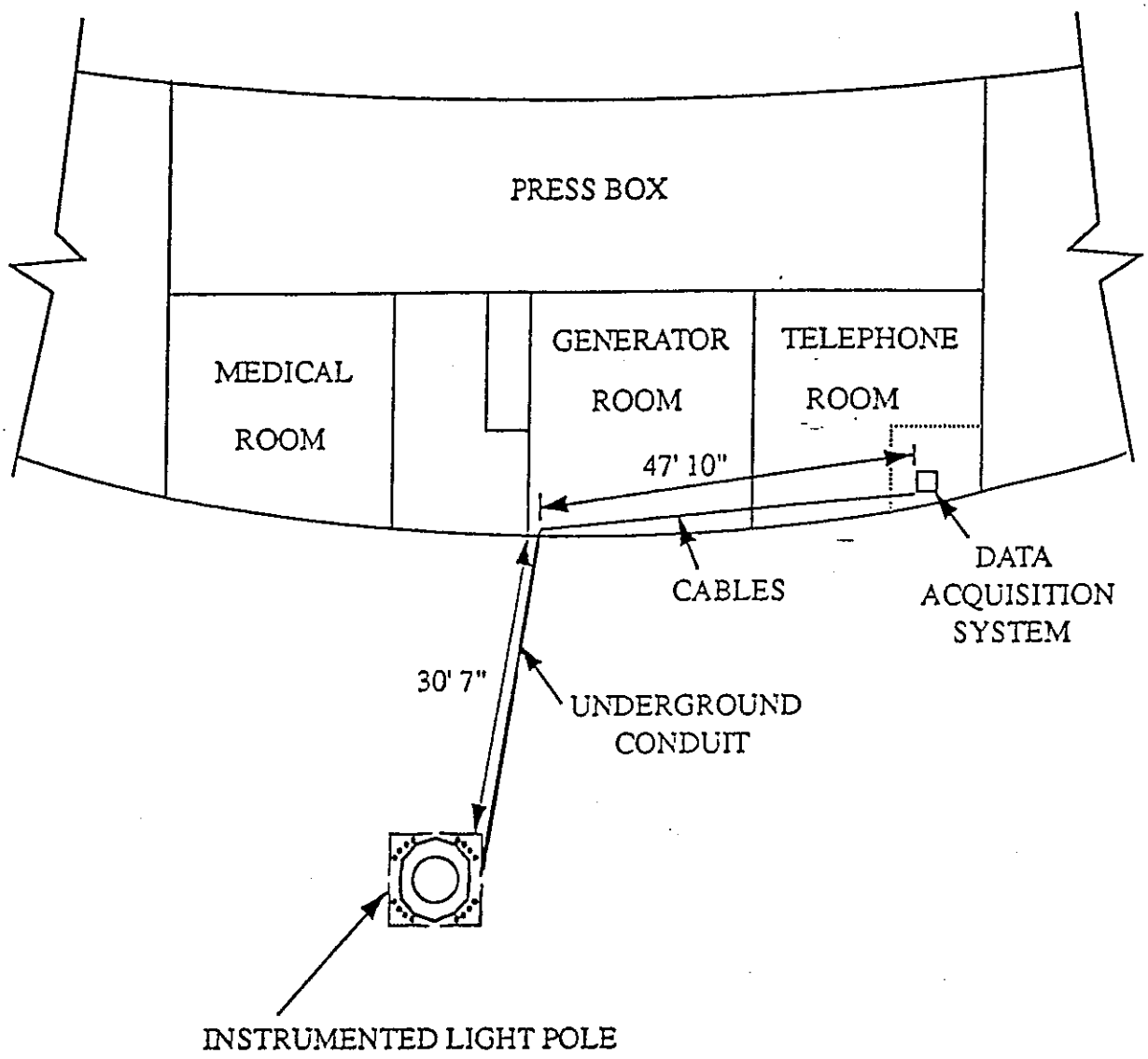

Fig. 3.2 : Location of the Data Acquisition System

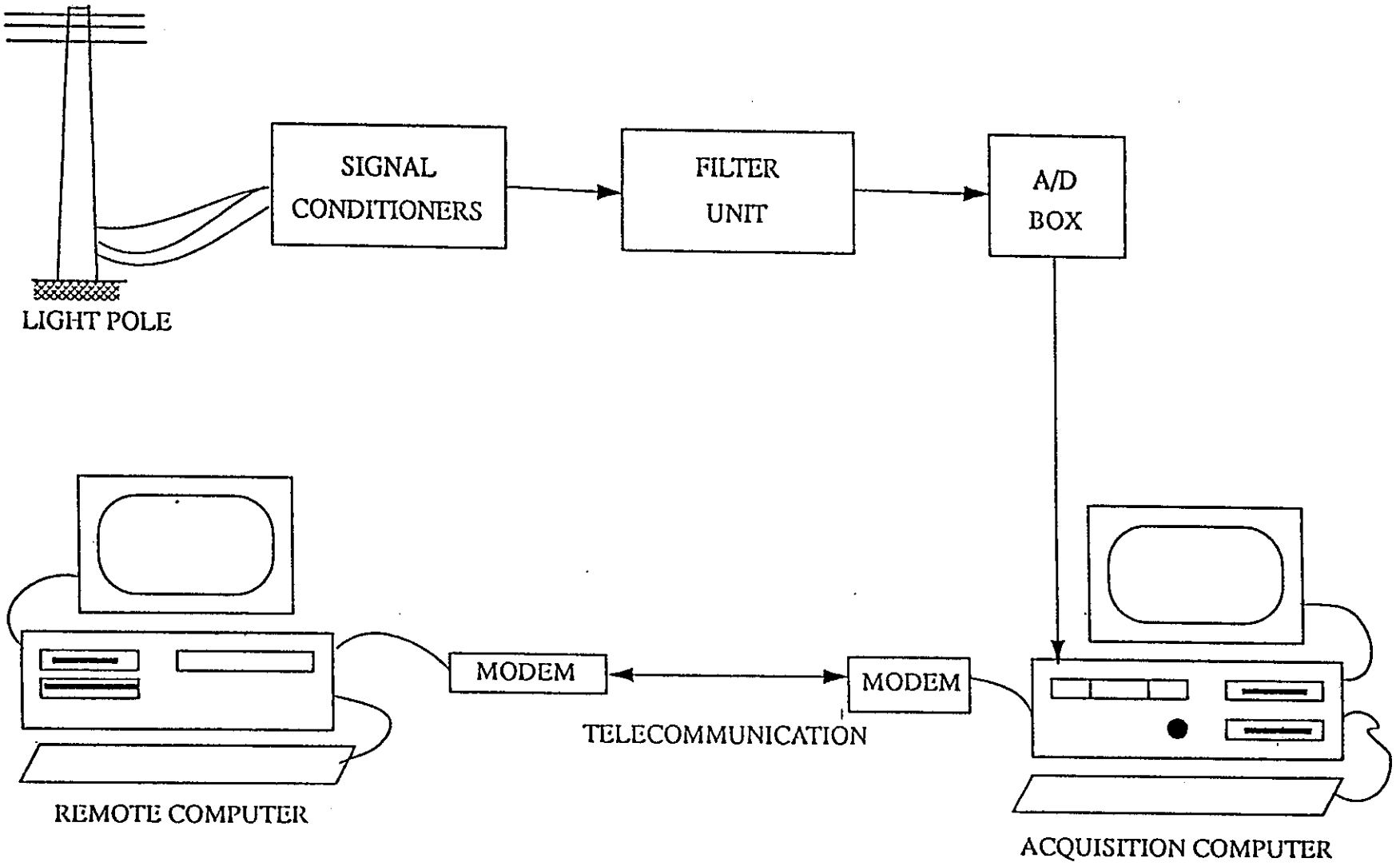

Fig. 3.3 : Schematic Diagram of Data Acquisition System

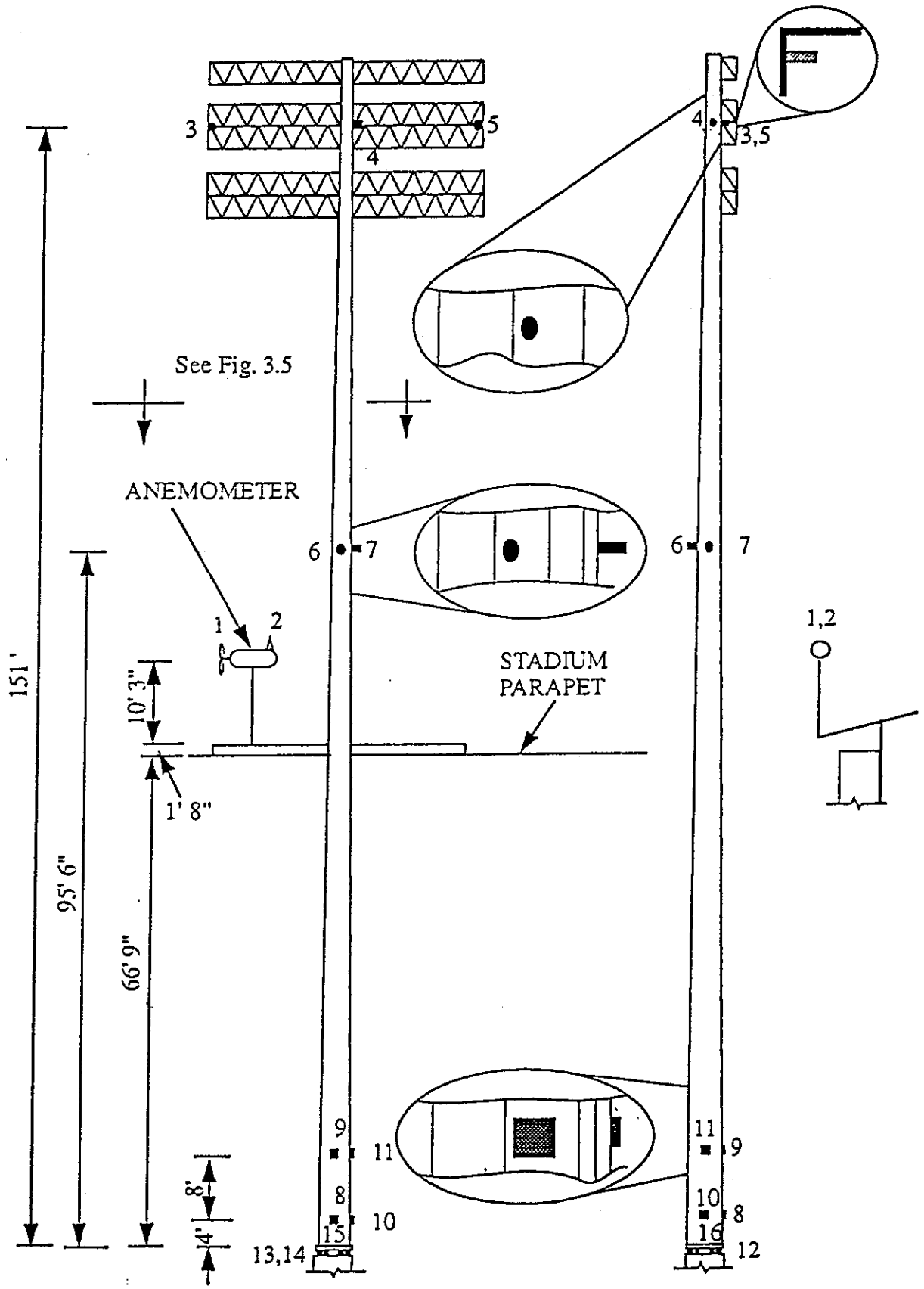

Fig. 3.4 : Instrumentation of the Light Pole

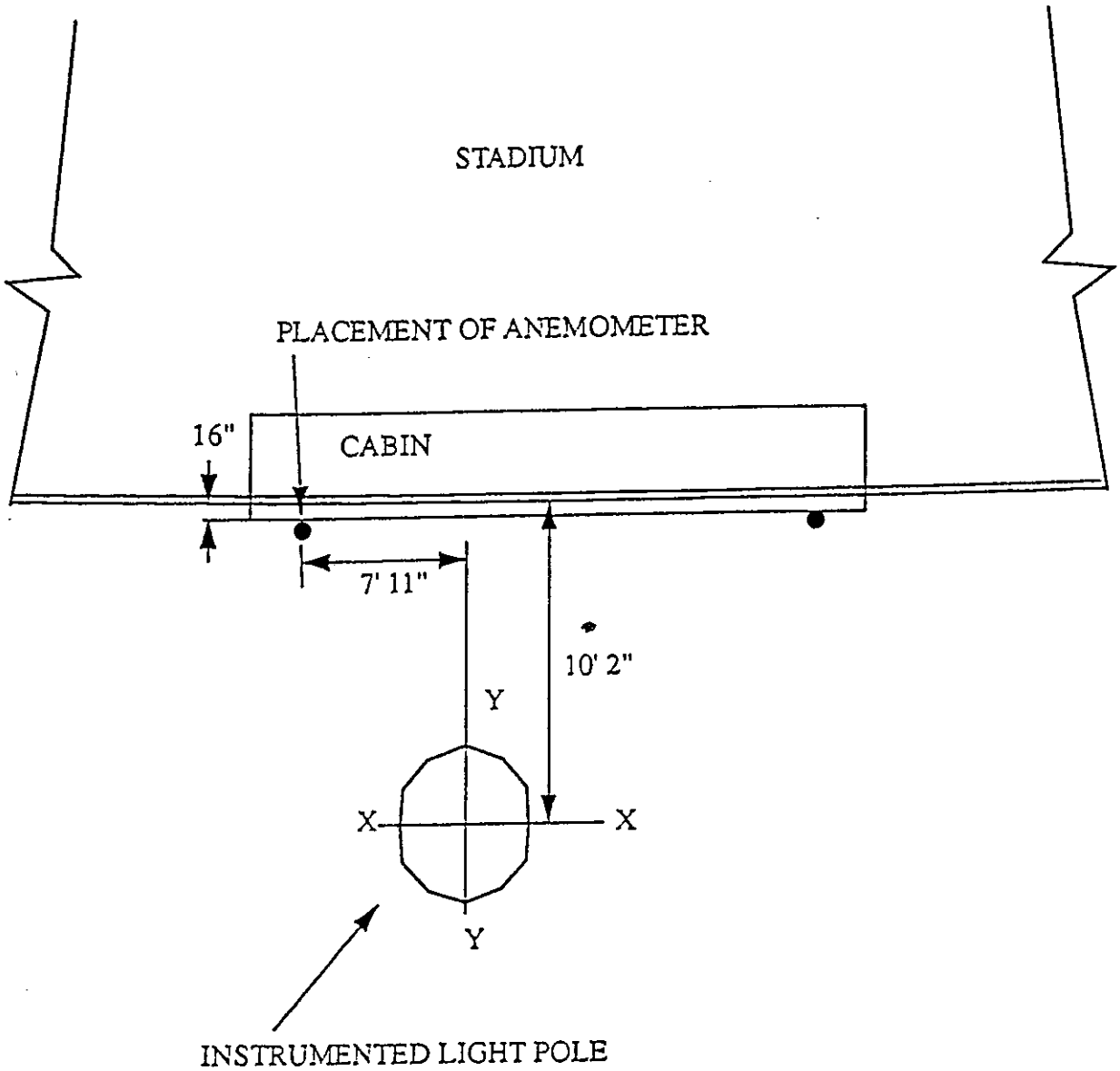

Fig. 3.5 : Plan View of Anemometer Location

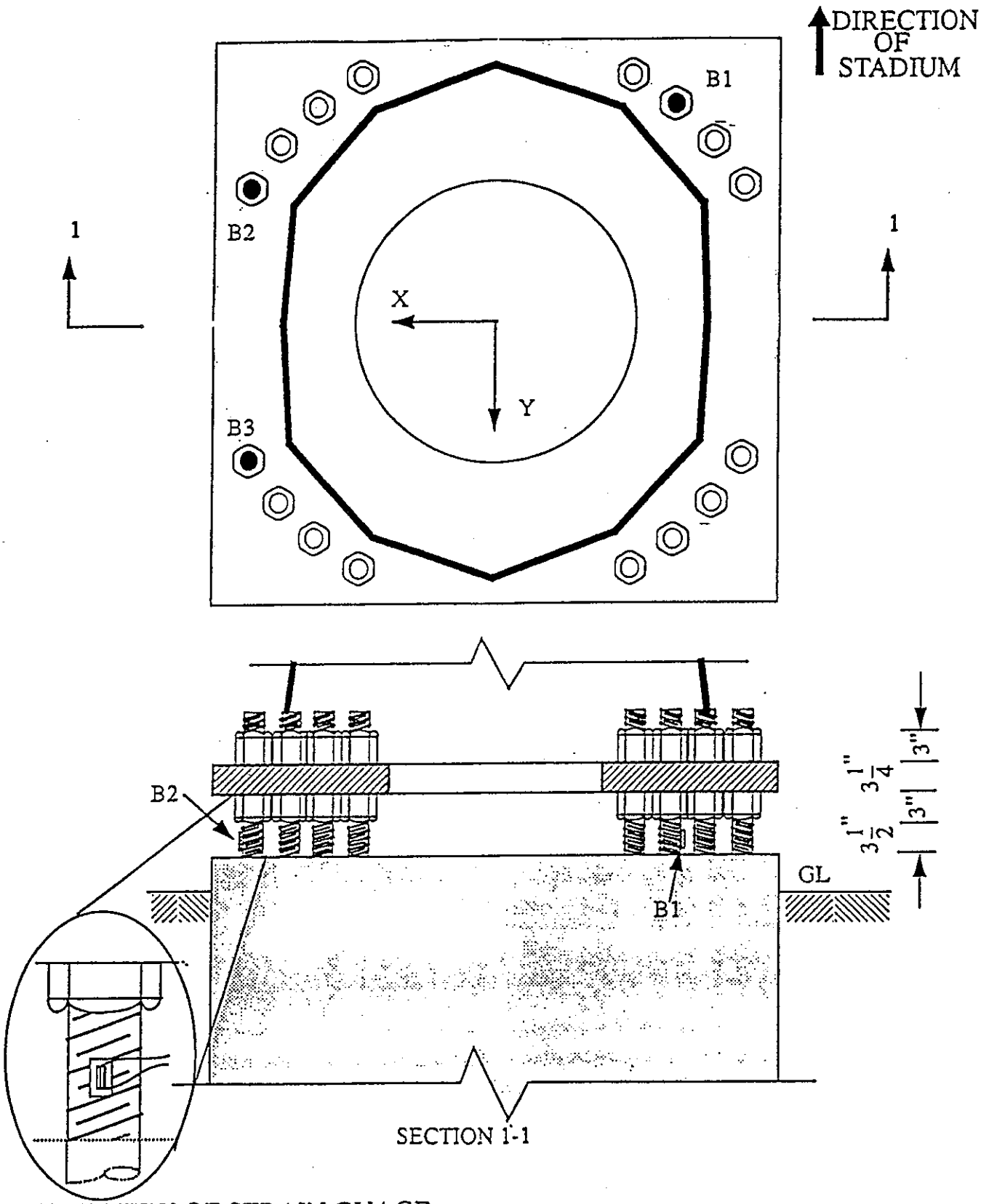

Fig. 3.6 : Strain Guages and Instrumentation of Bolts

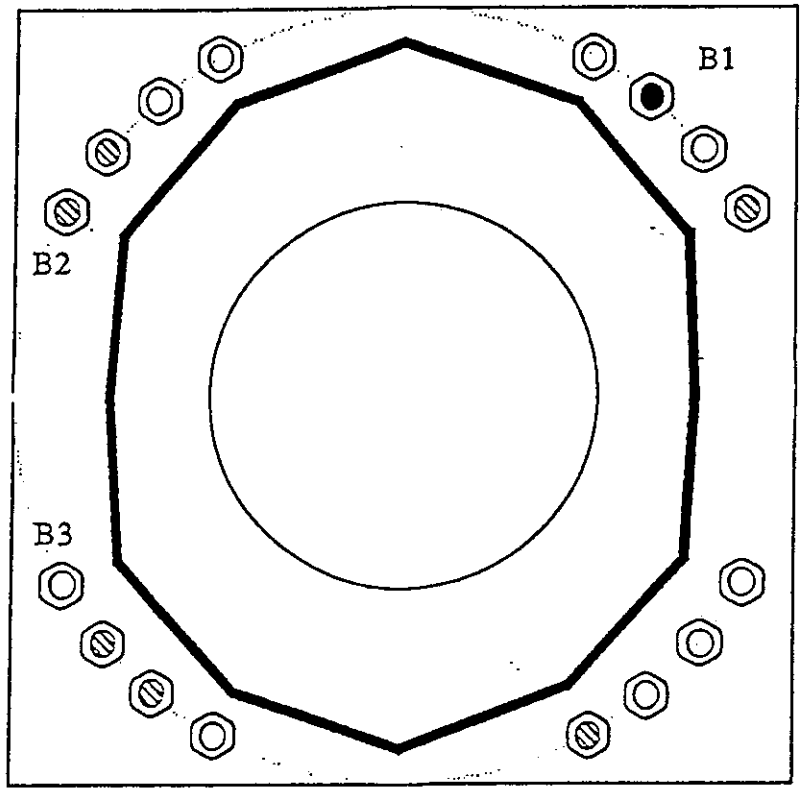

● ULTRASONIC LARGE INDICATION

⊘ ULTRASONIC INDICATION

Fig. 3.7 : Anchor Bolt Ultrasonic Test Indications
(From Meyer Industries Sketch Dated 8 - 23 - 90)

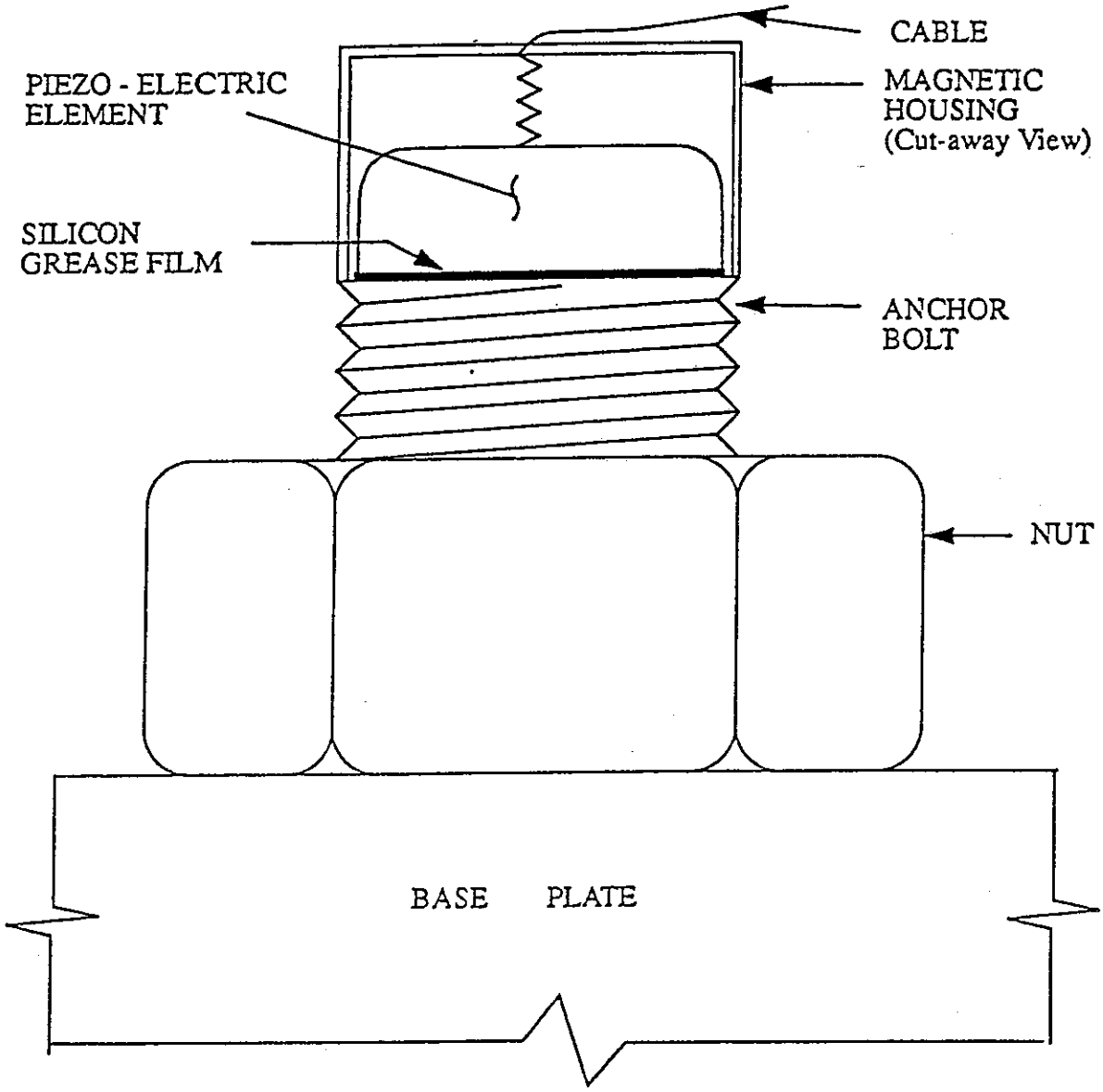

Fig. 3.8 : Transducer Mounting on Anchor Bolt

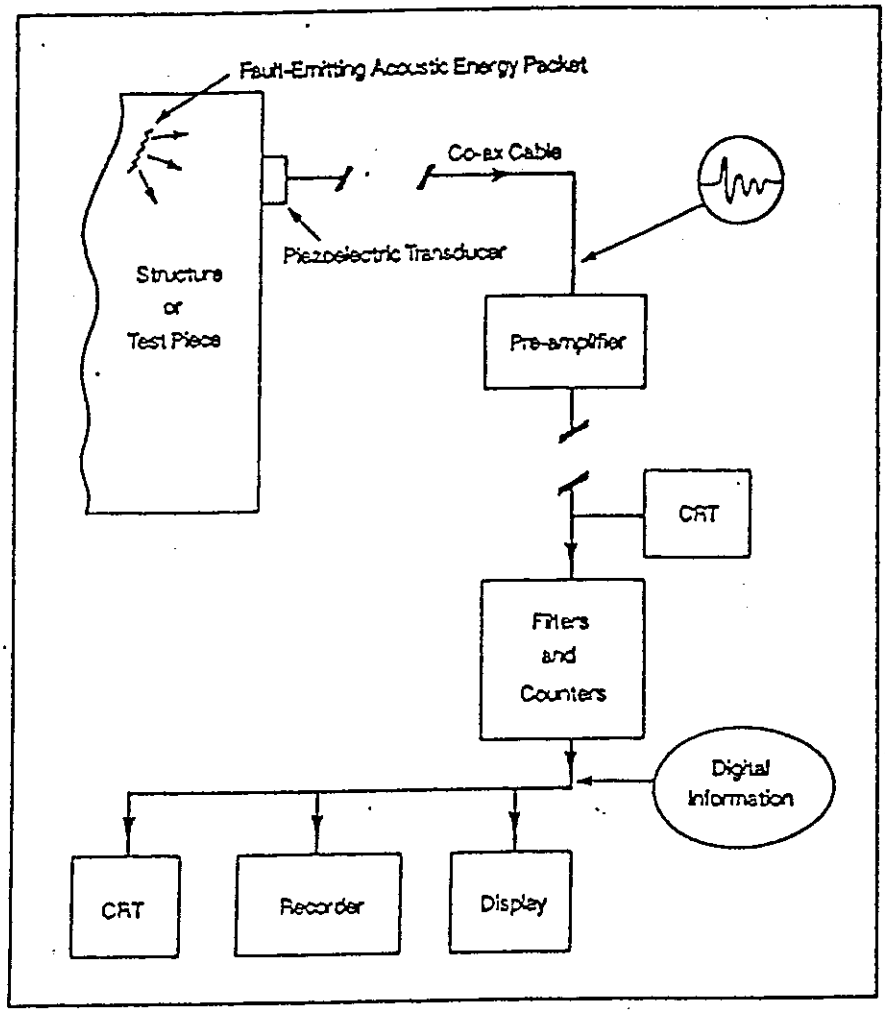

Fig. 3.9 : Acoustic Emission Monitoring System

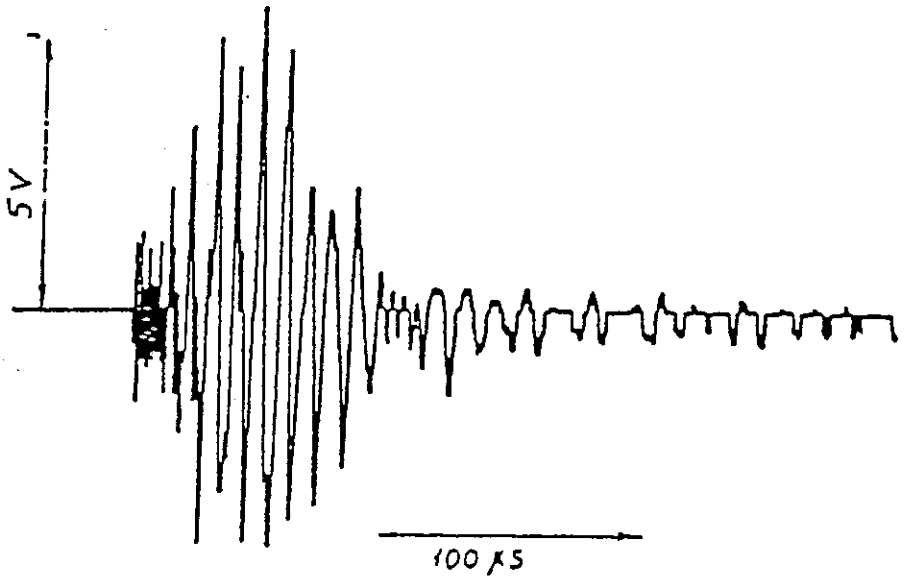

Fig. 3.10 : Typical Amplified Acoustic Emission Signals

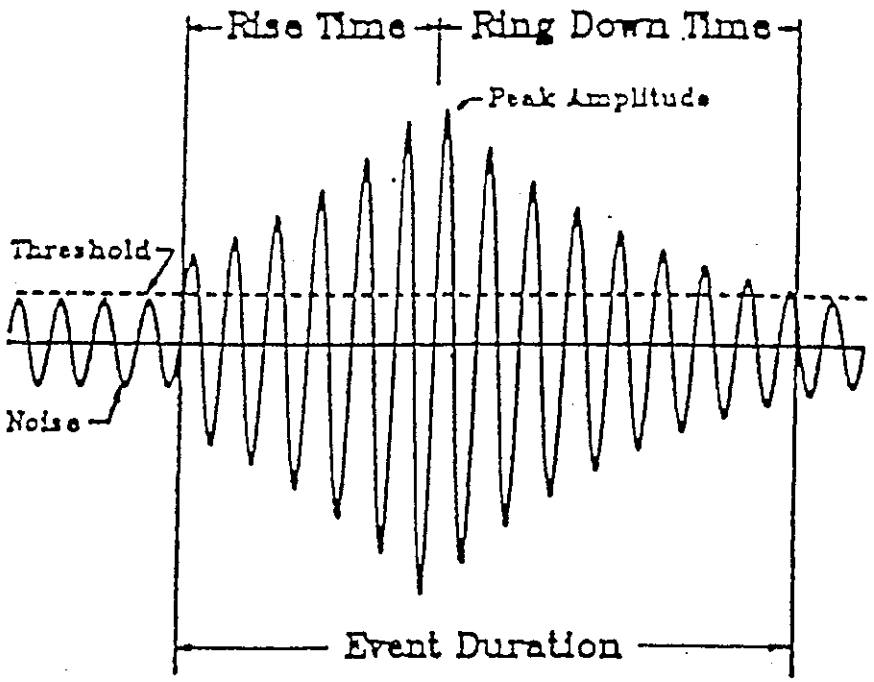

Fig. 3.11 : Some Acoustic Emission Signal Parameters

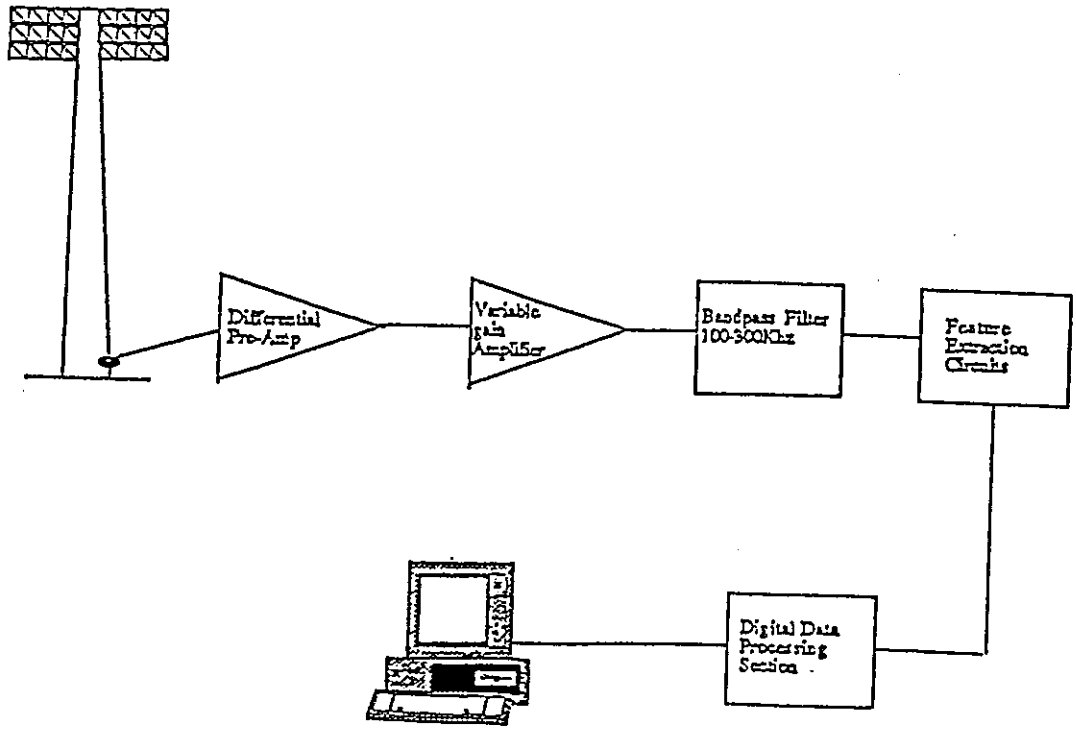

Fig. 3.12 : Schematic View of Monac System Attached to Tower Base Plate

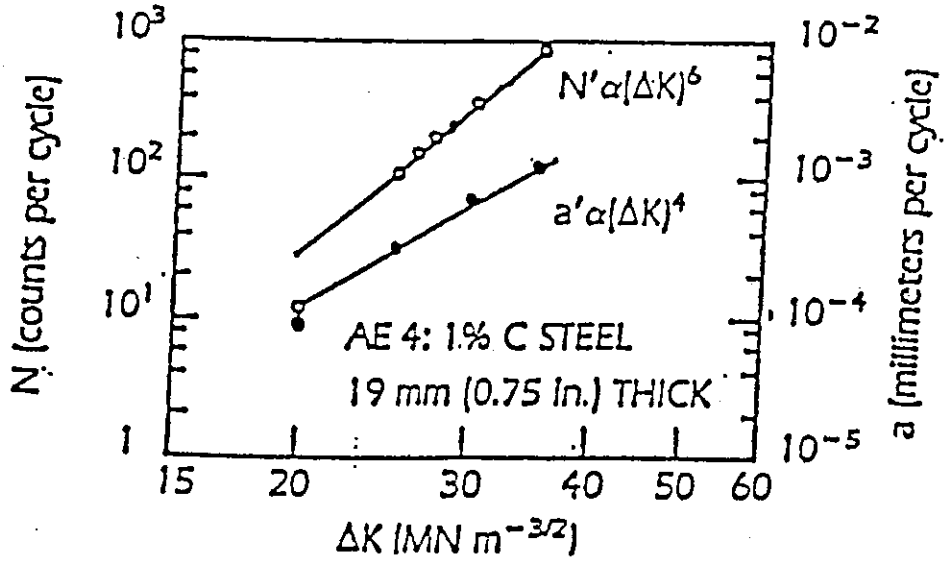

Fig. 3.13 : The Relationship Among Acoustic Emission Count Rate, Crack Growth rate and the Stress Intensity Factor for Two Steels

SECTION 4

RESULTS OF EXPERIMENTAL AND ANALYTICAL STUDY

4.1 INTRODUCTION

In this section the results from the experimental observations are presented, and a comparison made with analytical predictions. Firstly, the experimental and theoretical vibrational characteristics of the pole are analyzed. From these results the wind speeds at which across-wind effects are expected are determined. The bolt stresses observed over a six month period from November 1991 to May 1992 are presented next. These results are compared with the theoretical along-wind response. Differences between the theoretical and observed response illustrate the effects of across-wind behavior. Analytical relationships are then developed which relate bolt stress range and wind speed. These relationships are used to assess fatigue damage of each of the instrumented bolts.

4.2 VIBRATIONAL CHARACTERISTICS OF THE LIGHT POLE

Table 4.1 presents the analytically predicted and experimentally observed frequencies. The analytical prediction was determined from eigen frequencies by modeling the pole as a number of tapered beam elements with lumped masses at each of the node points. From the results it is evident that the close analytical/experimental agreement implies that the in-situ pole behavior was governed by base fixity with little indication of soil-structure interaction effects. Over the course of the six months of the study a number of frequency shifts were detected and are presented in Table 4.2. These could be explained by soil-softening in the springtime during the thaw period (which would shorten the frequency and increase damping), and the presence of some ice on the superstructure during the winter period. In any case, frequency changes were minimal and are not considered to affect the fatigue damage accumulation in the bolts. If frequency changes were more significant there would be more cause for immediate concern about the global integrity of the pole base.

Examination of the measured accelerations and bolt strains showed negligible torsional mode effects. Consequent bolt stress range cycling was characterized by relatively narrow-band cycling dominated by the fundamental frequencies of the pole in bending about its strong and weak axes.

The effective viscous damping of the pole in both directions of bending was 3.52%. This was determined using the half band-width method from the experimentally determined power spectral density (PSD) functions. This value is considered to be rather high for a light steel structure which may normally expect a damping value in the range of 0.5% to 2%. The difference, however, is attributed to aerodynamic (wind-structure interaction) damping. This composite value was used in the analytical modeling of dynamic response described in Section 2.3.3.

TABLE 4.1: VIBRATIONAL CHARACTERISTICS

	ANALYTICAL		EXPERIMENTAL	
	Weak	Strong	Weak	Strong
Frequency (1st) Hz	0.295	0.358	0.30	0.36
Frequency (2nd) Hz	1.50	1.92	1.47	2.05
Damping Ratio ξ (%)	--	--	3.52	3.52

TABLE 4.2 FREQUENCY AND DAMPING MEASURED OVER 6 MONTHS

DATE	WIND SPEED	WIND DIR.	MODE	FREQUENCY(Hz)		DAMPING (%)	
				Weak	Strong	Weak	Strong
12/14/91	23.5	50	1	0.30	0.37	3.51	3.52
			2	1.49	1.99	3.52	3.51
12/14/91	29.0	41	1	0.30	0.37	3.51	3.51
			2	1.49	1.98	3.51	3.53
12/14/91	30.0	52	1	0.30	0.37	3.51	3.53
			2	1.49	1.98	3.52	3.53
12/14/91	32.1	43	1	0.30	0.37	3.52	3.55
			2	1.49	1.97	3.52	3.56
1/14/92	19.9	78	1	0.30	0.367	3.52	3.58
			2	1.493	1.89	3.52	3.59
1/14/92	24.4	76	1	0.30	0.367	3.52	3.58
			2	1.48	1.89	3.52	3.58
3/10/92	16.7	61	1	0.30	0.353	3.54	3.68
			2	1.47	1.82	3.54	3.70
4/15/92	17.0	68	1	0.30	0.35	3.64	3.81
			2	1.49	1.83	3.63	3.85
5/12/92	9.0	6	1	0.30	0.35	3.72	3.89
			2	1.49	1.83	3.73	3.89

4.3 OBSERVED WIND ENVIRONMENT

The anemometer was employed for continuous measurement of the wind speed and direction at the stadium. The hourly mean speed and direction were extracted from the resulting wind records. Fig. 4.1 presents the histogram of these wind speeds observed at the stadium during the period of November 1991 - May 1992. The histogram shows a trend which is consistent with the 1972-1991 recorded wind data at the Buffalo Airport shown in Fig. 2.14. The Buffalo Airport hourly mean wind speed is also very near to the hourly mean wind speed recorded at the stadium.

Wind direction is also considered in the wind recording as shown in Fig. 4.2. In this figure, wind speed records are subdivided in to various categories based on its speed and direction. Wind records are categorized on the basis of mean hourly wind speeds as follows:

- 0 to 12.5 mph
- 12.5 to 17.5 mph
- 17.5 to 22.5 mph
- 22.5 to 27.5 mph
- $\geq$ 27.5 mph

The direction is subdivided into a 30° ($\pm$15°) segments labeled A to L. From Fig. 4.2 it is apparent that the predominant direction of wind is between 15° to 75° with respect to the pole's Y-Y axis. Experimentally recorded wind speeds also show that most of the wind speed occurrences are less than 12.5 mph. The occurrences of mean hourly wind speeds greater than 27.5 mph are less than 2% of the total recorded. A sample wind record is shown in Fig. 4.3, illustrating typical fluctuations observed for both speed and direction.

4.4 ACROSS-WIND RESPONSE PREDICTIONS

Table 4.3 presents the range of predicted wind speeds that are expected to cause across-wind response. From this table it is evident that some across-wind response may occur anywhere between 2 and 30 mph. This range depends on whether vortex shedding is occurring only over a portion of the pole (this gives the lower wind speeds), or the entire pole (based on the average pole width) and the angle of attack of the wind. Based on this range of wind speeds the across-wind response stress predictions are presented in Table 4.4 for first-mode behavior.

TABLE 4.3: RANGE OF WIND SPEEDS (MPH) FOR ACROSS-WIND RESPONSE

Mode of Vibration		Weak Axis Bending	Strong Axis Bending
First Mode:	Range	2 - 4	3 - 7
	Median	3	4.5
Second Mode:	Range	7 - 20	18 - 30
	Median	15	26

TABLE 4.4: CALCULATED BOLT STRESSES (ksi) FOR FIRST-MODE ACROSS-WIND RESPONSE

Bolt		Weak Axis Bending	Strong Axis Bending
Bolt 1	Range	0.5 - 1.33	1.5 - 4.0
	Median	0.88	2.6
Bolts 2 and 3	Range	0.70 - 1.86	0.94 - 2.4
	Median	1.20	1.60

4.5 OBSERVED BOLT STRESSES

Figs. 4.4 to 4.7 present the experimental results of the stresses directly measured by the strain gauges affixed to the bolts. In Figs. 4.4 to 4.7 the average five minute wind speed was divided into 12 quadrants designated from A to L. The directionally dependent results are plotted with their respective quadrant letter. It will be noted that the prevailing wind comes from Lake Erie with an approach angle of 30° (±15°) to the longitudinal axis of the football playing field. Thus most results are in quadrant B , but a selection is also presented for the other quadrants.

As might be expected, due to the vagaries of the wind speed and direction, there is a significant amount of scatter in the results. However, a lot of the scatter can be explained as a result of the poles' dynamic response to the wind. Because the pole is symmetrical about the two orthogonal (x,y) directions, which both possess distinct vibrational characteristics, the response is somewhat dependent on modal superposition. Thus either complete coupling or uncoupling of the two orthogonal modes may be expected.

Uneven transfer of pole base moments to the hold-down bolts may also account for some of the differences between expected and recorded bolt stresses. The following subsection briefly presents measured pole base moments and their distribution to bolt stresses.

4.6 ANALYTICAL STRESS PREDICTIONS

4.6.1 Response Time-Histories:

A computer program was developed in *FORTRAN* to perform the simulation and analysis described earlier in Section 2. The program was used to predict the stress-time histories in the bolts using the actual site-recorded wind speeds and directions. It should be noted that only along-wind response is predicted by this method. The predicted time histories were compared with the actual bolt stress time histories obtained from the strain gauges (Fig. 4.8). It is apparent that the theoretical and experimental stresses for Bolt 1 show a good agreement in terms of average, standard deviation and pattern of variation. In the case of Bolt 2, although the time-history pattern and standard deviation agree reasonably well, the average for the experimental stresses is higher than the analytically predicted stresses. This may be explained by variety of factors, the simplest being that the strain gauges were wired as a quarter-bridge so that over time the mean strain will drift due to a lack of thermal compensation. Other possible reasons include the redundancy of the 16-bolt base connection, across-wind effects for the dominant wind direction, inadequacy of the assumptions used in deriving bolt stresses from the base moments and secondary P-delta effects in the pole.

It is considered that in general however, the bidirectional SDOF idealization provides an adequate representation of the dynamic response of the pole structure, and providing across-wind response is not significant (as is the case for the more fatigue-critical high wind speeds) a reliable analytical prediction can be made of the transient behavior.

The foregoing comparisons of the theoretical and actual results not only serve to validate the assumptions used in formulating the analytical model but also highlight its limitations. However, it may be safely concluded from these comparisons that the analysis predicts the structural behavior to a reasonably acceptable degree of accuracy. One of the purposes of developing such a model was to generate time histories of structural response

from simulated or actual wind records (scaled up) for extreme loading conditions that may affect the structure during its lifetime but cannot be possibly recorded in the course of the limited duration of experimental measurements. Such time histories are not only useful for structural design purposes but may also be used to estimate the parameters required for the fatigue damage and life assessment of the pole. A following section of this report presents the important predictions that were made about the extreme wind behavior of the pole.

4.6.2 Transient Response Predictions:

The most important parameter of interest in fatigue damage evaluation is the effective stress range, S_r. It is also of interest to compare this response with: the standard deviation of stress σ_{std}; the 5 minute average stress, σ_{avg}; and the maximum stress, σ_{max}. The theoretical stress-time histories were used to evaluate the effective stress ranges in Bolts 1, 2 and 3 using the Rainflow counting method. The theoretically predicted stress ranges for several wind records are also plotted against the mean five-minute wind speed for each of the bolts in Figs 4.4 to 4.7. It is evident from these plots that the predicted stress ranges show an excellent agreement with the experimental values, with the exception of low wind speeds. This difference in the observed experimental bolt strains, and those predicted using actual wind speed records, is primarily due to across-wind response. The differences are most noticeable for the first mode across-wind response speeds from 2 to 7 mph .

Another anomaly in the results are observed stresses higher than predicted for directions E, F, and G for velocities of 7 to 10 mph. This may be attributed to wind channeling over the top of the stadium where the overturning moments are amplified due to higher pressure over the upper portion of the pole.

It is also of interest to note that the transition period between non-turbulent and turbulent flow between 11 and 18 mph is captured well by the analytical modeling and corroborated by the experimental observations. The along-wind stresses are for turbulent

flow ($V > 20\ mph$) and non-turbulent flow ($V < 10\ mph$) which are proportional to the drag factor C_d and hence V^2. For the transitional flow ($10 < V < 20\ mph$) due to the varying nature of the drag factor ($C_d \propto Vd^{1.3}$ according to [AASHTO-85]) the stresses are proportional to $V^{0.7}$.

By curve fitting the experimental results, the following relationships were established.

$$\text{Bolt 1} \qquad \max \begin{cases} S_r = 0.3\ V^{0.7} \\ S_r = 0.0075\ V^2 \end{cases}$$

$$\text{Bolt 2} \qquad \max \begin{cases} S_r = 0.2\ V^{0.7} \\ S_r = 0.0064\ V^2 \end{cases}$$

$$\text{Bolt 3} \qquad \max \begin{cases} S_r = 0.3\ V^{0.7} \\ S_r = 0.0055\ V^2 \end{cases}$$

The resulting stresses S_r determined by the Rainflow counting method were compared with the standard deviation results, σ_{std}. The general trend shows that there is a factor of 2.6 to 3.0 difference between σ_{std} and S_r. This is in accordance with Eq. 49 from Section 2 where

$$S_{re} = 2\sqrt{2}\ \sigma_{std} = 2.83\ \sigma_{std}$$

It is evident that for this class of random wind loading, damage accumulation can be determined directly from the PSD function and/or the standard deviation of the time-history response.

4.7 DAMAGE DENSITY FUNCTIONS AND FATIGUE LIFE

The historically observed probability distribution for wind (PDF) was used in conjunction with the experimentally observed bolt stresses to determine *Damage Density Functions* for each of the instrumented bolts. The analytical relationships presented in Section 4.6.2 are multiplied by the winds' unit probability density function for the pole's lifetime period (1972-91). A *unit damage density function* (DDF) is then derived for each bolt. These curves are plotted on Fig.4.9. It is evident that even though the probability of a high wind speed is low, damage that occurs during such an event can be quite significant.

A cumulative damage density function can also be derived by numerically integrating the individual DDF's. The resulting cumulative distributions of damage of plotted in Fig.4.10. From this figure the 50 percentile wind speeds can be identified for each bolt. Also, by using Eq. 48 an equivalent constant amplitude stress range (RMC) can be derived. Then using Eq. 45 the bolt-life till first fatigue crack can be assessed.

Table 4.5 presents a summary of the results for the fatigue-life analysis. The results show that Bolt 1 is the most fatigue-prone bolt, with Bolts 2 and 3 projecting similar fatigue lives. It should be emphasized that the results are somewhat imprecise due to: variability of wind speed results; assumptions made in the fatigue model used (Eq. 40); and the inherent approximations in the rainflow cycle counting method. Nevertheless, because the averaging processes were taken over a long time period a reasonable degree of confidence can be placed in the resulting trends. Obviously a clear case can be made for the fatigue life of the bolts being consumed in less than 20 years.

TABLE 4.5 RESULTS OF FATIGUE DAMAGE ANALYSIS

	BOLT 1	BOLT 2	BOLT 3
$V_{50\%}$ (mph)	26.3	21.4	26.9
$S_{50\%}$ (ksi)	5.55	2.57	4.64
S_{re} (ksi)	2.68	2.06	2.11
S_{re}^{*} (ksi)	2.88	2.21	2.26
T_f $(years)$	17.8	39.2	36.6

4.8 PEAK STRESS PREDICTIONS

The peak stresses were analytically predicted for two wind records (Winds 22 and 23) and plotted against the mean wind speed for bolts 1,2 and 3 (Fig. 4.8 a,b and c respectively). The plots also include the experimental values for the given bolt for a large number of site-recorded winds including the aforementioned winds. It can be seen from these plots that the theoretical values fit reasonably well with the experimentally observed values.

In order to estimate the bolt stresses caused by extreme winds, one of the highest recorded winds (Wind 23, Mean wind speed = 32.1 mph) was used. Firstly, Wind 23 was scaled up to a mean of 48 mph which was the maximum average wind speed observed over the 20 year pole life. The time-history analysis was used to determine the peak stresses as well as the stress ranges for the three bolts. Secondly, the same wind (Wind 23) was then scaled up to a mean of 56 mph which corresponds to a design return period of 50 years and the dynamic analysis repeated. The results of the two predictive analyses are presented in Figs 4.4 to 4.7. It is evident from the predictive results in these figures that the maximum bolt stress was computed to be 35 ksi based on an average of 48 mph wind speed. This is well below the maximum allowable stress in tension which is given by the *AASHTO* code as:

$$f_t = (140\%)(0.6f_y) = 0.84f_y = 63\ ksi$$

in which the yield stress for the anchor bolts is f_y = 75 ksi. It is apparent that the bolts have not yielded and thus have not been subjected to low cycle fatigue resulting from inelastic strain cycling if nut snugness during the 6 month instrumentation period is representative of conditions over the 20 year life of the pole to date.

For the future life of the pole it is also apparent that for a 50 year return period anchor bolt yielding is unlikely to occur.

TABLE 4.6: RESULTS OF PEAK STRESS PREDICTIONS (SCALED WIND23)

	BOLT 1	BOLT 2	BOLT 3
σ_{max} [1972-91] (*ksi*)	34.4 C	13.2 C	27.5 T
σ_{max} [T = 50 *yrs*] (*ksi*)	47.0 C	18.2 C	37.6 T
σ_{max} / f_t [f_t = 63 *ksi*]	75 %	29 %	60 %

C = Compressive stress T = Tensile stress

4.9 ASSESSMENT OF POST-CRACKING FATIGUE LIFE

As described in Section 3, the initiation of detectable cracking does not necessarily exhaust the fatigue life. This section utilizes relevant results of the acoustic emission crack monitoring with the fracture mechanics of crack propagation to estimate the severity of bolt cracking in terms of predicted remaining life.

4.9.1 Acoustic Emission Activity in Instrumented Bolts

Direct results of the acoustic emission monitoring may be summarized as follows:

1. High acoustic emission activity occurred during January, corresponding to several high wind records. Activity was significantly reduced during subsequent months. The cumulative number of acoustic events during the 22 day period from January 8 to 28 is as shown in Figs. 4.11 to 4.13 for each of the three anchor bolts. The average January event rates were 0.42, 0.33 and 0.09 events per cycle for bolts #1, #2, and #3, respectively.

2. The crack in bolt #1 was active and experiencing stable growth. Table 4.7 and Fig. 4.14 illustrate the acoustic activity on one of the more acoustically active days, January 17, 1992, during a high wind of about 25 mph with a wind direction of 60°.

3. The crack in bolt #2 was also active and experiencing stable growth. Table 4.7 and Fig. 4.15 illustrate its acoustic activity during the same high wind of about 25 mph at 60°.

4. As is shown in Table 4.7 and Fig. 4.16, no significant acoustic emission activity was recorded in bolt #3, consistent with the lack of ultrasonic test indication at this bolt (refer to Fig. 3.12).

5. Little acoustic emission activity was recorded at wind speeds less than 10 mph. This implies that fatigue cracks in bolts #1 and #2 will not grow at speeds lower than 10 mph.

Since there is stable crack growth under higher wind conditions, proof tests would not be an adequate way to assess the integrity of the cracked bolts.

4.9.2 Estimation of ΔK

Since the wind velocity and direction varied constantly, load conditions were random and varied. Due to these variations, the approximations inherent in the acoustic emission nondestructive technology, and other uncertainties (e.g., about crack geometries), only an approximate range of changes to the stress intensity factor can be estimated over selected time periods. The semi-circular, straight, sickle-shaped, and annular crack front geometries were each considered in this evaluation.

For the active wind conditions of Jan. 17, the acoustic emission results correspond to a stress intensity factor range ΔK in bolt #1 of between about 8 and 18 $ksi\sqrt{in}$, and slightly less than that in bolt #2.

4.9.3 Estimation of Post-Cracking Fatigue Life

The acoustic emission results may be used with fracture mechanics-based models to predict remaining fatigue life, but only by making assumptions about bolt material parameters and crack geometry, both of which are unknown. Normally, ΔK values such as those shown above are not too serious, corresponding to only small crack growth rates da/dN. When combined with stress range data obtained simultaneously, however, initial flaw sizes a_0 on the order of 0.4" to 0.9" result.

With such relatively large initial flaw sizes, remaining fatigue lives are consistently estimated to be less than a year, regardless of the assumed flaw geometry. Such estimates, of course, neglect the softening effect of an increasing crack size in a bolt. This softening effect would reduce the magnitude of stress range developed in the bolt and prolong its fatigue life by taking advantage of the structural redundancy inherent in the anchorage system. Nonetheless, the additional stress ranges thrown into the adjacent bolts will accelerate the consumption of their remaining fatigue lives.

Thus, it may be possible to allow the existing cracks to grow for some period of time. But should remediation not be promptly made, it is important to monitor the crack condition during the windy season, particularly during the winter. Redundancy analyses should be performed, to quantify the structural reliability in a scenario where one or two bolts fail before being replaced or otherwise remediated.

To enable a more accurate prediction of crack growth rates, it would be necessary to conduct laboratory material testing to characterize the relation or crack growth rate to acoustic emission properties for the specific type of steel used in the anchor bolts. Such laboratory testing should consider that the estimation of stress intensity factors in this study were subject to several restrictions. The varying wind velocities resulted in random loading histories, while the averaging process over discrete time intervals may only reflect the average crack severity during each time period. In addition, the crack shapes in the bolts are likely to be different than those in laboratory test specimens. It is important to note that neither the size nor the shape of the cracks (both of which are needed for calculation of remaining fatigue life) can be determined accurately from current ultrasonic and acoustic emission nondestructive techniques.

TABLE 4.7 : ACOUSTIC EMISSION RESULTS FOR JAN. 17, 1992

Time (hr:min)	13:40	16:40	17:41	18:41
Wind Speed	23	25	26	22
Dir. (Fig.4.2)	59°	59°	62°	62°
Acoustic count rate (counts per cycle)				
Bolt # 1	78	50	80	20
Bolt # 2	32	24	34	22
Bolt # 3	2	< 2	< 2	< 2

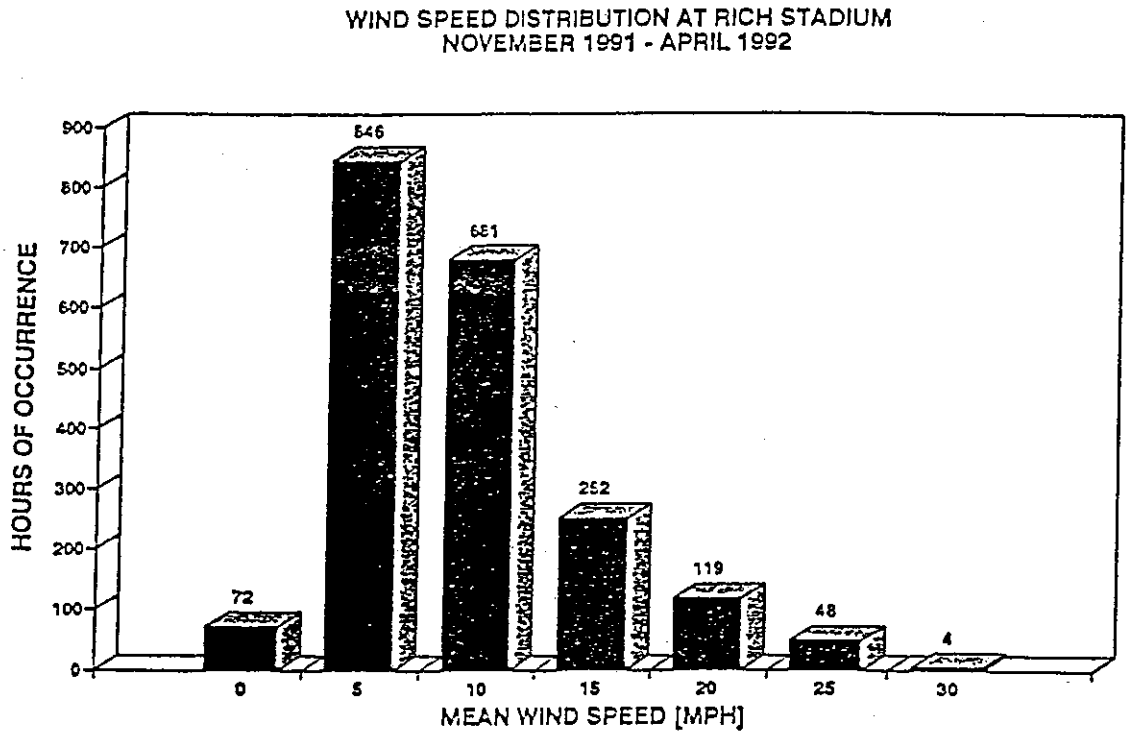

Fig. 4.1 : Histogram of Hourly Average Wind Speed at Rich Stadium

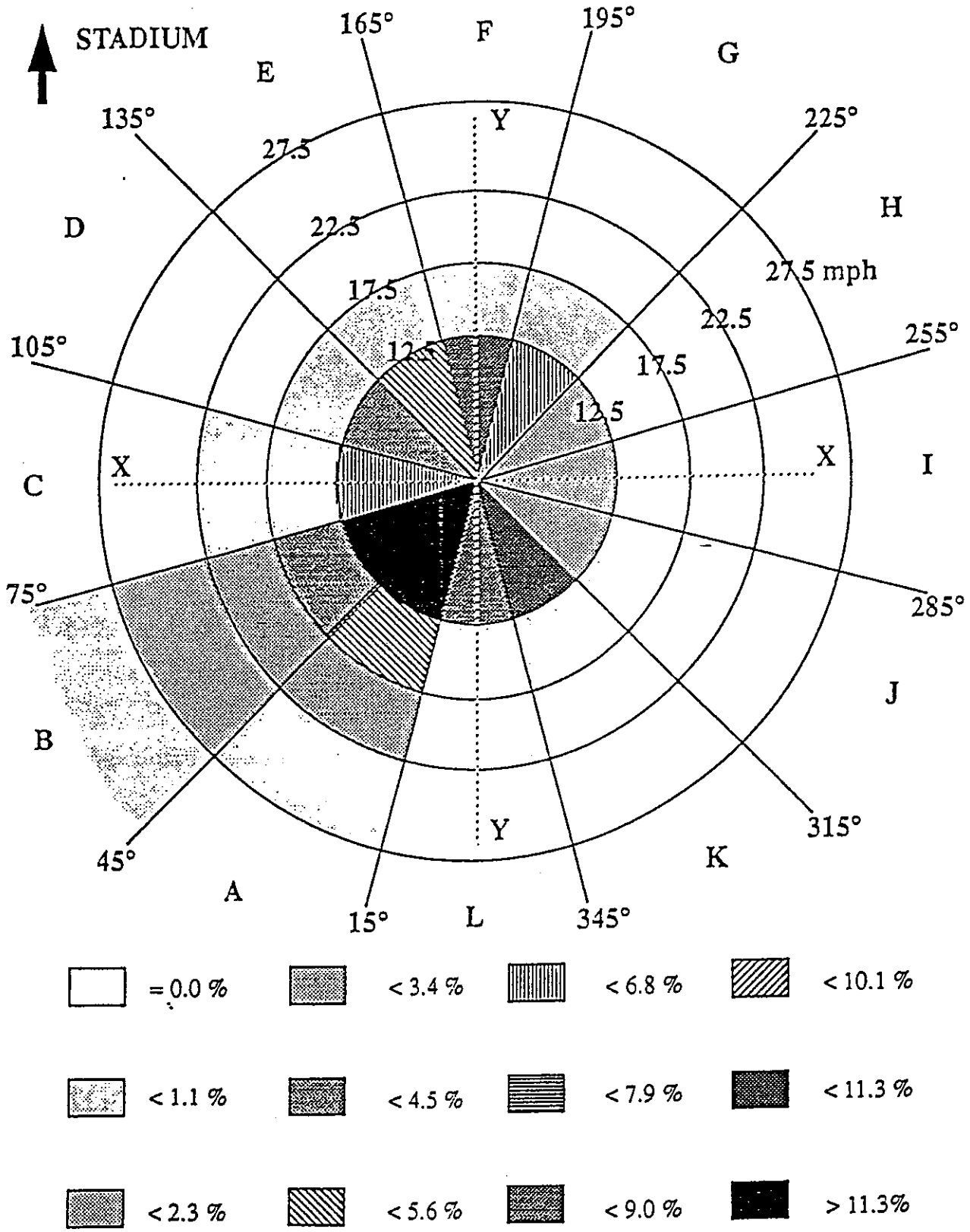

Fig. 4.2 : Recorded Wind Occurrences at Rich Stadium

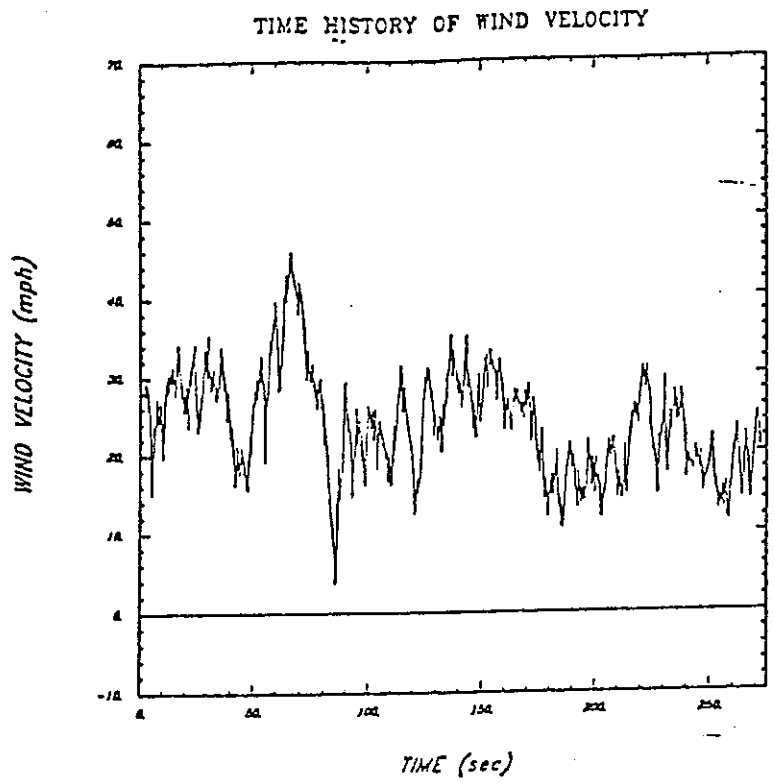

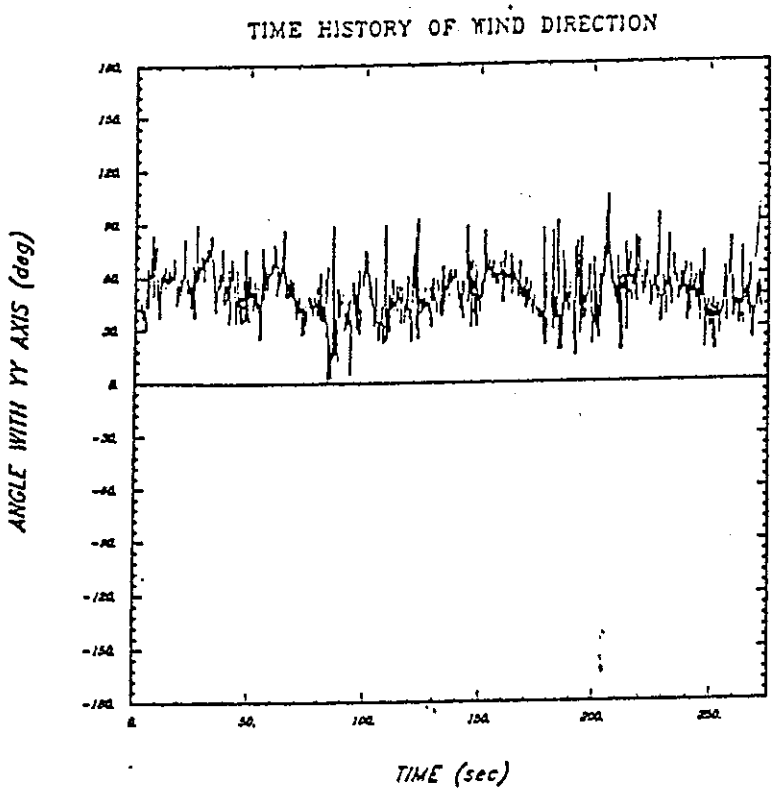

Fig. 4.3 : Sample Wind Record at Rich Stadium

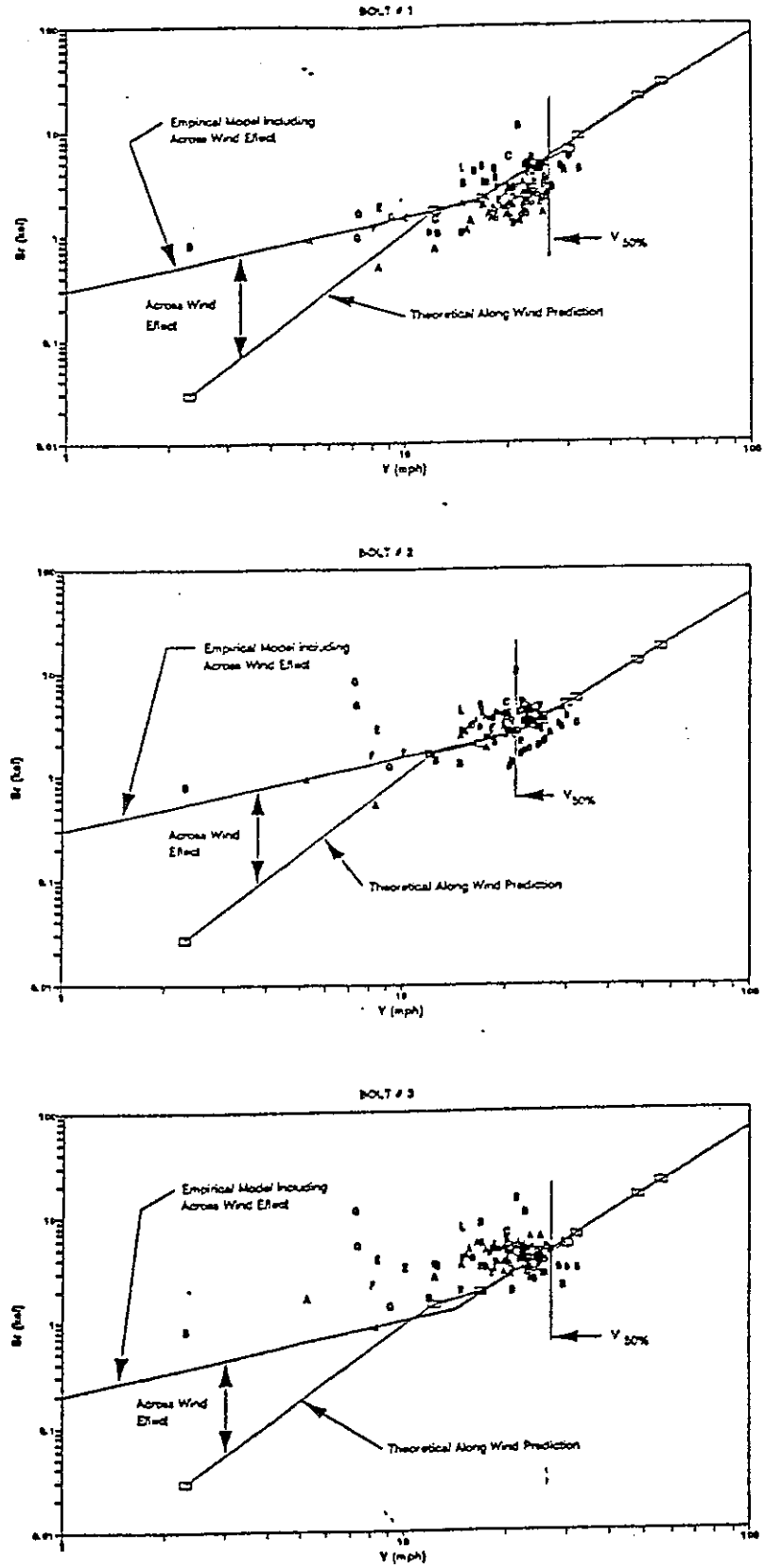

Fig. 4.4 : Effect of Wind Speed on Stress Range of Instrumented Bolts

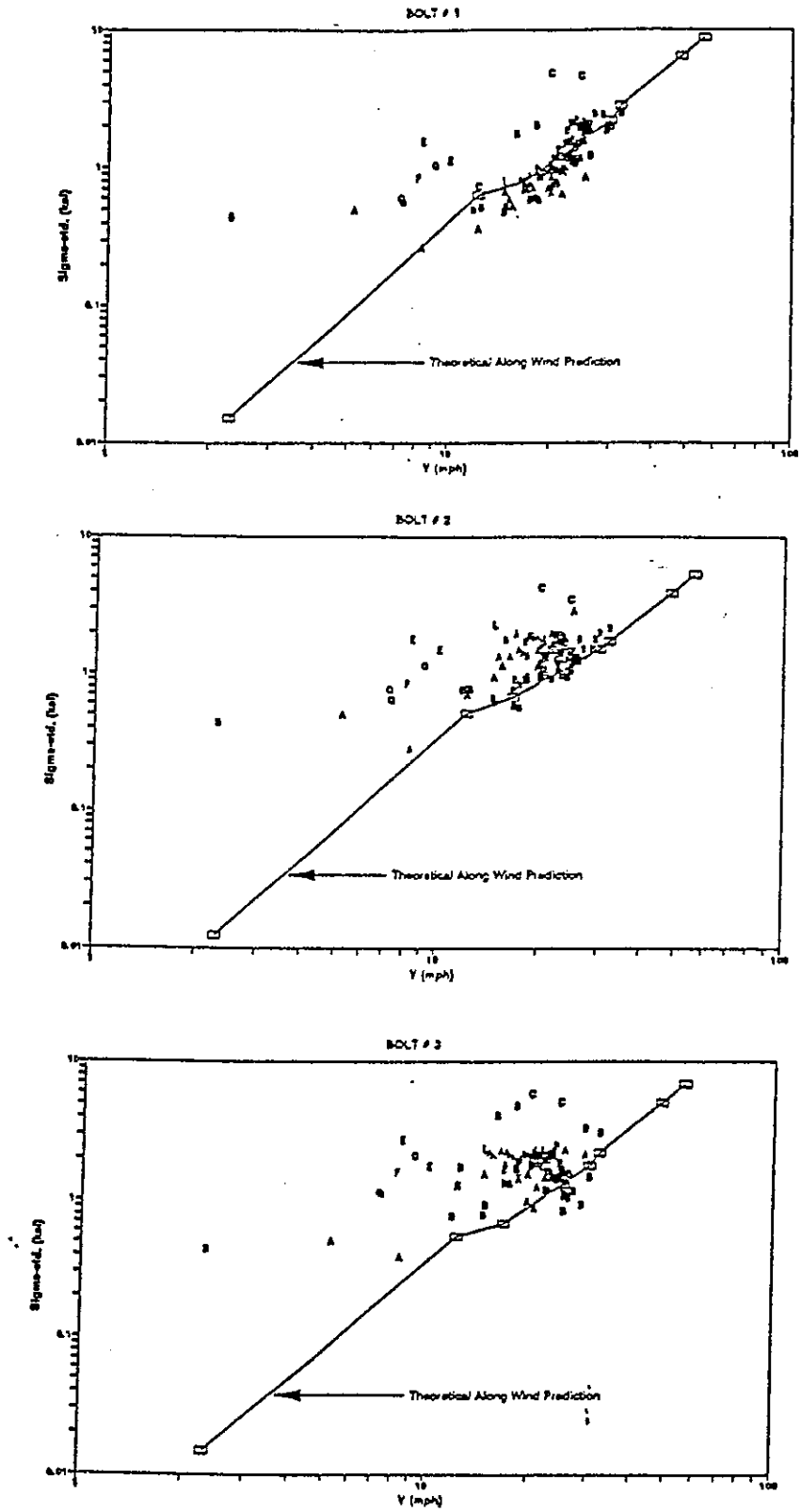

Fig. 4.5 : Effect of Wind Speed on Standard Deviation in Stress

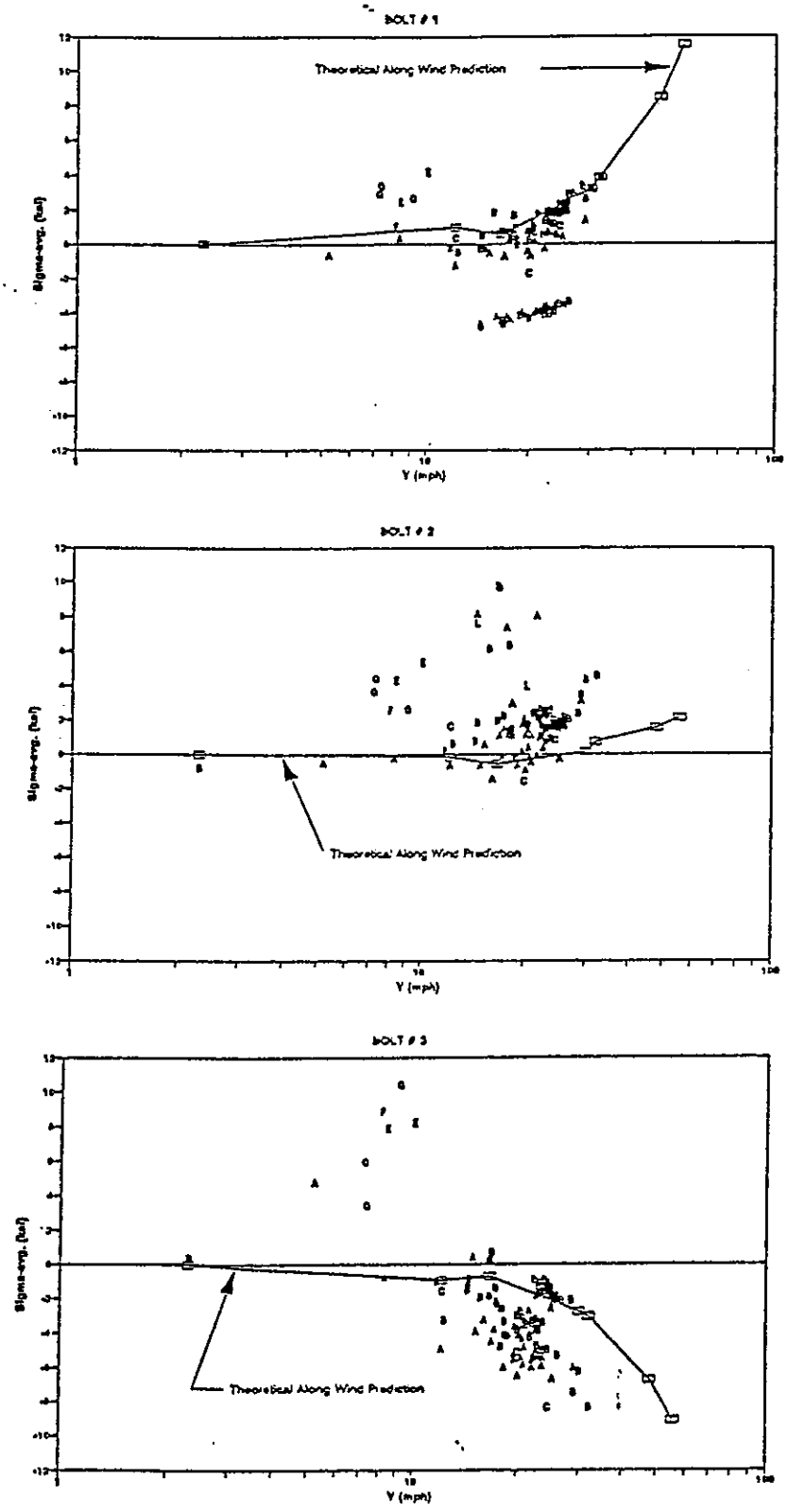

Fig. 4.6 : Effect of Wind Speed on Average Stress

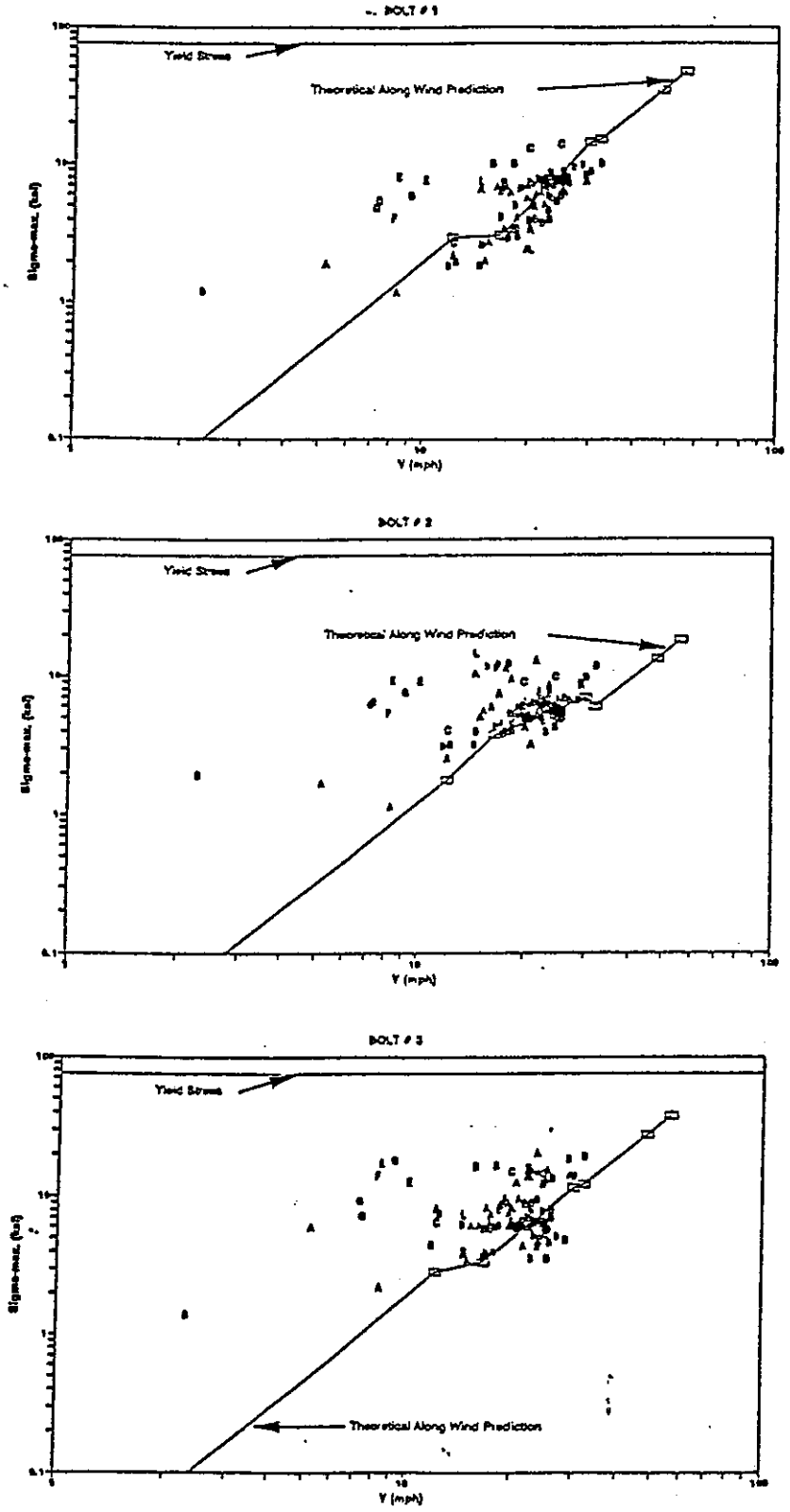

Fig. 4.7 : Effect of Wind Speed on Maximum Stress

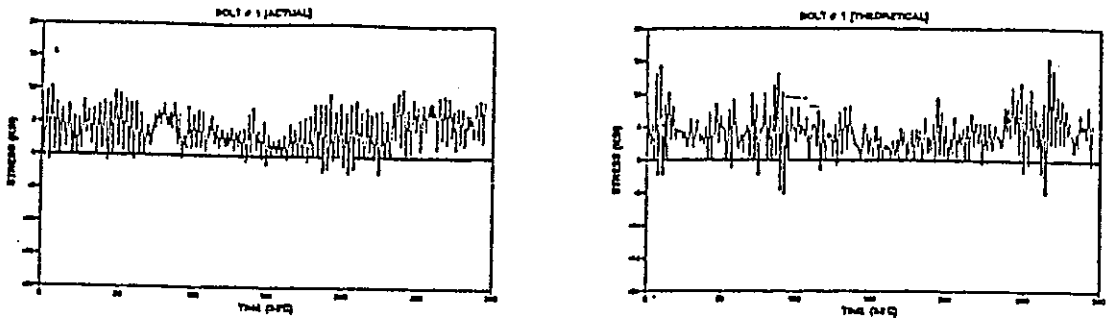

(a)

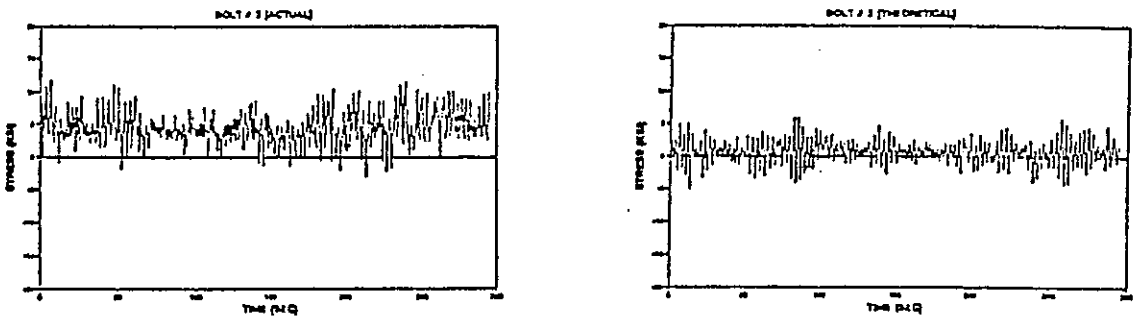

(b)

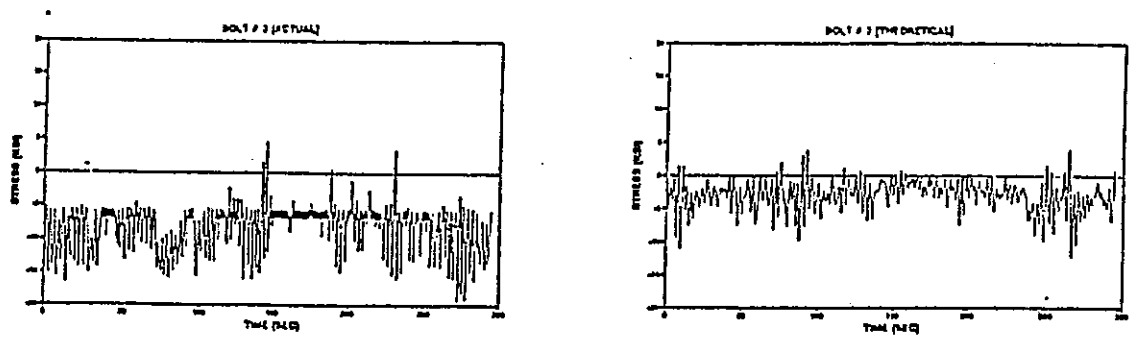

(c)

Fig. 4.8 : Comparison of Measured Bolt Stresses and Theoretical Bolt Stresses

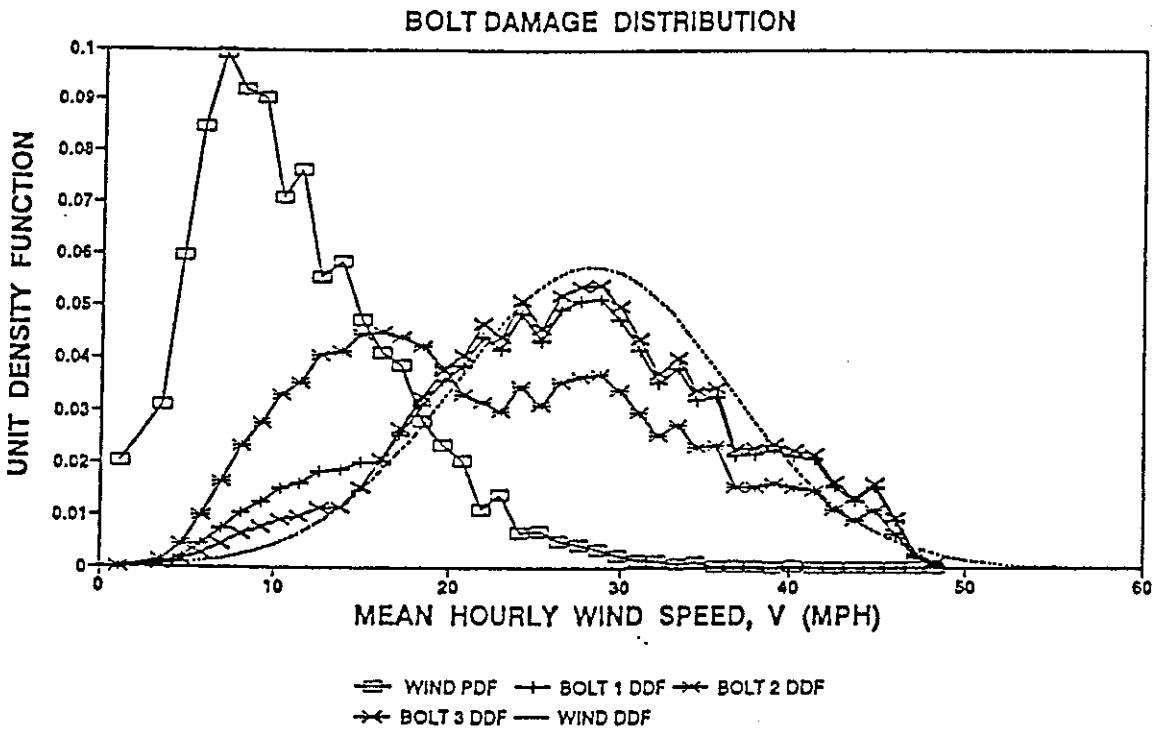

Fig. 4.9 : Damage Distribution Function of Instrumented Bolts

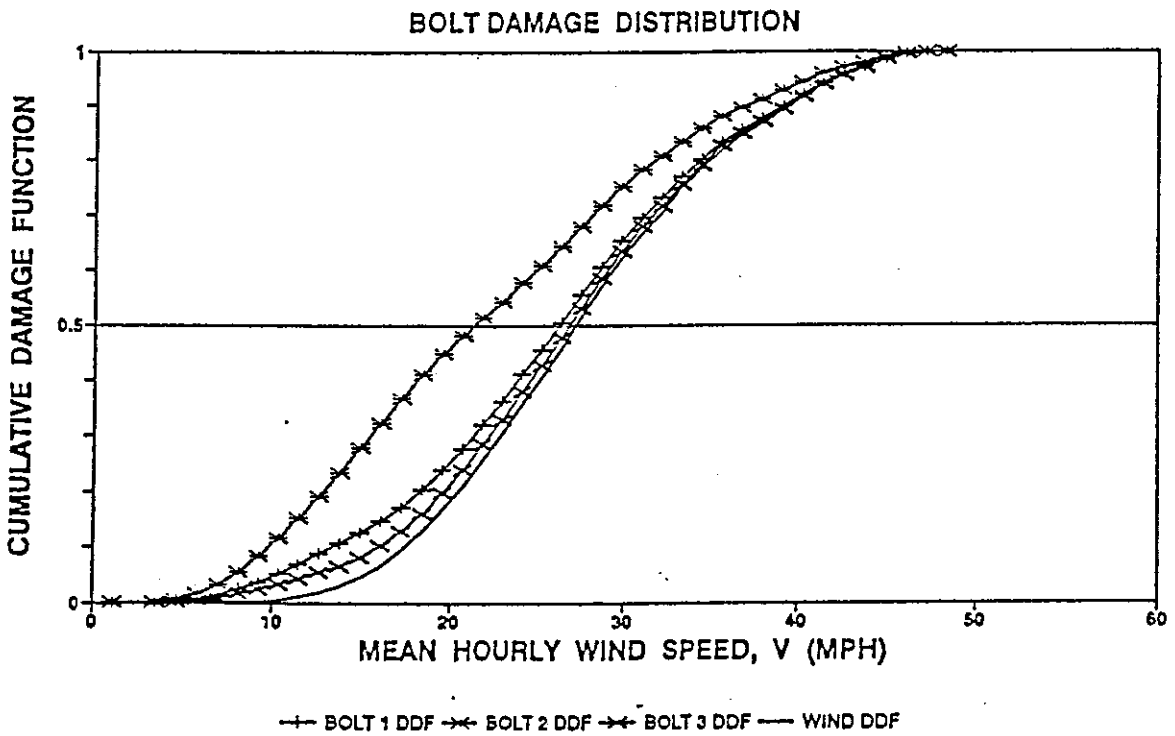

Fig. 4.10 : Cumulative Damage Distribution of Instrumented Bolts

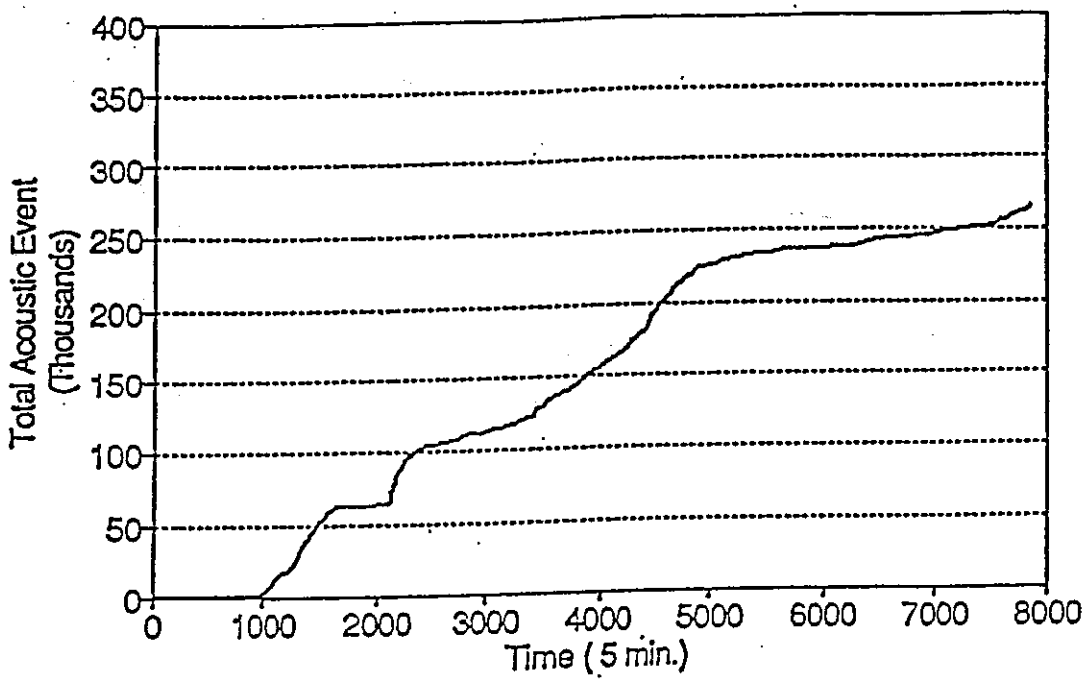

Fig. 4.11 : Cumulative Acoustic Events for Bolt # 1 Over the Period from January 8 to 28, 1992

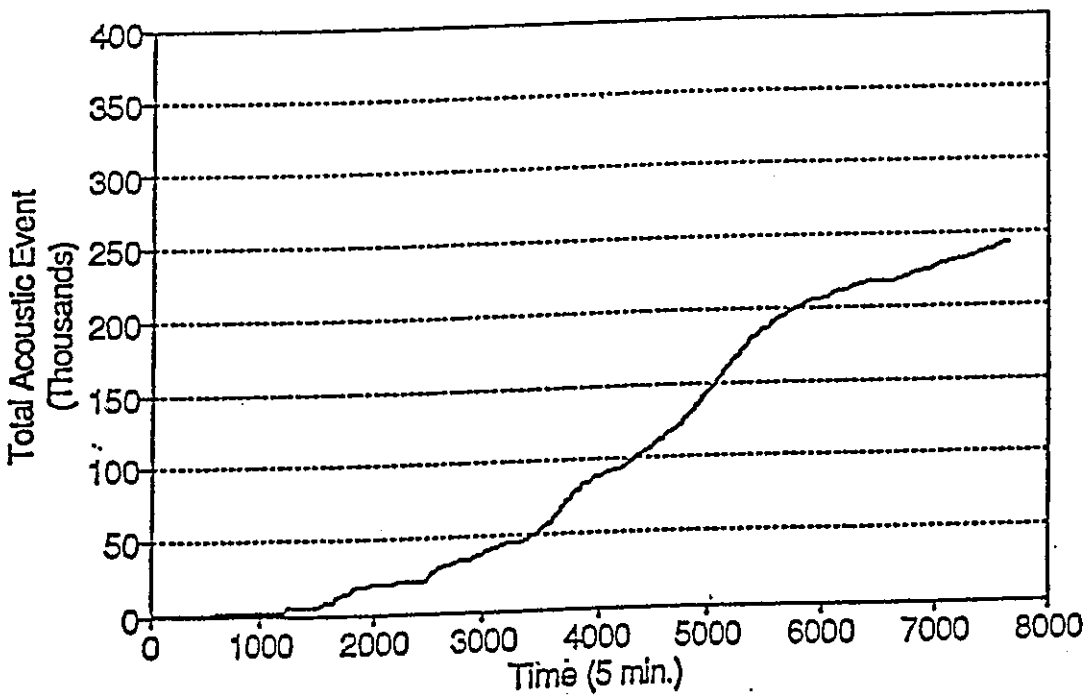

Fig. 4.12 : Cumulative Acoustic Events for Bolt # 2 Over the Period from January 8 to 28, 1992

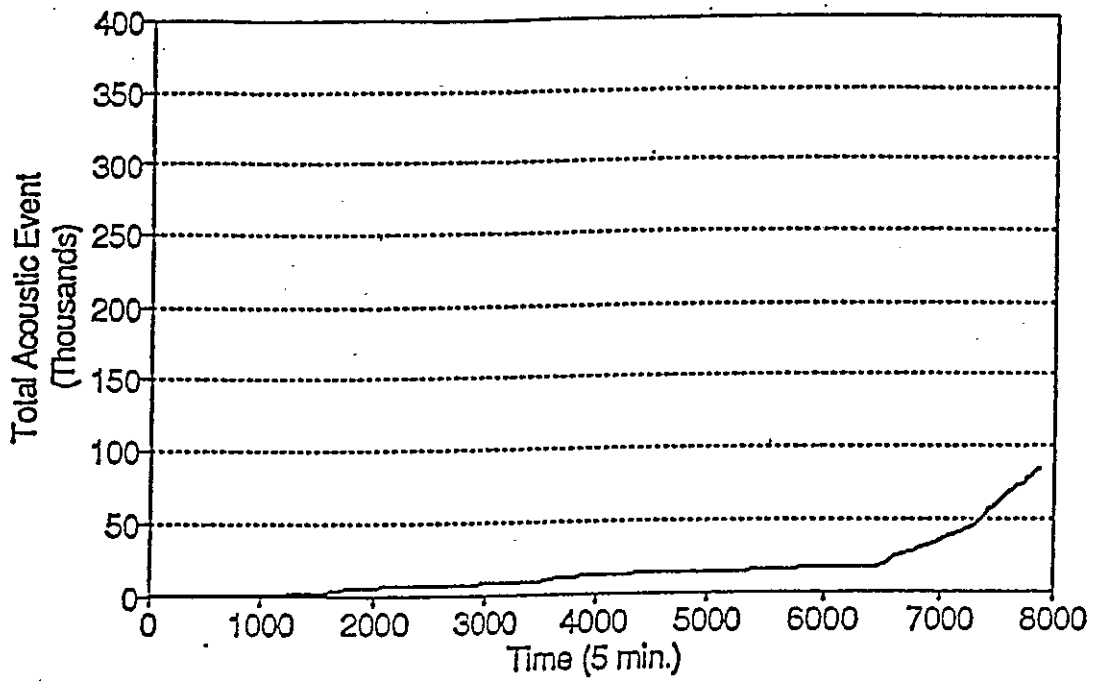

Fig. 4.13 : Cumulative Acoustic Events for Bolt # 3 Over the Period from January 8 to 28, 1992

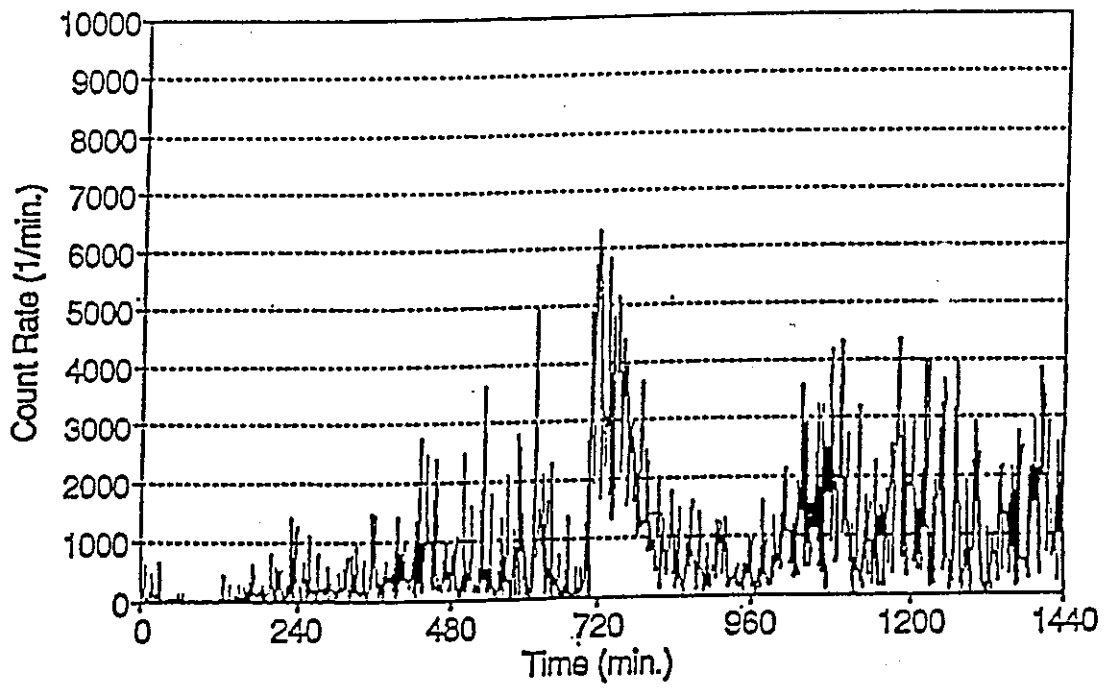

Fig. 4.14 : Acoustic Activity of Bolt # 1 During High Winds on January 17, 1992

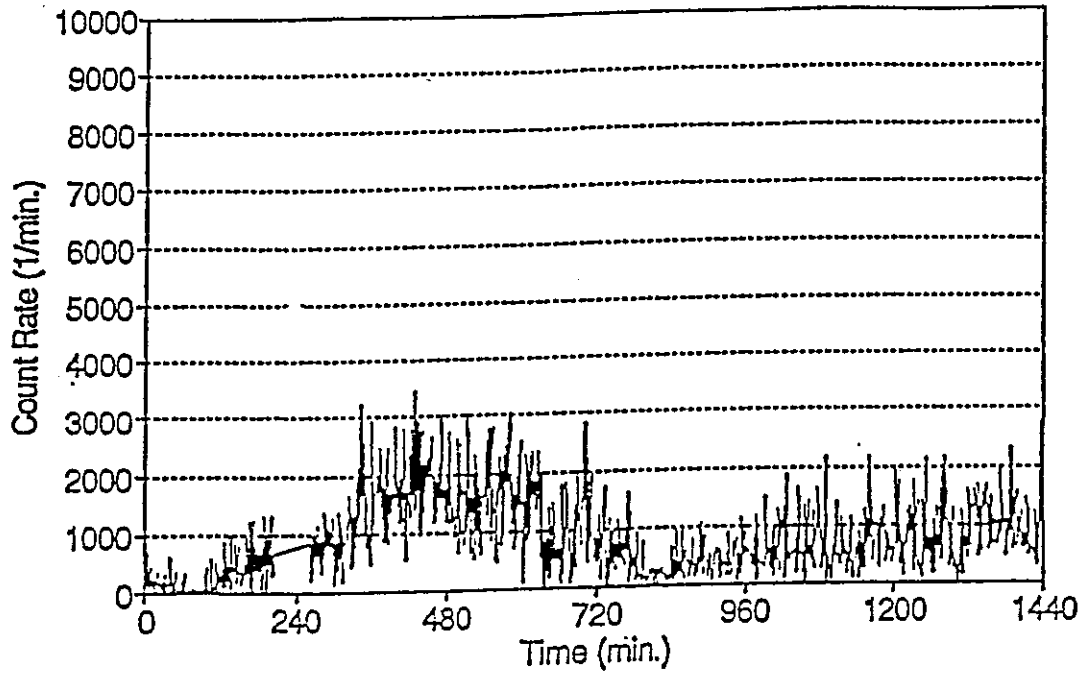

Fig. 4.15 : Acoustic Activity of Bolt # 2 During High Winds on January 17, 1992

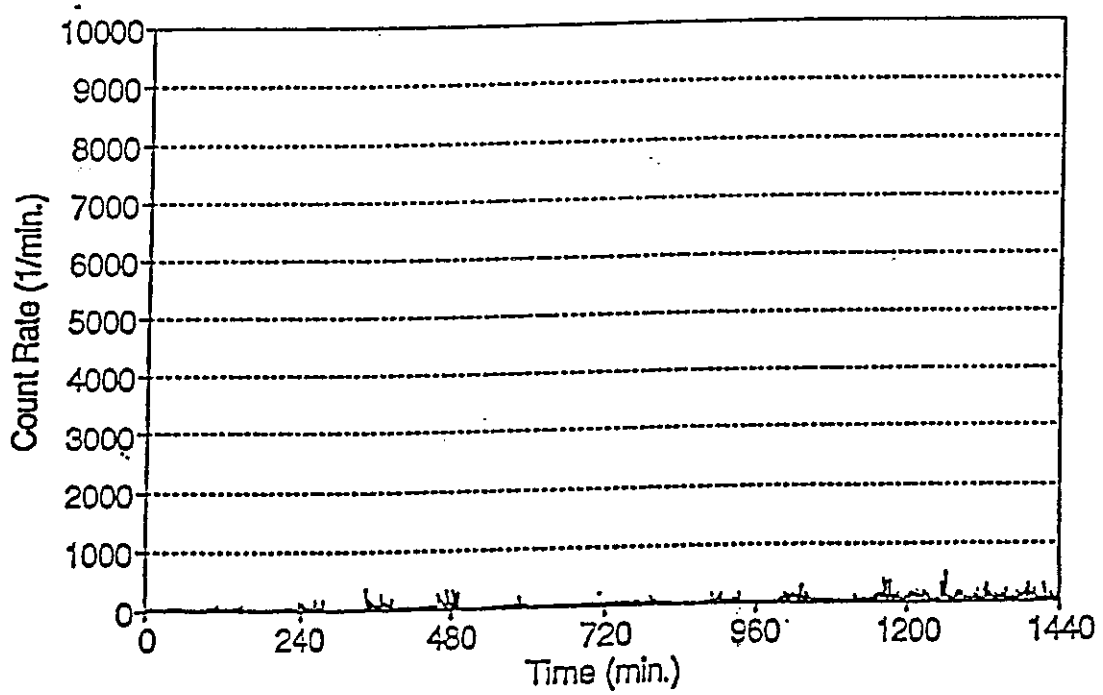

Fig. 4.16 : Acoustic Activity of Bolt # 3 During High Winds on January 17, 1992

SECTION 5

FATIGUE RETROFIT PROPOSALS

5.1 INTRODUCTION

It is evident from Section 4 that fatigue induced damage has occurred to the Rich Stadium field light poles owing to an initial absence of fatigue resistant design. Analysis of post cracking fatigue damage shows that it is inevitable that fracture of some bolts will result some time in the future. Owing to limitations in the present state-of-the-art in nondestructive evaluation of fatigue cracks, the remaining life is uncertain, but analysis shows that it may not be long, perhaps less than a year for the most severely cracked bolts. If full fracture (separation) does occur, there is sufficient redundancy remaining in the base anchorages to prevent a catastrophic collapse. However, the strain range and hence damage growth rate to the remaining bolts will increase.

Clearly, some form of remedial action should be taken soon. If this cannot be completed before the forthcoming football season, then constant Acoustic Emission and dynamic response monitoring of the existing fatigue cracks as well as regular visual inspections should be undertaken.

The foregoing analysis of the experimental results shows that the primary cause leading to the present situation is repeated stress cycling of the anchor bolts. In order to improve the remaining life of the poles, such stress cycling should be minimized and if possible eliminated.

Herein we propose a three-phase retrofit that will firstly minimize stress range and secondly virtually eliminate stress on the existing bolts for all winds except perhaps for the rare strong wind event.

5.2 PHASE I: RESEATING THE ANCHORAGES

It is considered that one of the primary reasons for the relatively short fatigue life to date is due to the bolts being subjected to full tension-compression stress range cycles. Compression cycles arise due to the base plate being seated on the leveling nuts, and tension cycles are due to the anchor (top) nuts holding the pole down from the overturning loads. Even though grout was placed in the space between the steel base plate and concrete pedestal at the time of construction, creep and shrinkage would require that compressive loads be transferred directly to the anchor bolts.

In order to avoid a repetition of the previous situation, the following procedure should be followed:

1. The top anchor nuts should be loosened, and the base plate should be raised by 1/16". This can be achieved by a number of means that could be left to a contractor to propose. Jacking using a proprietary system such as the Rowan Tri-Chock™ is one recommended approach.

2. The space between the pole's base plate and the concrete foundation should be re-grouted using a non-shrink pourable grout/high-strength concrete. Again, this can be left to a contractor to propose a system acceptable to the Engineer. Master Builders, for example, has products that may be suitable such as Masterflow 928 grout or Set-45 concrete. Both are pourable, and thus formation of air voids/honeycombing can be avoided.

3. Re-torque the anchor nuts, snug-tight only.

It should be noted that this phase will remove compressive stresses previously applied to the bolts. Moreover, most shear will be transferred through base friction/adhesion of the grout. Thus, by reducing the average stress range by 50 percent, according to Eq. 40 the remaining life of the existing system will be increased by a factor of eight (2^3).

5.3 PHASE II: PROVIDE BACKUP SYSTEM

With the implementation of Phase I remediation the remaining fatigue life of the pole anchorages is still finite and considered insufficient in the long term. This can be overcome by providing a backup system which will effectively become the primary anchorage. It is proposed that a composite post-tensioned base anchorage should be provided, as shown in Fig. 5.1. This can be achieved by carrying out the following steps, as illustrated in Fig. 5.2.

1. Using a 2" diameter diamond core drill, bore holes through the base plate and concrete base, as shown in Fig. 5.2. The exterior holes should be inclined to avoid drilling through existing reinforcing steel and anchor bolts.

2. Epoxy grout in the 1-3/8" diameter high alloy DYWIDAG thread-bars. An acceptable grout should be proposed and approved by the Engineer. One recommended proprietary type is Brutem AB supplied by Master Builders. The depth of anchorage should be established by analysis, based on the in-situ concrete strength of the existing bases and proof tested on a trial bolt installed adjacent to the pole base. Data in the literature would indicate that these bolts may need to be anchored on the order of 6 ft deep. It should be noted that the upper 12" should remain unbonded by sleeving.

3. Post-tension the anchor bolts to 70 percent of their specified ultimate tensile strength, using an understress/overstress relaxation technique. This should require temporary jacking forces up to 180 kips per bolt.

This second phase will remove any loading from the existing bolts, except for winds in excess of approximately 40 mph, which rarely occur in any case. Furthermore, by post-tensioning, the stress cycling range on the new bolts is minimized. In fact, the maximum stress range under extreme winds will only be in the order of 10 ksi. This is well below the fatigue limit for this class of bolt material. Thus, fatigue should no longer be a problem.

5.4 PHASE III: PROVIDE ADDITIONAL DAMPING

It has been shown that once the first two phases of retrofit have been implemented, stress cycling on the original bolts should be eliminated and on the new system minimized through post-tensioning. It is considered, however, that fatigue problems may arise elsewhere, in neighboring connections. For example, the fillet welds that connect the pole shell to the base plates are also a fatigue prone detail that possess a finite life.

In order to avoid future problems, the wind induced cyclic stress range can be reduced further by increasing the damping in the pole. Fig. 5.3 shows the placement of proposed viscous dampers. Analyses have been carried out to investigate the feasibility of such a further retrofit measure. Fig. 5.4 shows the analytically predicted dynamic response of the pole for an extreme wind with and without added damping. The corresponding time histories of the stresses in Bolts 1 to 3 are illustrated in Fig. 5.5. In this analysis it was assumed that 16 percent viscous damping was added to the existing 4 percent equivalent damping. It is evident that the pole response is reduced by approximately 50 percent. Such a reduction will provide an 8-fold increase to the remaining fatigue life.

A viable damping system for the light pole could consist of two viscous dampers installed to the concrete parapet of the stadium each at an inclination of 45 deg with the pole principal axes. Of particular concern in implementing such a system, however, is the magnitude of the loads being imparted to the parapet. For the proposed configuration of the damping system, the maximum design damper force is projected to be 3 kips for the 50 year design wind, Fig 5.6 (a). This ultimate load on the stadium parapet should be checked as to its acceptability. It should be emphasized, however, that under more typical 50 percentile damaging wind $V_{50\%}$, the maximum parapet loads will be reduced to a modest 400 lbs. Also of interest from the design point of view are the displacements and velocities of the pole at the stadium height, as shown in Fig. 5.6.

Based on these analyses, contractors could be invited to quote a design-build damping system with the following specification:

C = 0.215 Kips/inch/sec

Stroke = ± 16.0 inches

Maximum Velocity = 13 inch/sec

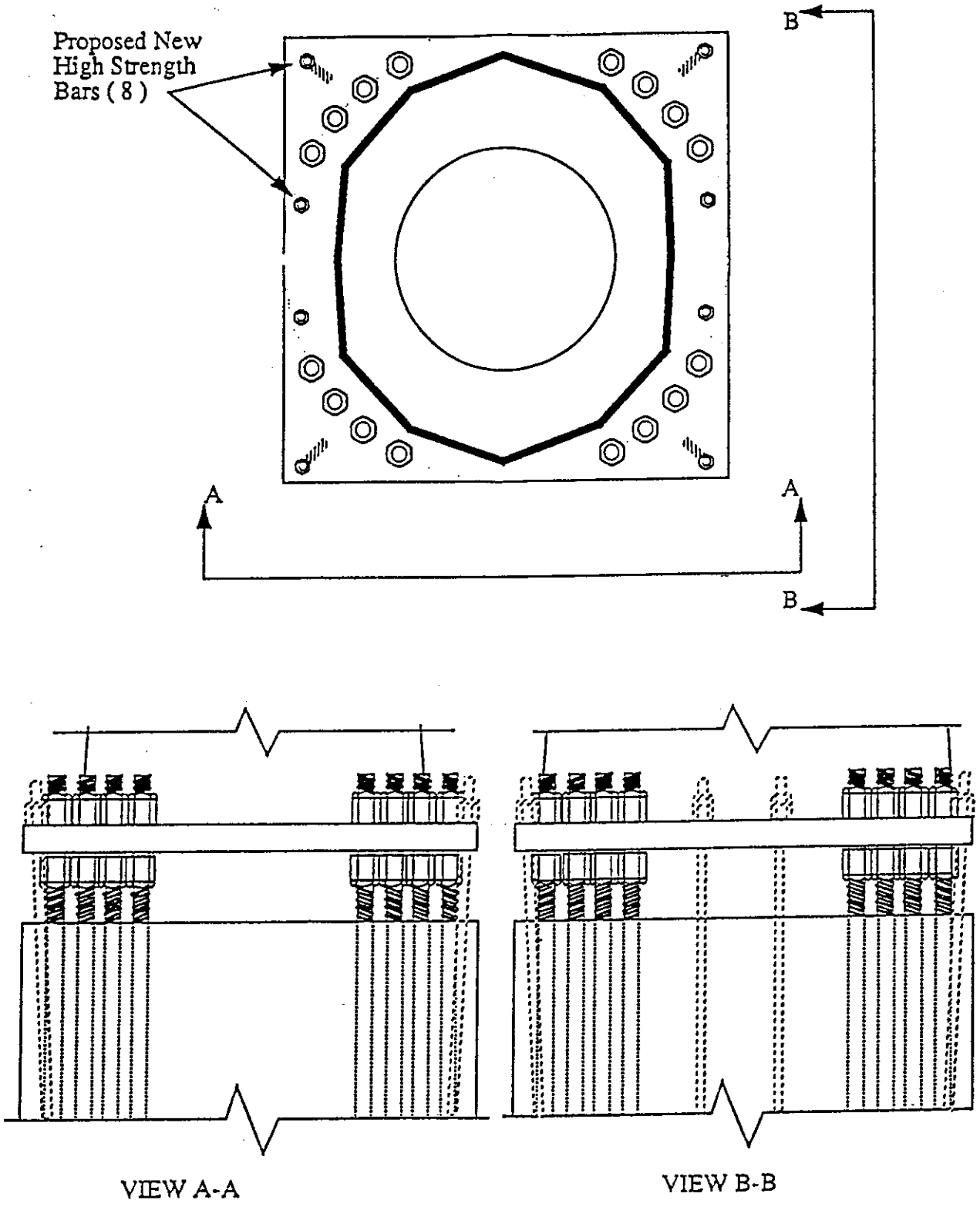

Fig. 5.1 : Proposed Additional Anchorage

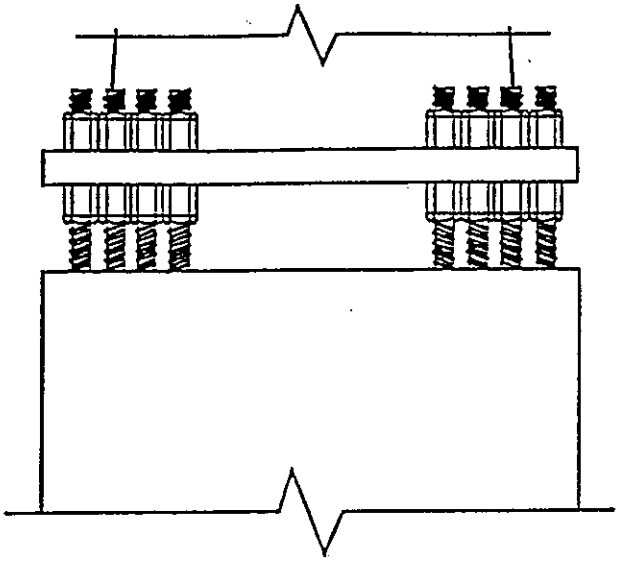

1. Current Position

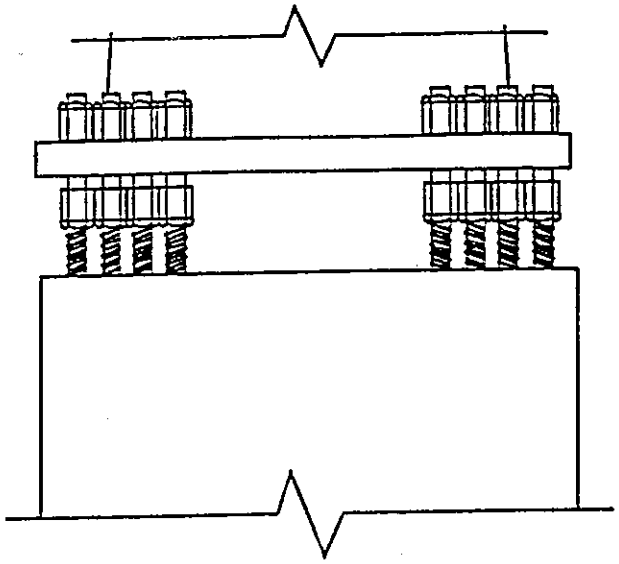

2. Loosen Anchor Nuts and Raise Base Plate off Levelling Nuts

3. Fill Void Beneath Base Plate with Non-Shrink Grout

4. Bore Holes for High Strength Anchor Bars

5. Epoxy Grout for New Anchorages

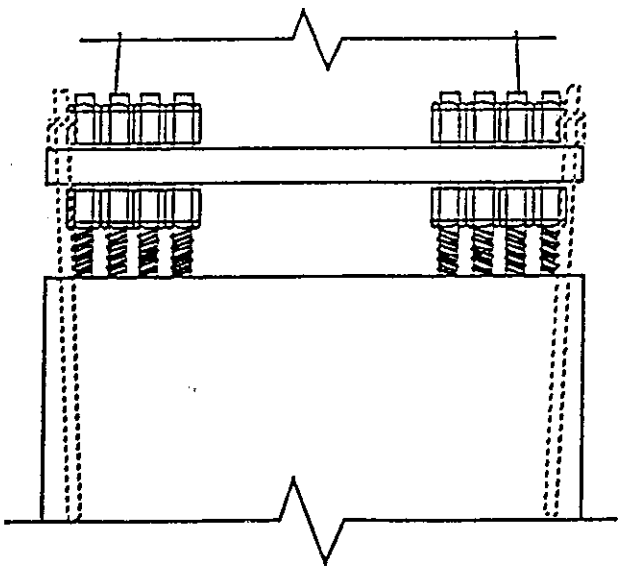

6. Post Tension High Strength Bars

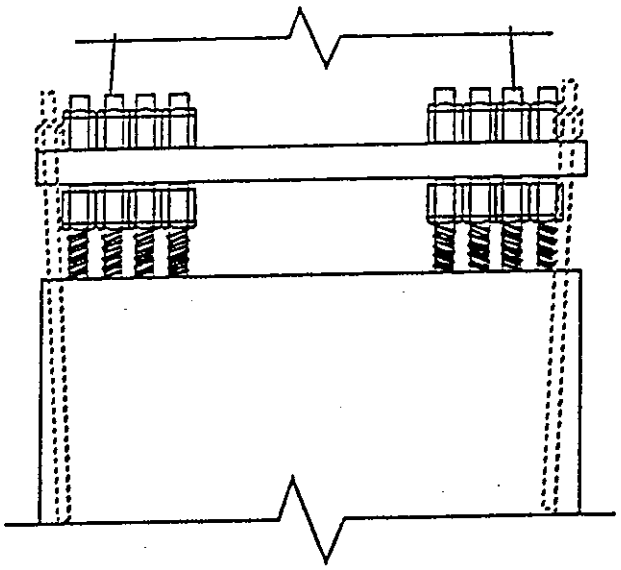

7. Proposed Final Position

Fig. 5.2 : Proposed Additional Anchorage Procedure

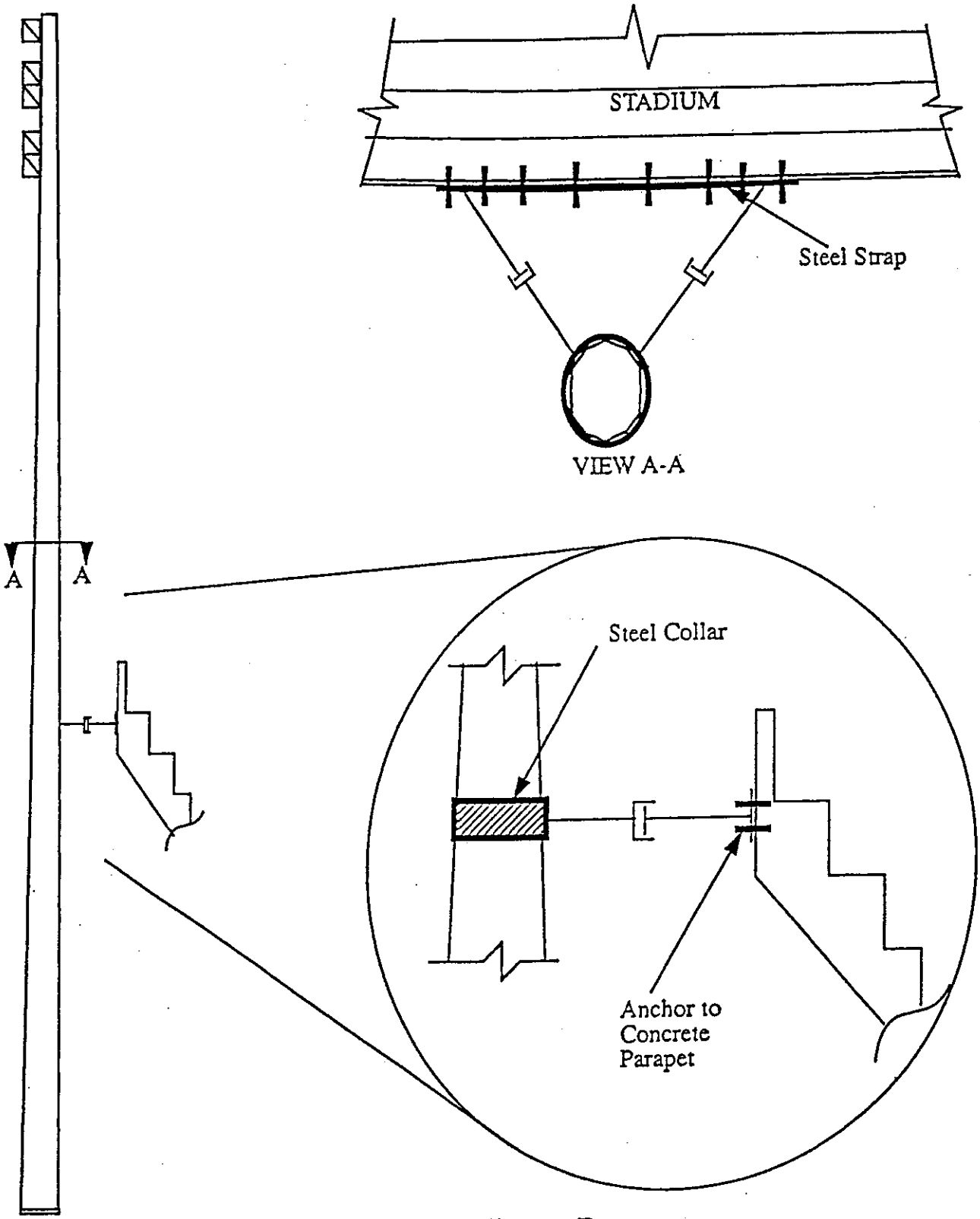

Fig. 5.3 : Placement of Proposed Viscous Dampers

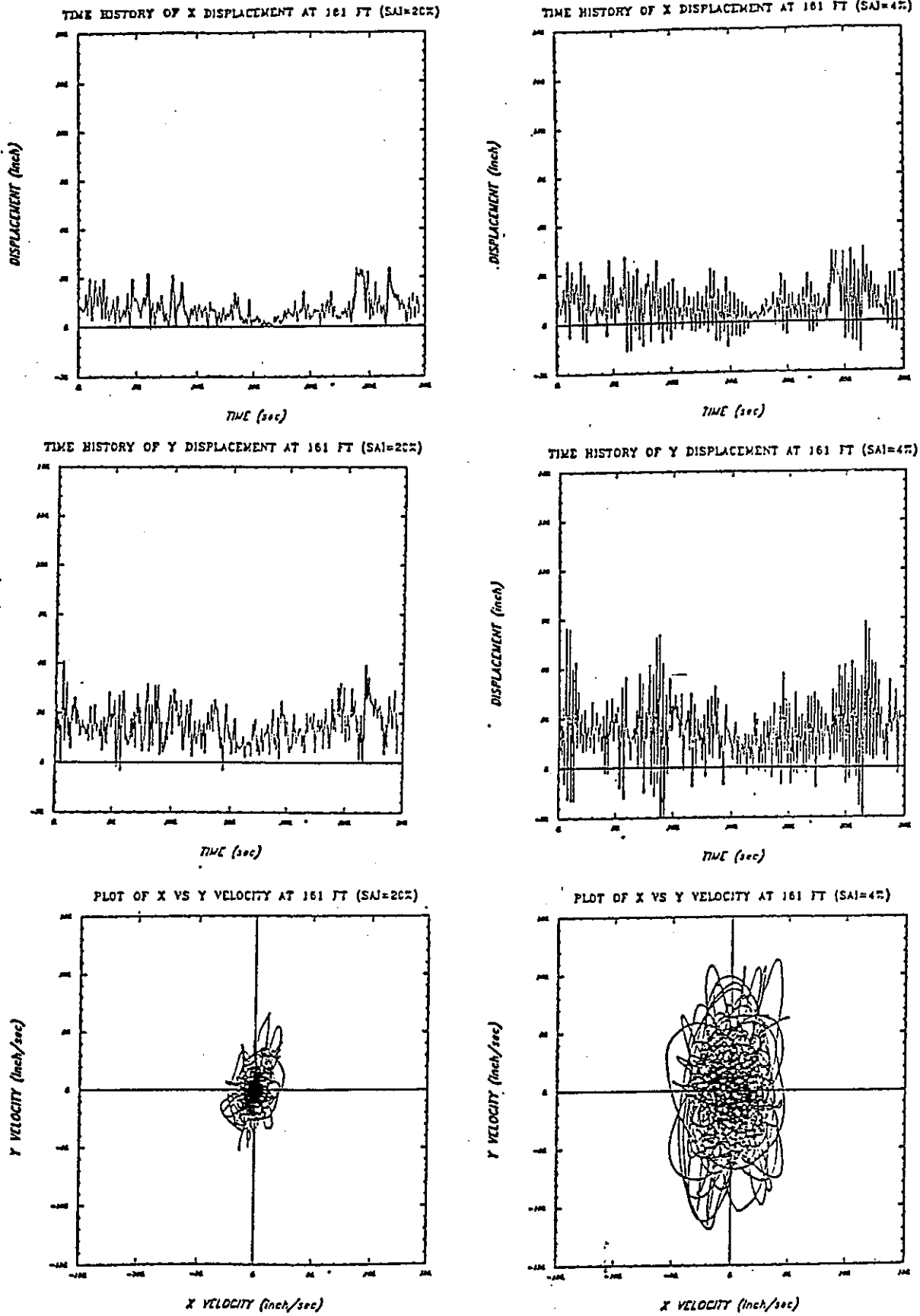

Fig. 5.4 : Comparison of Pole Response To 50 Year Wind With and Without Added Damping

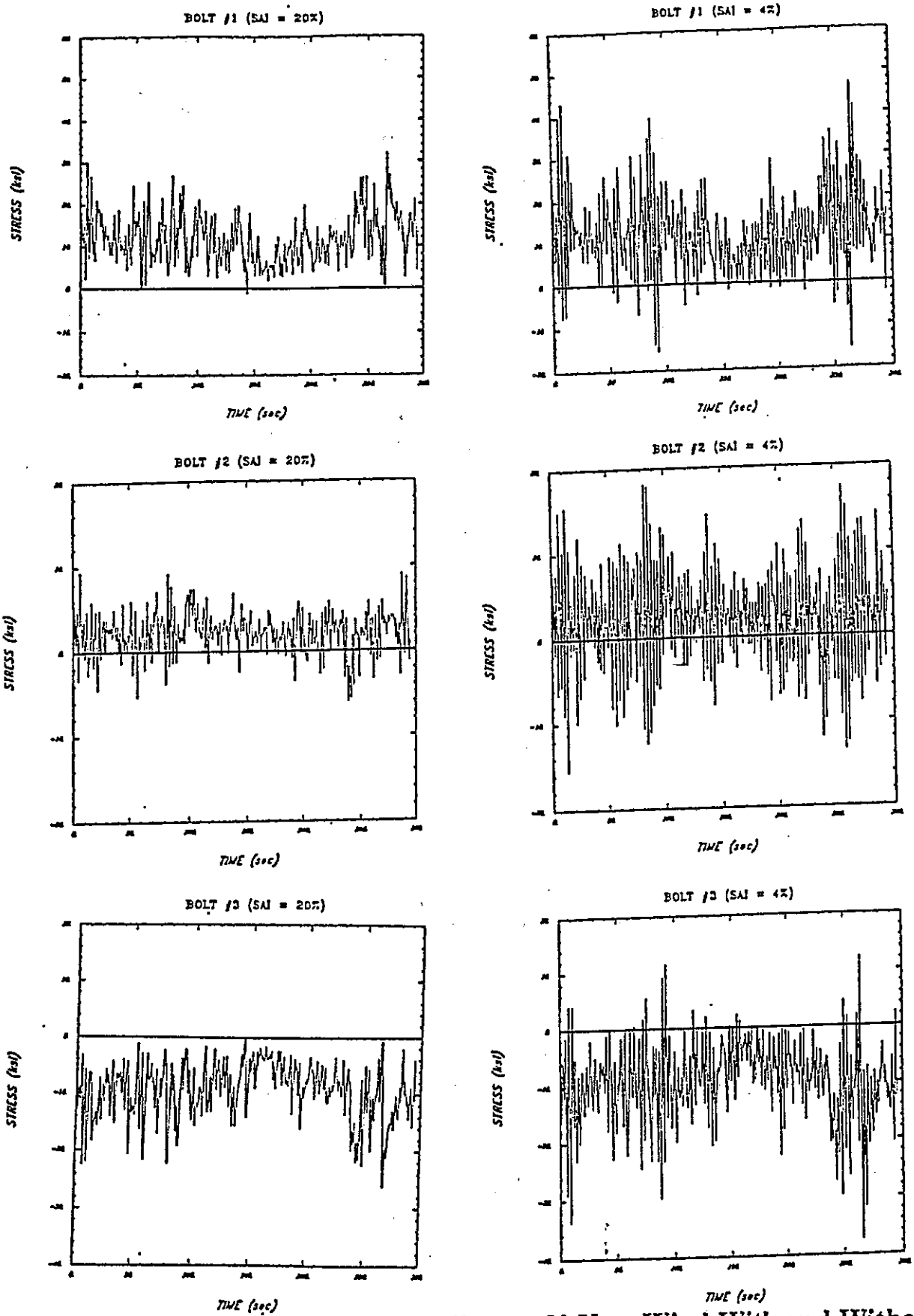

Fig. 5.5 : Comparison of Bolt Stresses Due to 50 Year Wind With and Without Added Damping

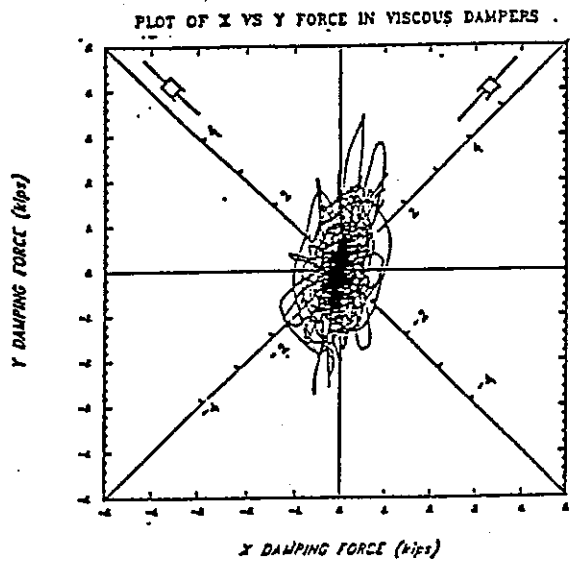

(a)

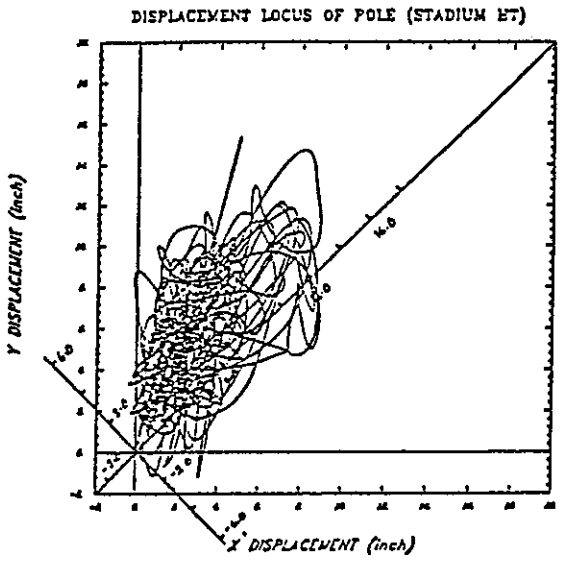

(b)

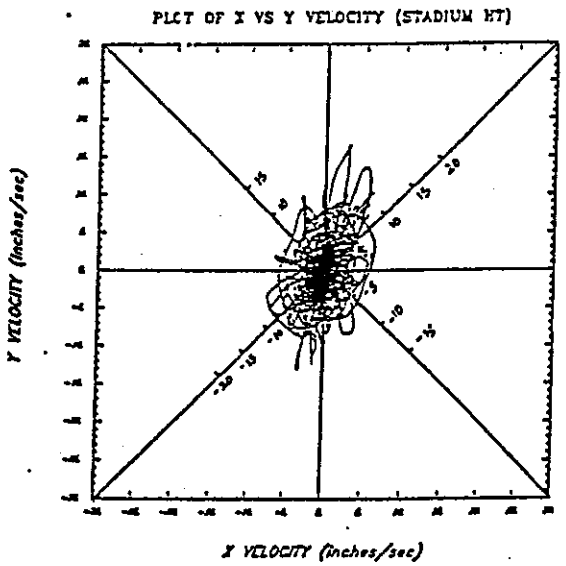

(c)

Fig. 5.6 : Time Variation of Damper Design Parameters for the 50 year wind.

SECTION 6

CONCLUSIONS AND RECOMMENDATIONS

From the results of the experimental and analytical study presented in this report, the following conclusions are listed.

1. The interrelationship between the applied unsteady wind load, the dynamic response of a light pole and the fatigue induced damage is somewhat complicated. However, by careful synthesis of the along-wind and across-wind response modes it is possible to predict fatigue damage using either time or frequency domain solutions.

2. An experimental study of one of the light poles at Rich Stadium showed that the pre-cracking fatigue life of a number of the bolts has been consumed already. The investigation confirms that fatigue cracks are to be expected, that they do exist, and that they are growing.

3. The remaining post-cracking fatigue life till fracture (separation) is not easy to predict without being able to visually observe the shape and nature of the crack. An analysis of several different crack front types all show that the remaining life is likely to be less than one year for the more severely cracked bolt.

4. A three-phase retrofit scheme has been proposed that should eliminate the present fatigue problem in the anchor bolts. The first two stages of the retrofit are <u>essential</u>, the third desirable.

5. The third stage retrofit requires the installation of viscous dampers on the pole. This should substantially increase the remaining fatigue life of other fatigue-prone details. This measure is considered essential if the expected life of the stadium is to be at

least another 20 years.

The following recommendations are also made:

1. During the course of the retrofit, the existing instrumentation system should be kept intact, recalibrated as necessary, and used to monitor the reduction in stress ranges to the bolts monitored as part of the study reported herein.

2. During the anchorage retrofit, it is recommended that one severely cracked bolt be removed for further forensic analysis. With a visual inspection of the crack front alone it may be possible to clear up the uncertainty surrounding the post-cracking analysis and to provide a more reliable correlation of acoustic emission count rate with ΔK for this type of steel, specimen geometry, crack front configuration and present damage state. Under such controlled laboratory conditions, many of the assumptions and approximations that were necessary in conducting the fatigue and post-cracking analyses could be directly investigated. Fractographic studies should also be carried out, as should cycling to failure under a stress relating to $V_{50\%}$.

Appendix 1

Calculation of $\overline{G}$ based on ANSI A58.1 1982

The gust factor calculation is based on the equation

$$\overline{G} = 0.65 + \left(\frac{P}{\beta} + \frac{(3.32T_1)^2 S}{1 + 0.002c}\right)^{\frac{1}{2}}$$

where

$$P = \bar{f} J Y$$

and

$$\bar{f} = \frac{10.5fh}{sV}$$

where

c = Average horizontal dimension in direction normal to wind in ft

D_o = Surface drag coefficient (Table A6)

f = fundamental frequency in Hz

h = Height of structure in ft

J = Pressure profile factor as function of γ (Fig. A6)

P = Probability of exceeding design wind speed in n years (Eq. A4)

s = Surface friction factor (Table A9)

S = Structure size factor (Fig. A8)

T_1 = Exposure factor evaluated at height of the structure (Eq. A6)

V = Basic wind speed in mph

Y = Structural profile factor as function of γ and c/h (Fig. A8)

z_g = Height of wind profile (Table A6)

α = exponent constant for wind profile (Table A6)

β = Structural damping coefficient

γ = exposure category constant depend on height of structure (Table A9)

The sample computations of $\overline{G}$ for Rich Stadium Light poles are as follows:

Exposure Category = C (Assumed)

Structural Properties:

h = 160 ft; c_x = 29.4375 in; c_y = 39.2188 in;

Damping factor β = 0.02 assumed prior to any field measurement.

γ = 0.23/h = 0.23/160 = 0.0014375; s = 1.0. (Table A9)

From Table A6 the constants are: α = 7.0; z_g = 900; D_o = 0.005.

From Fig. A8: S = 0.96; Y = 0.614

From Fig. A6: J = 0.0036

Fundamental frequencies: f_x = 0.30 Hz and f_y = 0.37 Hz

Calculation of T_1

$$T_1 = \frac{2.35(D_o)^{\frac{1}{2}}}{\left(\frac{z}{30}\right)^{\frac{1}{\alpha}}} = \frac{2.35(0.005)^{0.5}}{\left(\frac{160}{30}\right)^{\frac{1}{7}}} = 0.1308$$

Calculation of $\overline{G}$ for basic wind speed V = 70 mph

For weak axis

$$\bar{f} = \frac{10.5 f_x h}{sV} = \frac{10.5*0.29*160}{1.0*70} = 6.96$$

$$P = \bar{f} J Y = 6.96*0.0036*0.614 = 0.0154$$

$$\therefore \overline{G} = 0.65 + \left(\frac{0.015}{0.02} + \frac{(3.32*0.1308)^2*0.96}{1 + 0.002*2.453125} \right)^{\frac{1}{2}} = 1.614$$

For strong axis

$$\bar{f} = \frac{10.5 f_x h}{sV} = \frac{10.5*0.37*160}{1.0*70} = 8.88$$

$$P = \bar{f} J Y = 8.88*0.0036*0.614 = 0.0196$$

$$\therefore \overline{G} = 0.65 + \left(\frac{0.0196}{0.02} + \frac{(3.32*0.1308)^2*0.96}{1 + 0.002*3.26823} \right)^{\frac{1}{2}} = 1.727$$

Calculation of $\overline{G}$ for basic wind speed V = 35 mph

For weak axis

$$\bar{f} = \frac{10.5 f_1 h}{sV} = \frac{10.5*0.29*160}{1.0*35} = 13.92$$

$$P = \bar{f} J Y = 13.92*0.0036*0.614 = 0.0308$$

$$\therefore \overline{G} = 0.65 + \left(\frac{0.0308}{0.02} + \frac{(3.32*0.1308)^2*0.96}{1 + 0.002*2.453125} \right)^{\frac{1}{2}} = 1.964$$

For strong axis

$$\bar{f} = \frac{10.5 f_1 h}{sV} = \frac{10.5*0.37*160}{1.0*35} = 17.76$$

$$P = \bar{f} J Y = 17.76*0.0036*0.614 = 0.0393$$

$$\therefore \overline{G} = 0.65 + \left(\frac{0.0393}{0.02} + \frac{(3.32*0.1308)^2*0.96}{1 + 0.002*3.268233} \right)^{\frac{1}{2}} = 2.115$$

Keating, P., and Fisher, J. W.,
"Evaluation of Fatigue Tests and Design Criteria on Welded Details",
National Cooperative Highway Research Program Report 286, Transportation Research Board, National Research Council, 1986.

Kliman, V.,
"Fatigue Life Estimation Under Random Loading Using the Energy Criterion", Int. J. Fatigue, Vol. 7, No. 1, 1985, pp. 39-44.

Mackay, T. L., and Alperin, B. J.,
"Stress Intensity Factors for Fatigue Cracking in High-Strength Bolts", Engineering Fracture Mechanics, Vol. 21, No. 2, 1985, pp. 391-397.

Manson, S. S.,
"Behavior of Materials under Conditions of Thermal Stress", Heat Transfer Symposium, University of Michigan Engineering Reserach Institute, 1953, pp. 9-75.

Mattheck, C., Morawietz, P., and Munz, D.,
"Stress Intensity Factors of Sickle-shaped Cracks in Cylinderical Bars", Int. J. Fatigue, Vol. 7, No. 1, 1985, pp. 45-47

Moses, F., Schilling C. G., and Raju, K. S.,
"Fatigue Evaluation Procedures for Steel Bridges",
National Cooperative Highway Research Program (NCHRP) Report 299,
Transportation Research Board, National Research Council,
Nov 1987.

Scruton, C., and Rogers, E. W. E.,
"Steady and Unsteady Wind Loading of Buildings and Structures", Phil. Trans. Roy. Soc. London, A269 (1971), pp. 353-383.

Simiu, E., and Scanlan, R.,
Wind Effects on Structures, John Wiley and Sons, 1986.

Standards Association of New Zealand,
"Code of Practice for General Structural Design and Design Loadings for Buildings", New Zealand Standard NZS 4203:1976.

Toribio, J., Sanchez-Galvez, V., Astiz, M. A., and Campos, J. M.,
"Stress Intensity Factor Solutions for a Cracked Bolt under Tension, Bending and Residual Stress Loading", Engineering Fracture Mechanics, Vol. 39, No. 2, 1991, pp. 359-371.